SIMULATION OF FLUID INTERFACES

M. J. P. Nijmeijer

24 AUG. 1990

Universiteit Leiden
1 481 253 6

BIBLIOTHEEK
INSTITUUT-LORENTZ
voor theoretische natuurkunde
Postbus 9506 - 2300 RA Leiden
Nederland

Kast dissertaties

SIMULATION OF FLUID INTERFACES

PROEFSCHRIFT

TER VERKRIJGING VAN DE GRAAD VAN DOCTOR AAN DE RIJKSUNIVERSITEIT TE LEIDEN, OP GEZAG VAN DE RECTOR MAGNIFICUS DR. J.J.M. BEENAKKER, HOOGLERAAR IN DE FACULTEIT DER WISKUNDE EN NATUURWETENSCHAPPEN, VOLGENS HET BESLUIT VAN HET COLLEGE VAN DEKANEN TE VERDEDIGEN OP DONDERDAG 6 SEPTEMBER 1990 TE KLOKKE 14.15 UUR

DOOR

MARCO JAN PIETER NIJMEIJER

GEBOREN TE BEVERWIJK IN 1964

Promotie-commissie:

Promotor: Prof. Dr. J.M.J. van Leeuwen
Co-promotor: Dr. C. Bruin
Overige leden: Prof. Dr. D. Bedeaux
Prof. Dr. R. de Bruyn Ouboter
Prof. Dr. D. Frenkel
Prof. Dr. C.J.N. van den Meijdenberg
Prof. Dr. J.F. van der Veen

Het in dit proefschrift beschreven onderzoek werd uitgevoerd als onderdeel van het programma van de Werkgemeenschap voor Statistische Fysica van de Stichting voor Fundamenteel Onderzoek der Materie (F.O.M.) en is mogelijk gemaakt door financiele steun van de Nederlandse Organisatie voor Wetenschappelijk Onderzoek (N.W.O.).

CONTENTS

I General Introduction

1. Introduction 2

2. Wetting and drying 3

3. Outline 6

II Microscopic expressions for the surface and line tension

1. Introduction 9

2. The pressure tensor and the change in grand potential 11

3. The definition of the surface and line tension 14

4. Density expressions 16

4.1 Hard wall 16

4.2 Soft wall 18

5. Pressure expressions for the surface and line tension: hard wall 20

6. Pressure expressions for the surface and line tension: soft wall 24

7. Surface tension of a structured wall 30

8. Summary and conclusions 33

Appendix A 36

Appendix B 37

Appendix C 39

Appendix D 40

III A visual measurement of contact angles

1. Introduction 47

2. Description of the system 48
3. Calculation of the contact angles 49
4. Conclusion 56

IV Wetting and drying of an inert wall by a fluid

1. Introduction 60
2. Description of the simulations 61
3. Results 66
4. Conclusions 72

V Accurate determination of the location and order of the drying transition

VI Wetting and drying of a wall with a long-ranged wall-fluid interaction

1. Introduction 83
2. Description of the system 84
3. The density profiles 86
4. Effects of the finite system size 90
5. The wetting and drying transition 93
6. Conclusions 95

VII A search for prewetting

1. Introduction 99
2. Description of the system 101
3. Results 105
4. Conclusions 109

VIII The Lennard-Jones liquid-vapor interface

1. Introduction 113
2. Description of the system 114
3. Calculation of the surface tension 116

4. Comparison with other results and conclusion 118

IX Measurement of the surface tension of a drop

1. Introduction 122

2. Thermodynamics 124

3. Description of the simulations 128

4. Results 131

5. Conclusions 136

Samenvatting (summary in Dutch) 139

Curriculum vitae 142

List of publications 143

CHAPTER I

GENERAL INTRODUCTION

1. Introduction.

Interfaces appear in a wide variety of physical contexts. An interface forms the separation between two bulk phases and as these can be of all kinds, interfaces may have very different properties. From a macroscopic point of view, interfaces are sharp and can be regarded as a "sheet" separating the bulk phases. In this sheet acts a "stress", the surface tension, which tries to contract the sheet and therefore minimizes the area of the interface. The surface tension stabilizes the interface and the interface disappears when the surface tension vanishes. Two different types of interfaces are the solid-fluid and the fluid-fluid interface, which are the interfaces studied in this thesis. The solid-fluid interface can be considered as an interface imposed on the fluid by the rigid nature of the solid. This rigidity makes the interface "stiff", which stiffness is reflected in a large surface tension. The question why a fluid separates into two phases is much more subtle. Both phases, having no a priori structure, are alike and not as difficult to match as a solid and a fluid. Therefore, the surface tension of a fluid-fluid interface is in general lower than that of a solid-fluid interface and as a result, the former interface is much more flexible.

These differences are especially well visible at a microscopic level where the interface attains a structure and a finite width. The structure of the solid is described by a density profile with sharp peaks at the lattice positions. This peaked, oscillatory structure of the microscopic density propagates into the fluid at a solid-fluid interface as if the first adsorbed fluid layers are of a solid nature. The peaks damp out further into the fluid until the density profile attains a constant fluid density. Entirely different is the density profile of a fluid-fluid interface: it interpolates smoothly between the densities of the fluid phases. The low value of the surface tension of a fluid-fluid interface causes the interfacial width to be significantly increased by capillary wave fluctuations. In fact, fluid-fluid interfaces are unstable with respect to these fluctuations and their width diverges in an infinite, field-free system1). The systems encountered in e.g. simulations, however, are finite although the simulated interfaces may still be very wide, especially near criticality where the surface tension vanishes.

Quantities like the surface tension are closely connected to the structure of the interface. As an example, the surface tension γ of a fluid-fluid interface can be expressed2) in the paircorrelation function $n_2(\vec{r}_1,\vec{r}_2)$ in the interface and the interaction potential $\phi(r)$ between the particles:

$$\gamma = \frac{1}{2} \int_{-\infty}^{\infty} dz_1\, dz_2 \int_{-\infty}^{\infty} dx_{12}\, dy_{12} \frac{x_{12}^2 + y_{12}^2 - 2z_{12}^2}{2r_{12}} \frac{\partial\phi(r_{12})}{\partial r_{12}}\, n_2(z_1,z_2,r_{12}) \quad (1.1)$$

where $\vec{r}_{12}=\vec{r}_1-\vec{r}_2$ and we employed the planar symmetry by which n_2 depends only on the z-positions of the particles and their distance r_{12} (the z-direction is taken to be perpendicular to the interface). Note that the integral vanishes in the bulk fluid phases at $z=\infty$ and $z=-\infty$ where n_2 becomes isotropic. In a simulation of a fluid interface by molecular-dynamics or Monte Carlo techniques, one can sample the paircorrelation function and evaluate the integral. One can thus measure a surface tension directly with an accuracy that is determined by the statistical accuracy of the results of the sampling.

Expressions like (1.1) are regularly employed in the simulations described in this thesis. This is possible since one can obtain from a simulation the microscopic structure of an interface with details that can not be given by theoretical considerations or experimental techniques. Moreover, simulations study a well-defined model system which facilitates the comparison with theoretical predictions. In this thesis for example, results of our simulations are compared with the results of density functional calculations$^{3)}$ which are tailored for the simulations. The limitations of a computer experiment are related to the limitations on the computer capacities. A direct consequence of these limitations is an upper bound on the size of the systems that can be simulated. This bound becomes especially crucial in simulations of interfacial phenomena because one needs at least two bulk phases to form an interface. In the wetting simulations of the capters III-VI, we even encounter three bulk phases and a substrate simultaneously in the system. This is beyond the capacity of a usual simulation which treats maximally a thousand particles. A second, important limitation of the simulations is the limitation on the range of the interactions which is necessary to keep the computing time within reasonable limits. Realistic interactions, which are long-ranged, are often modelled by truncated Lennard-Jones potentials but it is shown in chapter IIX that the truncation is by no means harmless and may have a large effect on the properties of an interface.

Our simulations are carried out on a special purpose computer: the Delft Molecular-Dynamics Processor (DMDP)$^{4)}$ which allows systems up to 16,000 particles. The use of this computer and its 24 hours per day availability, enabled the large-scale simulations described in this thesis. As already stated by the name of the DMDP, the simulations are of the molecular-dynamics type. All phases in the system are formed by particles with a Lennard-Jones 12-6 interaction:

$$\phi(r) = 4\varepsilon \{(\sigma/r)^{12} - (\sigma/r)^{6}\} \tag{1.2}$$

which is truncated at 2.5σ. The majority of the simulations is devoted to the "wetting" and "drying" transition and related phenomena. These transitions will be described in the next section.

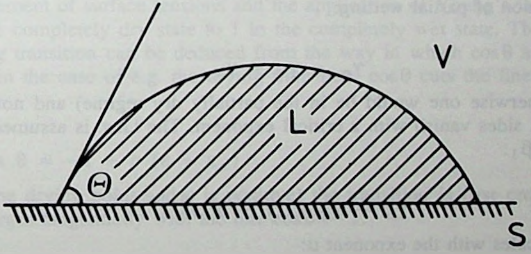

Fig. 1. A liquid droplet at a substrate, surrounded by a saturated vapor; θ is the contact angle.

2. Wetting and drying.

The terms wetting and drying refer to the adsorption of two coexisting phases at a third "spectator" phase[5]. A model system to discuss these phenomena is the system of a coexisting liquid and vapor phase in contact with a wall, which is also the system encountered in our simulations. Consider a liquid drop that rests on the substrate and is surrounded by a saturated vapor. The liquid-vapor interface makes a well defined angle with the substrate-liquid interface which is called the contact angle θ (see fig. 1). This angle is related to the surface tensions γ_{sl}, γ_{sv} and γ_{lv} that belong to the substrate-liquid, the substrate-vapor and the liquid-vapor interface respectively. This relation, called Young's law, takes the form of a condition for mechanical equilibrium if the surface tensions are considered as mechanical forces that act on the contact line where the three phases meet. It reads

$$\gamma_{sv} = \gamma_{sl} + \gamma_{lv} \cos\theta \tag{2.1}$$

The contact angle varies with e.g. temperature. If it vanishes, the droplet spreads over the substrate and a liquid layer intrudes between the solid and the vapor phase all over the substrate surface. The vanishing of θ thus implies that a direct contact between the substrate and the vapor phase is no longer stable but that a macroscopically thick liquid layer should develop in between them. Complementary, a contact angle that is equal to π implies that a stable interface between substrate and liquid incorporates an intermediate macroscopic vapor layer. The case $0 < \theta < \pi/2$ is called the partially wet state, the case $\theta = 0$ the completely wet state and similarly are the cases $\pi/2 < \theta < \pi$ called the partially dry and $\theta = \pi$ the completely dry state. The transition from the partially wet to the completely wet state is a genuine surface phase transition, called the wetting transition. The drying transition is defined analogously. The transition from the partially dry to the partially wet state is not a phase transition but it is convenient to be able to distinguish between these two states.

The wetting and drying transition have attracted much interest by an argument of Cahn[6] that predicts that, whenever a system is partially wet (dry) at T below T_c, one should encounter a wetting (drying) transition as the temperature is raised towards T_c. Cahn inspected the condition of partial wetting:

$$\gamma_{sv} - \gamma_{sl} < \gamma_{lv} \tag{2.2}$$

(with $\gamma_{sl} < \gamma_{sv}$, otherwise one would be in the partially dry regime) and noticed that as T approaches T_c both sides vanish with a critical exponent. The l.h.s. is assumed to scale with a surface exponent β_1:

$$\gamma_{sv} - \gamma_{sl} \propto (T - T_c)^{\beta_1} \tag{2.3}$$

whereas the r.h.s. scales with the exponent μ:

$$\gamma_{lv} \propto (T - T_c)^{\mu} \tag{2.4}$$

which have the values $\beta_1 = 0.8$ and $\mu = 1.3$ in the $3-d$ Ising universality class, which is the appropriate universality class for classical, three dimensional fluids. As γ_{lv} vanishes faster that the difference $(\gamma_{sv} - \gamma_{sl})$ according to these scaling assumptions, inequality (2.2) should break down at a temperature T_w, the wetting temperature, below T_c where the inequality becomes an equality:

$$\gamma_{sv} - \gamma_{sl} = \gamma_{lv} \tag{2.5}$$

which marks the presence of a wetting transition. This wetting scenario is called "critical point wetting" because the wetting transition is expected in the vicinity of the critical point.

Obviously, Cahn's argument cannot be rigorously correct because, as soon as the wetting transition occurs, (2.5) holds and thus, scaling assumption (2.3) is no longer valid. Instead, the difference $(\gamma_{sv}-\gamma_{sl})$ should also scale with μ. A careful analysis7) of scaling functions is needed to understand the flaw in the argument. Nevertheless, the notion of Cahn has inspired much research on the wetting transition and many systems have indeed been shown to exhibit critical point wetting. The status of the drying transition is less clear. Although the wetting and drying transition appear to be two similar demonstrations of the same physical mechanism, a drying transition has not been observed experimentally. Questions put forward in the research5) on wetting and drying are e.g. on the location and order of the transitions and their relation to the molecular interactions. Theoretically, such questions have been studied in lattice models8,9), in variants of Landau's mean-field theory5) and by density functional calculations3,10,11). There is general agreement that in systems with realistic interactions, the wetting transition is first order unless the transition takes place very close to T_c in which case continuous wetting may occur11).

Intermediate between theory and experiment, simulations of the wetting and drying transition have been carried out, both in lattice models and in models of real fluids. Among the earliest examples of the latter is a simulation of van Swol and Henderson12) who studied the drying transition in a system with square-well interactions. A more extensive simulation of wetting and drying in a Lennard-Jones system was carried out on the DMDP by Sikkenk *et al*13). Instead of by temperature, the transitions are driven in both simulations by changing the substrate-fluid interaction strength ε. Increasing ε, one passes from the completely dry to the completely wet state via a drying and, subsequently, a wetting transition. These transitions are identified by a measurement of $\cos\theta$ as a function of ε where $\cos\theta$ is obtained from a measurement of surface tensions and the application of Young's law. The cosine rises from -1 in the completely dry state to 1 in the completely wet state. The order of the wetting and drying transition can be deduced from the way in which $\cos\theta$ approaches its limiting values. If in the case of e.g. the drying transition, $\cos\theta$ cuts the line $\cos\theta = -1$ under a finite angle:

$$\cos\theta = -1 + c\,(\varepsilon - \varepsilon_d) \tag{2.6}$$

(where ε_d is the drying point and c is positive) the transition is first order. If, on the other hand, $\cos\theta$ merges tangentially with the line $\cos\theta = -1$:

$$\cos\theta = -1 + c\,(\varepsilon - \varepsilon_d)^x \qquad x > 1 \tag{2.7}$$

the transition is continuous. Inspecting the contact angles, both simulations predicted a first-order drying transition whereas the simulation of Sikkenk *et al* also gave a first-order wetting transition. However, the results of Sikkenk *et al* for the drying transition turned out to be controversial14) because of inaccurate measurements of γ_{sv} and γ_{sl}.

Outline

The simulations described in the chapters III-VII are related to the wetting and drying transition and contain a liquid phase, a vapor phase and a substrate. The latter is absent in he simulations of the chapters VIII and IX which aim at a study of the liquid-vapor interface. Before we describe the simulations, we devote a chapter, chapter II, to a discussion of relations like (1.1) between macroscopic and microscopic quantities of the interface. As such relations are frequently used in the simulations, chapter II provides the formal background for those measurements. Special attention is paid to the derivation of an expression for the surface tension of an interface between a fluid and a substrate that is modelled by a structured, i.e. periodic, external potential. Such interfaces are encountered in the simulations and the appropriate expression for γ had not yet been derived. The derivation had been given for a structureless substrate but it turned out that as one treats the more realistic structured case, the derivation becomes much more complicated.

Chapter III treats a visual measurement of contact angles which circumvents the measurement of surface tensions that had been so cumbersome in the simulation of Sikkenk *et al.* A liquid-vapor meniscus is enclosed between two parallel substrates and the angle is obtained from the shape the meniscus attains. The angles display a strongly shifted drying transition compared with Sikkenk's simulation and moreover, they are consistent with both a first-order and a continuous character of this transition. The wetting transition has remained first-order.

This modified picture of the wetting and drying transitions is confirmed in chapter IV. The set-up of the simulations in this chapter is the same as in Sikkenk's simulation apart from the representation of the substrate. Whereas the substrate particles were allowed to oscillate around their lattice positions in the simulation of Sikkenk *et al*, they are frozen in at those positions here. Representing the wall thus as an external potential, one obtains a series of contact angles with varying ε which agrees well with the visually measured angles.

The most accurate determination of the order and location of the drying transition is obtained in chapter V. In this chapter, the variation of the contact angle with ε is measured. The measurements form strong evidence for a continuous transition and, moreover, locate the position of the transition an order of magnitude more accurately with respect to the measurements of the angle itself.

In chapter VI, a step towards the simulation of a more realistic system is taken. We have added the long-ranged tail of the substrate-fluid interaction to the simulations and reinspected the wetting and drying transitions. It is to be expected that the drying transition will be suppressed by the added tail and this is confirmed by the simulations.

Chapter VII inspects a transition which should accompany a first-order wetting transition: the prewetting transition[6,15]. This is a transition between a thin and a thick adsorbed film which occurs in the regime of the undersaturated vapor. The existence of this transition is predicted on sound theoretical grounds but it has so far only been observed in lattice-gas simulations[16,17] and in one simulation[18] of a Lennard-Jones system. Any experimental observation lacks in spite of several attempts[19,20]. We have inspected the adsorption at the wall at a range of vapor densities and values of ε but find no clear evidence for a thin-thick transition. The region in which the transition occurs must be narrow and we give bounds on it.

The last two chapters discuss some properties of liquid-vapor interfaces. Chapter VIII discusses simulations in which a part of the liquid-vapor coexistence line is scanned with planar interfaces between the coexisting phases. The values quoted in the literature for the liquid-vapor surface tension vary significantly. We have accurately measured this quantity, as well as some properties of the liquid and vapor phases. Moreover, we increased the cut-off radius of the Lennard-Jones potentials from 2.5σ to 7.33σ and observed a significant effect on the properties of the interface and the coexisting phases.

The last chapter studies the influence of curvature on the surface tension in a simulation of liquid drops. It is assumed$^{21)}$ that the surface tension deviates from its planar value with an amount of the order of the inverse droplet radius. We show that this amount can be obtained from an analysis of the pressure difference over the interace and this difference is evaluated in the simulations. It turns out that the effect of the curvature is small.

References

1) for a review see e.g. M.P. Gelfand and M.E. Fisher, Physica A **166,** 1 (1990).
2) D. Schofield and J.R. Henderson, Proc. R. Soc. Lond. A **379,** 231 (1982).
3) A. Velasco and P. Tarazona, J. Chem. Phys. **91,** 7916 (1989).
4) A.F. Bakker and C. Bruin, in *Special Purpose Computers,* edited by B.J. Alder (Academic, London, 1988).
5) for a review see e.g. S. Dietrich, in *Phase Transitions and Critical Phenomena,* edited by C. Domb and J. Lebowitz (Academic, London, 1988), Vol 12.
6) J.W. Cahn, J. Chem. Phys. **66,** 3667 (1977).
7) M.P. Nightingale and J.O. Indekeu, Phys. Rev. B **32,** 3364 (1985).
8) R. Pandit, M. Schick and M. Wortis, Phys. Rev. B **26,** 5112 (1982).
9) C. Ebner, Phys. Rev. B **28,** 2890 (1983).
10) C. Ebner and W.F. Saam, Phys. Rev. Lett. **38,** 1486 (1977).
11) F. van Swol and J.R. Henderson, Phys. Rev. A **40,** 2567 (1989).
12) F. van Swol and J.R. Henderson, Faraday Symp. Chem. Soc. **20,** 1 (1985).
13) J.H. Sikkenk, J.O. Indekeu, J.M.J. van Leeuwen, E.O. Vossnack and A.F. Bakker, J. Stat. Phys. **52,** 23 (1988).
14) F. van Swol, Phys. Rev. Lett. **60,** 239 (1988).
15) E.H. Hauge and M. Schick, Phys. Rev. B **27,** 4288 (1983).
16) D. Nicolaides and R. Evans, preprint.
17) A.K. Sen and C. Ebner, Phys. Rev. B **33,** 5076 (1986).
18) J. Finn and P.A. Monson, Phys. Rev. A **39,** 6402 (1989).
19) J.W. Schmidt and M.R. Moldover, J. Chem. Phys. **84,** 4563 (1986).
20) G. Ascarelli and H. Nakanishi, J. Phys. France **51,** 341 (1990).
21) for an introduction see e.g. J.S. Rowlinson and B. Widom, *Molecular Theory of Capillarity* (Clarendon, Oxford, 1982).

CHAPTER II

Microscopic expressions for the surface and line tension

ABSTRACT

We consider the change in grand potential of a fluid under a deformation of its containing vessel. Thermodynamically, the change is expressed in terms of the pressure, the surface tension and the line tension of the fluid. As the change can also be expressed in the fluid's microscopic properties, one obtains microscopic expressions for thermodynamic quantities. We consider two types of such expressions, the first one relating the pressure, surface and line tension to the density at the hard walls of the vessel, the second one relating them to the pressure tensor. Moreover, we can generalize these two types of expressions to a single expression which contains them both. Besides the distinction between surface and line tension, we consider three models of the wall: a "hard" wall, a "structureless, soft wall" and a "structured, soft wall". It is shown that the expressions for the surface and line tension are similar for all types of walls.

1. Introduction.

The behaviour of fluids near a wall has attracted considerable interest in recent years. Especially the question whether a fluid wets a wall or not, has been the subject of many investigations$^{1)}$. This question refers to the equilibrium state of the wall-fluid interface which is characterized by the surface tension, describing the contribution of the wall-fluid interface to the grand potential of whole system. It forms the basis of many theoretical descriptions of the interface and can be measured experimentally. There exist formal expressions relating it to microscopic properties of the interface. As these properties are accessible in a simulation, the surface tension can also be evaluated in a simulation$^{2)}$.

In reality, two thermodynamic phases meet at a wall-fluid interface: the fluid and the solid which forms the wall. The atoms of the solid form a lattice, oscillating around their lattice positions. In this perspective, a solid-fluid interface is similar to a liquid-vapor interface and the same molecular expressions apply. The description of the interface is greatly simplified if the solid atoms are frozen in at their lattice positions. This simplification alters the physics of the interface only marginally in many cases. Such a rigid lattice is no longer a part of the thermodynamic system but serves as a boundary condition for the fluid. The boundary condition appears as an external potential acting on the fluid particles and preventing them from escaping from the system. Microscopic expressions have to be adapted for such an inert wall.

This paper is addressed to the derivation of formal expressions for the surface tension and related quantities of an interface between a fluid and an inert wall. As model for the wall we will consider three cases

a) The simplest model is a wall which is only a restriction on the positions of the fluid particles. The restriction is represented by an external potential which is zero at one side of the wall and infinite at the other side. This representation of a wall will be denoted as a "hard wall".

b) The model of a wall becomes more realistic when the potential varies smoothly with the distance from the wall. If the potential is still translationally invariant along the wall, the model for the wall is denoted as a (structureless) "soft wall".

c) The closest inert representation of a real wall is an external potential field which depends not only on the distance from the wall but varies also along the wall. The latter variation models the lattice structure of the wall. Since a lattice is periodic, the external potential is taken to be periodic along the wall also. This model of the wall is denoted as a "structured, soft wall".

An example of a relation between a thermodynamic quantity and a microscopic quantity of a fluid is the connection between the density at a hard wall and the fluid's pressure. Approaching a hard wall from inside the fluid, the density of the fluid changes discontinuously from a finite value to zero in the wall. The finite, limiting value of the density is called the density at the hard wall, n_0. It is related to the pressure p of the fluid by$^{3)}$

$$p = k_B T \, n_0 \tag{1.1}$$

where k_B denotes Boltzmann's constant and T the temperature of the system. We call relations of this type between a thermodynamic quantity and the density of the fluid at a wall "density expressions".

In this example, the pressure is related to a surface property of the fluid. An example of a different kind is the classical relation[4)] between the pressure and the pair correlation function of the bulk fluid, n_{2B}

$$p = k_B T \, n_B - \frac{2\pi}{3} \int_0^\infty \mathrm{d}r \, r^3 \, \phi'(r) \, n_{2B}(r) \tag{1.2}$$

where n_B denotes the density of the bulk fluid, $\phi(r)$ the interparticle potential for two particles at a distance r and $\phi'(r)$ its derivative with respect to r. In this form, the relation holds for a three dimensional fluid with central, pairwise additive interactions which is the type of fluid we will restrict ourselves to throughout this article. Relations as (1.2), expressing a thermodynamic variable in essentially an integral over the pair correlation function, are called "virial expressions". Virial expressions can often be formulated in terms of a "pressure tensor". As an example, the virial expression for the surface tension of a hard wall, γ_h, located in the plane $z=0$ with the fluid at $z>0$, reads[5)]

$$\gamma_h = -k_B T \int_0^\infty \mathrm{d}z \, (n(z) - n_B)$$

$$+ \frac{1}{2} \int_0^\infty \mathrm{d}z_1 \int_{-\infty}^{\infty} \mathrm{d}\vec{r}_{12} \, \frac{\frac{1}{2}(x_{12}^2 + y_{12}^2)}{r_{12}} \, \phi'(r_{12}) \, (n_2(z_1, z_2, r_{12}) - n_{2B}(r_{12})) \tag{1.3}$$

with $\vec{r}_{12} = \vec{r}_1 - \vec{r}_2$, n_2 the pair correlation function. In terms of a pressure tensor, the relation reads[5)]

$$\gamma_h = -\int_0^\infty \mathrm{d}z \, (p^T(z) - p) \tag{1.4}$$

where $p^T(z)$ denotes the component of a pressure tensor tangentially to the hard wall at a distance z. The pressure tensor is defined in terms of the density and the pair correlation function (see below). Substitution of this definition transforms (1.4) back into (1.3). Relations between thermodynamic variables and a pressure tensor are especially useful in simulations of fluids where the tensor can be measured explicitly[6)]. We call such relations "pressure expressions".

Formal relations between thermodynamic and microscopic quantities such as (1.1)-(1.4) can be derived from a deformation of a vessel which contains the fluid and at the same time provides the wall-fluid interface. The deformation results in a change in the grand potential of the fluid which is thermodynamically expressed in terms of quantities like the pressure and surface tension. On the other hand, it is possible to express the change directly in microscopic quantities of the fluid. The equivalence of the two expressions leads to microscopic expressions for the thermodynamic quantities. This technique has been employed in various cases. A systematic evaluation of the deformation method has not been given and it is the purpose of this paper. We were confronted with this problem when we simulated fluids contained by structured, inert walls which require a delicate treatment of the microscopic expressions.

We will employ two microscopic expressions for the change in grand potential. The first expresses the change in grand potential in, essentially, the density at the hard walls. The expression gives rise to density expressions of the type (1.1). The second expresses the change in terms of a pressure tensor from which pressure expressions of the type (1.4) can be derived. In this paper, we will consider deformations of the vessel which result in an increase of the area of the vessel as well as an increase of the length of the edges. Therefore, the change in grand potential involves both the surface and the line tension and density and pressure expressions will be derived for both these quantities.

The deformation is applied to the three models of a wall we mentioned above. At first, a vessel of hard walls is considered. Secondly, one of the hard walls is replaced by a structureless, soft wall and finally, this wall is replaced by a structured, soft wall. We thus obtain density and pressure expressions for the surface tension of a hard wall, a structureless soft wall and a structured soft wall. We also obtain density and pressure expressions for the line tension of the edges in these vessels. We do, however, not consider the edge formed by a hard and a structured, soft wall since already the surface tension of the structured wall turns out to be a complicated case.

The article is further organized in the following way. We introduce the concept of the pressure tensor and the two routes to the change in grand potential in section 2. Before we start the actual calculation, we give some comments on the definition of the surface and line tension in section 3. The first route to the change in grand potential is then exploited in section 4 which derives the density expressions. The second route is exploited the sections 5, 6 and 7 in which the pressure expressions are presented. Section 5 treats the hard wall and the edge formed by two hard walls. Sections 6 treats the structureless soft wall and the edge formed by a hard and a structureless soft wall. Section 7 treats the case of the structured soft wall. Finally, conclusions are drawn in section 8.

2. The pressure tensor and the change in grand potential.

The concept of a pressure tensor has long been present in phenomenological descriptions of inhomogeneous fluids$^{4)}$. The concept has been formalized by Schofield and Henderson$^{7)}$ who gave a microscopic definition of the tensor which they could link rigorously to the change in grand potential of a fluid. For a simple fluid, the microscopic definition reads

$$\overset{\rightrightarrows}{p}(\vec{r}) = k_B T\, n(\vec{r})\, \overset{\rightrightarrows}{I} - \frac{1}{2} \int_{-\infty}^{\infty} d\vec{r}_1\, d\vec{r}_2\, \frac{\vec{r}_{12}}{r_{12}}\, \phi'(r_{12})\, n_2(\vec{r}_1,\vec{r}_2) \int_{C_{12}} d\vec{l}\, \delta(\vec{l}-\vec{r}) \tag{2.1}$$

where $\overset{\rightrightarrows}{I}$ denotes the unit tensor and C_{12} is a contour from $\vec{r}_2$ to $\vec{r}_1$. This contour can be chosen arbitrarily and therefore, the pressure tensor is not defined uniquely. The most obvious choice for the contour is a straight line from $\vec{r}_2$ to $\vec{r}_1$, a choice which is referred to as the Irving and Kirkwood$^{8)}$ (IK) tensor. An alternative choice has been investigated by Harasima$^{9)}$ who took the contour to be a straight path from $\vec{r}_1$ to (x_2, y_2, z_1) followed by a straight path to $\vec{r}_2$. Clearly, each expression of a physical quantity in terms of a pressure tensor, like (1.4), must be independent of the choice of the tensor. It can furthermore be shown that the divergence of all tensors (2.1) satisfies

$$\nabla \cdot \vec{\vec{p}}(\vec{r}) = -n(\vec{r}) \; \nabla \phi^{ext}(\vec{r}) \tag{2.2}$$

where $\phi^{ext}(\vec{r})$ denotes the external potential acting on the fluid.

The tensor (2.1) can be used to describe the change in grand potential of a fluid when the container of the fluid is deformed. Schofield and Henderson discussed these deformations in the canonical ensemble, preserving the amount of particles in the system. It is however easy to show that the expression for the change in free energy that they obtain applies equally well to the change in grand potential. This thermodynamic potential has to be considered if the deformation is brought about in the grand canonical ensemble under constant chemical potential. Instead of considering the canonical partition function Z_N of a system of N particles

$$Z_N = \frac{1}{\Lambda^{3N} N!} \int_V d\vec{r}_1, \ldots, d\vec{r}_N \; e^{-\beta U_N} \tag{2.3}$$

where Λ denotes the thermic wavelength, U_N the energy of a configuration of N particles

$$U_N(\vec{r}_1, \ldots, \vec{r}_N) = \sum_{(i,j)} \phi(r_{ij}) + \sum_i \phi^{ext}(\vec{r}_i) \tag{2.4}$$

one has to consider the grand canonical partition function Z_{gr} given by

$$Z_{gr} = 1 + \sum_{N=1}^{\infty} z^N \, Z_N \tag{2.5}$$

with z the activity, related to the chemical potential μ by

$$z = e^{\beta\mu} \tag{2.6}$$

The grand potential is calculated from Z_{gr} as

$$\Omega = -k_B T \log Z_{gr} \tag{2.7}$$

The integration volume V in (2.3) defines the position space in which the particles are allowed to move. If the external potential becomes strongly repulsive near the boundaries of V, the available position space is effectively defined by this potential since it prevents particles from intruding up to the boundaries. The volume is then bounded by soft walls and the precise location of the boundaries of V does not influence the physical behaviour of the system. If there is no external potential to prevent the particles from reaching the boundaries of V, the volume is bounded by hard walls. In this case, the boundaries of V, i.e. the position of the hard walls, can not be changed without changing the physical behaviour of the system. In general, the volume can be bounded by a combination of soft and hard walls.

Schofield and Henderson considered the change in the partition function under an infinitesimal deformation of the integration volume V. The deformation is described by an infinitesimally small displacement field $\vec{u}(\vec{r})$ which shifts the boundaries of V from their original positions $\{\vec{r}\}$ to new positions $\{\vec{r} + \vec{u}(\vec{r})\}$. We consider only cases in which ϕ^{ext} is not affected by the application of a displacement field which implies that any soft wall remains in place and the deformation affects the hard walls only. The change in grand potential can, up to order u, be described by the one and two-particle correlation function

$$\mathrm{d}\Omega = \int_V \mathrm{d}\vec{r}\,\{-k_BT\;\nabla\cdot\vec{u}(\vec{r}) + \vec{u}(\vec{r})\cdot\nabla\phi^{ext}(\vec{r})\;\}\;n(\vec{r})$$

$$+\frac{1}{2}\int_V \mathrm{d}\vec{r}_1\,\mathrm{d}\vec{r}_2\;\{\;\vec{u}(\vec{r}_1) - \vec{u}(\vec{r}_2)\;\}\;\frac{\vec{r}_{12}}{r_{12}}\;\phi'(r_{12})\;n_2(\vec{r}_1,\vec{r}_2) \tag{2.8}$$

However, it can equally well be described$^{7)}$ by the pressure tensor (2.1)

$$\mathrm{d}\Omega = -\int_V \mathrm{d}\vec{r}\,\{\;\overset{\rightrightarrows}{p}(\vec{r}):\nabla\vec{u}(\vec{r}) - n(\vec{r})\;\vec{u}(\vec{r})\cdot\nabla\phi^{ext}(\vec{r})\}$$

$$+\int_{\partial V}\mathrm{d}\vec{S}\cdot\{\;\overset{\rightrightarrows}{p}(\vec{r}) - k_BT\;n(\vec{r})\;\overset{\rightrightarrows}{I}\;\}\cdot\vec{u}(\vec{r}) \tag{2.9}$$

The second integral is over the surface of V. If the surface is shielded by a soft wall, the density at the surface will be zero since particles never reach the boundary of V in that case. Therefore, for any reasonable choice of contour, the pressure tensor will also be zero at a soft wall and thus, soft walls do not contribute to the surface integral. At a hard wall, the pressure tensor $\overset{\rightrightarrows}{p}(\vec{r})$ becomes equal to $k_BT\;n(\vec{r})\;\overset{\rightrightarrows}{I}$ for a large class of contours. Each contour which does not intersect the wall, belongs to this class. Note that the IK and the Harasima tensor both fulfill this condition (if the wals are in the x-y, x-z or y-z plane). Therefore, for this class of tensors, hard walls also do not contribute to the surface integral which then does not contribute to dΩ at all. So the change in grand potential is, up to first order in u, fully given by

$$\mathrm{d}\Omega = -\int_V \mathrm{d}\vec{r}\,\{\;\overset{\rightrightarrows}{p}(\vec{r}):\nabla\vec{u}(\vec{r}) - n(\vec{r})\;\vec{u}(\vec{r})\cdot\nabla\phi^{ext}(\vec{r})\} \tag{2.10}$$

if the pressure tensor at a hard wall ∂V_h reduces to

$$\overset{\rightrightarrows}{p}(\vec{r},\,\partial V_h) = k_BT\;n(\vec{r},\,\partial V_h)\;\overset{\rightrightarrows}{I} \tag{2.11}$$

We will restrict ourselves to tensors satisfying (2.11) in the remaining part of this paper, which means that only reasonably simple contours will be considered, typical examples of which are the IK and the Harasima contour.

Equation (2.10) is what we referred to as the "pressure route" to dΩ. The "density route" to dΩ is easily obtained from (2.9) if the combination $n\nabla\phi^{ext}$ is replaced by $-\nabla\cdot\overset{\rightrightarrows}{p}$, in accordance with (2.2). Partial integration of the resulting term gives

$$\mathrm{d}\Omega = -k_BT\int_{\partial V}\mathrm{d}\vec{S}\cdot\vec{u}(\vec{r})\;n(\vec{r}) \tag{2.12}$$

which expresses dΩ entirely in terms of the density at the wall. The equation shows that if the volume is bounded by soft walls everywhere, the grand potential does not change since the density vanishes at a soft wall. This must be so because in that case the boundaries of V can be distorted without changing the physical behaviour of the system. Equation (2.12) also shows that $d\Omega$ does not depend on the value of $\vec{u}$ in the interior of V. This reflects the fact that the deformation is determined by the value of $\vec{u}$ at the boundary of V only. In particular, Ω does not change if $\vec{u}$ vanishes at the boundary of V since in that case, the integration volume is not distorted at all. Equations (2.8), (2.10) and (2.12) denote three different but equally valid ways to express the change in grand potential under a deformation $\vec{u}$ of the boundaries of the fluid.

3. The definition of the surface and line tension.

Consider a fluid in a three dimensional, rectangular box which consists of hard walls. The grand potential of the fluid is defined by (2.3)-(2.7) with $\phi^{ext}(\vec{r}) = 0$. As we mentioned in section 1, the surface tension γ_h of the hard walls and the line tension τ_{hh} of the edges of the box can be defined from the change in the grand potential under a well chosen deformation of the box. An alternative definition of these quantities is obtained from a decomposition of the grand potential in terms of the order of the volume V, the size of the surface A_h, and the length of the edges L_{hh} of the box

$$\Omega = \Omega_V + \Omega_S + \Omega_E \tag{3.1}$$

Expansion (3.1) could become ambiguous if p and γ_h depend too strongly on the system size, e.g. approach their thermodynamic value inversely proportional to the linear size of the system. If, however, p and γ_h in a finite system are defined in terms of local quantities such as in (1.2) and (1.4), it is reasonable to assume that the influence of the size of the system is exponentially small. This assumption does probably not hold near criticality where the distinction between pressure and surface tension should be carefully reanalysed, which is beyond the scope of this paper.

To be complete, we should have added a term of the order 1 to (3.1) to include the contributions of the corners of the box to the grand potential. Such contributions however, will not be studied in this article and therefore we neglect them. Ω_V, Ω_S and Ω_E define the pressure, surface tension and line tension

$$\Omega_V = -p\ V \tag{3.2}$$

$$\Omega_S = \gamma_h\ A_h \tag{3.3}$$

$$\Omega_E = \tau_{hh}\ L_{hh} \tag{3.4}$$

The geometry of the box is the geometry of the integration volume in (2.3). Changes in the volume induce changes in the grand potential. Consequently, the proportionality factors p, γ_h and τ_{hh} are unambiguously defined.

These notions may appear somewhat trivial but more care is needed when soft walls are involved. Consider the same box as before with one of the hard walls, taken to be in the plane $z=0$, replaced by a soft wall. Contributions from the hard wall to the grand potential must now be distinguished from contributions from the soft wall

$$\Omega_S = \gamma_s A_s + \gamma_h A_h \tag{3.5}$$

with γ_s and A_s the surface tension and area of the soft wall. Similarly, the contributions from the edges formed by two hard walls must be distinguished from the contributions from the edges formed by a hard and a soft wall

$$\Omega_E = \tau_{sh} L_{sh} + \tau_{hh} L_{hh} \tag{3.6}$$

with τ_{sh} and L_{sh} the line tension and length of the edges formed by a hard and a soft wall. Contrary to the previous case, the lower limit on the z-integrations in (2.3) can be shifted without affecting Z_N. The geometry of the box however, does change under such a shift. If the lower boundary is shifted from $z=0$ to $z=\delta z$, the geometric changes in the box are

$$\delta V = -A_s \delta z, \quad \delta A_s = 0, \quad \delta A_h = -L_{sh} \delta z,$$
$$\delta L_{sh} = 0, \quad \delta L_{hh} = -4 \delta z \tag{3.7}$$

so

$$\delta\Omega_V = p \, \delta z \, A_s \tag{3.8}$$
$$\delta\Omega_S = \delta\gamma_s A_s - \gamma_h \delta z L_{sh} \tag{3.9}$$
$$\delta\Omega_E = \delta\tau_{sh} L_{sh} - 4 \tau_{hh} \delta z \tag{3.10}$$

Note that p, γ_h and τ_{hh} do not change because they were completely specified by the temperature and the chemical potential which remain of course unaltered by the shift δz in the boundary of the box. Since Z_N does not change, the grand potential of the fluid does not change. Adding (3.8), (3.9) and (3.10) gives

$$\delta\Omega = (p\delta z + \delta\gamma_s) A_s + (\gamma_h \delta z - \delta\tau_{sh}) L_{sh} + O(1) = 0 \tag{3.11}$$

In (3.11) we have neglected the term $\tau_{hh}\delta z$ which is of the order 1. The two terms in (3.11) are of a different order of magnitude and must vanish seperately

$$\delta\gamma_s = -p \, \delta z \tag{3.12}$$
$$\delta\tau_{sh} = \gamma_h \, \delta z \tag{3.13}$$

These equations demonstrate that the magnitude of γ_s and τ_{sh} depends on the location of the lower boundary $z=0$ of the box. The dependence is trivial in the sense that e.g. γ_s varies linearly with the position of the boundary with a coefficient which is not an intrinsic property of the surface but can be determined from the bulk state of the fluid alone. Note also that in e.g. the study of surface phenomena at a fixed wall the absolute value of the surface tension is never of importance but only the difference in surface tension between competing interfaces. For instance in the wetting problem, the coexisting liquid and vapor phase, competing to wet the wall, both have the same bulk pressure p and thus the difference in surface tension is independent of the location of the lower boundary $z=0$. Although the dependence of γ_s and τ_{sh} on the location of the boundary forces one to treat the boundary carefully, they remain central parameters in the description of interfaces and contact lines respectively.

4. Density expressions.

Relations between thermodynamic and microscopic quantities of the fluid will be obtained from deformations of the box which contains the fluid. The box we will use throughout this paper has dimensions $0 \le x,y,z \le L$. The wall in the plane $z=0$ is the wall of interest. It will taken to be a hard wall, a structureless soft wall or a structured soft wall. The five remaining walls will always taken to be hard walls. The box is deformed according to the displacement field

$$\vec{u}(\vec{r}) = \lambda\ (\, x-L,\ y-L,\ z\,) \tag{4.1}$$

The parameter λ makes $\vec{u}$ infinitesimally small. This displacement field transforms the box from a cube with edge length L to a cube with edge $(1+\lambda)\ L$. To obtain density expressions, expression (2.12) for the change in grand potential is exploited which expresses the change in the density at the walls

$$d\Omega = -k_B T \int_{\partial V} d\vec{S}\cdot\vec{u}(\vec{r})\ n(\vec{r}) \tag{4.2}$$

The product $d\vec{S}\cdot\vec{u}$ vanishes at the planes $x=L$, $y=L$, and $z=0$. Only the three remaining walls contribute to the integral (4.2).

4.1 Hard wall.

First, we take the wall in the plane $z=0$ to be a hard wall. The change in grand potential is then given by

$$d\Omega = -p\ dV + \gamma_h\ dA_h + \tau_{hh}\ dL_{hh} \tag{4.3}$$

With displacement field (4.1), the changes are

$$dV = 3\lambda\ L^3, \qquad dA_h = 12\lambda\ L^2, \qquad dL_{hh} = 12\lambda\ L \tag{4.4}$$

The thermodynamic expression (4.3) for $d\Omega$ has to be compared with the microscopic expression (4.2). The three walls that contribute to (4.2), give the same contribution. Take the wall $x=0$ as exemplary

$$d\Omega = -3\ k_B T\ \lambda\ L \int_0^L dy \int_0^L dz\ n(\,0,\ y,\ z\,) \tag{4.5}$$

Note that the thermodynamic expression (4.3) consists of different orders of L. The term of order L^3 determines p, the term of order L^2 γ_h and the term of order L determines τ_{hh}. We decompose (4.5) also in orders of L. The decomposition is obtained from a decomposition of the density. Define the density at the wall, n_w

$$n_w(\,y,\ z\,) = n(\,0,\ y,\ z\,) \tag{4.6}$$

This density has a constant value n_0 far away from the edges and corners at the wall $x=0$. The density is distorted by the presence of neighboring walls within some microscopic length ζ of the edges. The distortion near an edge, far away from a corner, is denoted Δn_h. The additional distortions near a corner are denoted Δn_{hh}. The decomposition of n_w reads

$$n_w(\, y,\, z) \;=\; n_0 \;+\; \Delta n_h(y) \;+\; \Delta n_h(z) \;+\; \Delta n_{hh}(y,z) \tag{4.7}$$

where $\Delta n_h(y)$ denotes the correction near an edge formed with a wall in the $x-z$ plane, $\Delta n_h(z)$ the correction near an edge formed with a wall in the $x-y$ plane. A correction term vanishes if its argument, or one of its arguments, is chosen far away from the edges. We denote such positions, $\zeta << y,z < L/2$, as y,z approaching infinity. Taking e.g. y and z to infinity, (4.7) gives the definition of n_0

$$n_0 \;=\; n_w(\infty,\infty) \tag{4.8}$$

Taking only y to infinity, (4.7) gives the definition of $\Delta n_h(z)$

$$\Delta n_h(z) \;=\; n_w(\infty,\; z) \;-\; n_0 \tag{4.9}$$

while Δn_{hh} is defined by (4.7) itself. Substitution of decomposition (4.7) in (4.5) gives

$$\mathrm{d}\Omega \;=\; -\lambda\; k_B T\; 3L\; \{\; \int_0^L \mathrm{d}y\, \mathrm{d}z\; n_0 \;+\; 2 \int_0^\infty \mathrm{d}y \int_0^L \mathrm{d}z\; \Delta n_h(y) \;+\; 2 \int_0^\infty \mathrm{d}z \int_0^L \mathrm{d}y\; \Delta n_h(z)$$
$$+\; 4 \int_0^\infty \mathrm{d}y \int_0^\infty \mathrm{d}z\; \Delta n_{hh}(y,z) \;\} \tag{4.10}$$

The factor 2 in front of the integral over Δn_h accounts for the fact that there are two walls in both the $x-z$ and $x-y$ plane bordering on the wall at $x=0$. The factor 4 in front of the integral over Δn_{hh} accounts for the fact that there are four corners at this wall. The symmetry between the walls implies that the integral over $\Delta n_h(y)$ gives the same contribution to $\mathrm{d}\Omega$ as the integral over $\Delta n_h(z)$. Decomposition (4.10) is the decomposition of $\mathrm{d}\Omega$ in orders of L

$$\mathrm{d}\Omega = -\lambda\, k_B T\, 3L\, \{\, L^2\, n_0 + 4L \int_0^\infty \mathrm{d}z\, \Delta n_h(z) + 4 \int_0^\infty \mathrm{d}y\, \mathrm{d}z\, \Delta n_{hh}(y,z)\, \} \tag{4.11}$$

comparison with (4.3) shows

$$p \;=\; k_B T\; n_0 \tag{4.12}$$

$$\gamma_h \;=\; -k_B T \int_0^\infty \mathrm{d}z\;\; \Delta n_h(z) \tag{4.13}$$

$$\tau_{hh} \;=\; -k_B T \int_0^\infty \mathrm{d}y \int_0^\infty \mathrm{d}z\;\; \Delta n_{hh}(y,z) \tag{4.14}$$

which are the desired density expressions. The first of these was already quoted in (1.1). It is seen to be the first of a hierachy of three which relates the pressure, suface tension and line tension to the density at a hard wall.

4.2 Soft wall.

We replace the hard wall in the plane $z=0$ by a structureless, soft wall and repeat the calculation of the previous section. One can now question whether the density at a hard wall, bordering at the soft wall at $z=0$, is still related to e.g. the surface tension of this wall. The calculation shows that this is indeed the case.

One has to distinguish between the soft wall with area A_s and surface tension γ_s and the hard walls in the calculation. One also has to distinguish between the edges formed by the soft and a hard wall, with total length L_{sh} and line tension τ_{sh}, and the edges formed by two hard walls. A similar distinction has to be made between the corners Apart from the replacement of the hard wall, the box and displacement field are the same as in the previous section. The thermodynamic expression for the change in grand potential reads

$$d\Omega = -p\, dV + \gamma_s\, dA_s + \gamma_h\, dA_h + \tau_{sh}\, dL_{sh} + \tau_{hh}\, dL_{hh} \tag{4.15}$$

The change in volume is the same as previously, the other changes in the geometry are

$$\begin{aligned} dA_s &= 2\lambda\, L^2, \quad & dA_h &= 10\lambda\, L^2, \\ dL_{sh} &= 4\lambda\, L, \quad & dL_{hh} &= 8\lambda\, L \end{aligned} \tag{4.16}$$

Expression (4.15) is again compared with (4.2). The three walls that contribute to the integral (4.2) no longer contribute equally. The wall at $z=L$ gives the same contribution as previously, i.e. one third of (4.3). But the contribution of the walls at $x=0$ and $y=0$ will be different since they border at a soft wall now. Their contributions to (4.2) however, will still be equal to one another. Take the wall at $x=0$ as exemplary

$$d\Omega = \lambda\,\{-p\,L^3 + 4\gamma_h\,L^2 + 4\tau_{hh}\,L - 2\,k_BT\,L \int_0^L dy \int_0^L dz\; n(0,y,z)\,\} \tag{4.17}$$

$$\equiv d\Omega_1 + d\Omega_2 \tag{4.18}$$

where $d\Omega_2$ refers to the integral in (4.17). The density at the wall $x=0$, $n_w(y,z)$, is decomposed as in (4.7). The influence of the soft wall on the density near the edge with the soft wall is denoted as Δn_s, The influence of a corner formed with the soft and a hard wall is denoted as Δn_{sh}. The decomposition of the density in the corner $y,z \geq 0$ reads

$$n_w(y,z) = n_0 + \Delta n_s(z) + \Delta n_h(y) + \Delta n_{sh}(y,z) \tag{4.19}$$

The decomposition of the integral $d\Omega_2$ becomes

$$d\Omega_2 = -\lambda\, k_BT\, 2L\,\{\, L^2\, n_0 + L \int_0^\infty dz\, \Delta n_s(z) + L \int_0^\infty dz\, \Delta n_h(z) + 2L \int_0^\infty dy\, \Delta n_h(y)$$

$$+ 2 \int_0^\infty dy \int_0^\infty dz \; \Delta n_{sh}(y,z) + 2 \int_0^\infty dy \int_0^\infty dz \; \Delta n_{hh}(y,z) \; \} \tag{4.20}$$

with the aid of the density expressions (4.12)-(4.14)

$$\begin{aligned} d\Omega_2 = \lambda \; \{ & -2p \, L^3 + 6\gamma_h \, L^2 + 4\tau_{hh} \, L \\ & -k_B T \; 2L^2 \int_0^\infty dz \; \Delta n_s(z) - k_B T \; 4L \int_0^\infty dy \int_0^\infty dz \; \Delta n_{sh}(y,z) \; \} \end{aligned} \tag{4.21}$$

Adding $d\Omega_1$ and $d\Omega_2$, we get

$$\begin{aligned} d\Omega = \; & \lambda \; \{ -3p \, L^3 + 10\gamma_h \, L^2 + 8\tau_{hh} \, L \; \} \\ & -\lambda \; k_B T \; \{ \; 2L^2 \int_0^\infty dz \; \Delta n_s(z) + 4L \int_0^\infty dy \int_0^\infty dz \; \Delta n_{sh} \; (y,z) \; \} \end{aligned} \tag{4.22}$$

Comparison with (4.15) gives the density expressions

$$\gamma_s = -k_B T \int_0^\infty dz \; \Delta n_s(z) \tag{4.23}$$

$$\tau_{sh} = -k_B T \int_0^\infty dy \int_0^\infty dz \; \Delta n_{sh}(y,z) \tag{4.24}$$

The density at a hard wall near an edge formed with a soft wall, is related to the surface tension of the soft wall. The density at a hard wall near a corner formed with a second hard wall and a soft wall, is related to the line tension of the edge formed by the soft and the hard wall. The structure of (4.23) and (4.24) is exactly the same as the structure of (4.13) and (4.14).

In general, we can state that the deviations of the density at a hard wall near an edge formed by the hard wall and a second wall are related to the surface tension of that second wall. This second wall can be either a hard or a soft wall. The deviations of the density near a corner formed by the hard wall and two other walls is related to the line tension of the edge formed by the other two walls. This relation has been proven for the case that the other two walls are hard and for the case that one of them is hard and the other soft. Using the same method, one easily finds that it also holds for the case that the other two walls are both soft.

We conclude this section with a consideration of the remark we made in section 3 about the dependence of γ_s and τ_{sh} on the lower boundary $z=0$ assigned to the system. The dependence is stated explicitly in equations (3.12) and (3.13). It should be possible to recognize the same dependence in the microscopic definitions of γ_s and τ_{sh}, (4.23) and (4.24). We have to inspect how these definitions change if the lower boundary $z=0$ is shifted with an amount δz. At $z=0$, the integrands become

$$\Delta n_s(\, 0) = -n_0 \tag{4.25}$$

$$\Delta n_{sh}(\, y,\, 0) \;=\; -\Delta n_h(y) \tag{4.26}$$

Therefore, γ_s and τ_{sh} change under the shift δz

$$\delta\gamma_s \;=\; -k_B T \; n_0 \; \delta z \tag{4.27}$$

$$\delta\tau_{sh} \;=\; -k_B T \;\delta z \int\limits_0^\infty dy \;\Delta n_h(y) \tag{4.28}$$

The density expressions (4.12) and (4.13) for the density at a hard wall show that these changes are equal to those in (3.12) and (3.13).

Density expressions do not only exist for hard walls. They can be derived for soft walls too from a deformation which also shifts these walls. In that case, the displacement field does not only affect the boundaries of V but also the external potential which forms the soft wall. An extra term must be added to (2.12) to account for this shift and density expressions can then be derived from the modified (2.12) in the way demonstrated here. As an example, one easily notices that the relation between the pressure and the density near a structureless, soft wall is given by

$$p \;=\; -\int\limits_0^\infty dz \;\; n(z)\;\; \frac{\partial}{\partial z} \;\; \phi^{ext}(z) \tag{4.29}$$

since the r.h.s. denotes the force per unit of area which the wall exerts at the fluid.

5. Pressure expressions for the surface and line tension: hard wall.

In this section, we exploit route (2.10) to the change in grand potential which leads to relations between thermodynamic quantities and the pressure tensor of the fluid. The box and displacement field are the same as in section 4. The wall in the plane $z=0$ is taken to be a hard wall in this section.

The thermodynamic expression for $d\Omega$ is given by (4.3) while on the other hand, equation (2.10) with $\phi^{ext}(\vec{r}) \;=\; 0$, states

$$d\Omega \;=\; -\int\limits_V d\vec{r} \;\overset{\Rightarrow}{p}(\vec{r}) : \nabla\vec{u}(\vec{r}) \tag{5.1}$$

With displacement field (4.1), the tensor $\nabla\vec{u}$ has the simple form

$$\nabla\vec{u}(\vec{r}) \;=\; \lambda \; \overset{\Rightarrow}{I} \tag{5.2}$$

Our strategy is the same as in the previous section: we split the microscopic expression (5.1) in orders of L. On comparison with (4.3), the term of order L^2 gives the microscopic definition of γ_h, the term of order L the definition of τ_{hh}. The decomposition of (5.1) in orders of L is obtained from a decomposition of the pressure tensor.

This decomposition is similar to the decomposition of n_w of the previous section. The tensor is translationally invariant and isotropic in the bulk fluid

$$\overset{\rightrightarrows}{p}_B = p\,\overset{\rightrightarrows}{I} \tag{5.3}$$

where p denotes as usual the bulk pressure. Near the walls, within some microscopic length ζ, $\overset{\rightrightarrows}{p}$ deviates from $\overset{\rightrightarrows}{p}_B$. The deviation near a wall, far away from edges and corners, is denoted as $\Delta\overset{\rightrightarrows}{p}_h$. The additional deviations near an edge are denoted as $\Delta\overset{\rightrightarrows}{p}_{hh}$. The influence of the corners is denoted as $\Delta\overset{\rightrightarrows}{p}_{hhh}$. The decomposition of $\overset{\rightrightarrows}{p}$ in the corner $x,y,z \geq 0$ reads

$$\begin{aligned}\overset{\rightrightarrows}{p}(\vec{r}) &= \overset{\rightrightarrows}{p}_B + \Delta\overset{\rightrightarrows}{p}_h(x) + \Delta\overset{\rightrightarrows}{p}_h(y) + \Delta\overset{\rightrightarrows}{p}_h(z) \\ &+ \Delta\overset{\rightrightarrows}{p}_{hh}(x,y) + \Delta\overset{\rightrightarrows}{p}_{hh}(x,z) + \Delta\overset{\rightrightarrows}{p}_{hh}(y,z) + \Delta\overset{\rightrightarrows}{p}_{hhh}(x,y,z)\end{aligned} \tag{5.4}$$

The correction terms $\Delta\overset{\rightrightarrows}{p}$ vanish if one of their arguments is taken far away from the walls. We denote such positions, $\zeta << x,y,z < L/2$, as x,y,z approaching infinity. With x, y and z in this limit, (5.4) becomes the definition of $\overset{\rightrightarrows}{p}_B$

$$\overset{\rightrightarrows}{p}_B = \overset{\rightrightarrows}{p}\,(\infty,\infty,\infty) \tag{5.5}$$

Taking x and y to infinity, one obtains the definition of $\Delta\overset{\rightrightarrows}{p}_h$

$$\Delta\overset{\rightrightarrows}{p}_h(z) = \overset{\rightrightarrows}{p}(\infty,\infty,\, z) - \overset{\rightrightarrows}{p}_B \tag{5.6}$$

Taking only x to infinity, one obtains the definition of $\Delta\overset{\rightrightarrows}{p}_{hh}$

$$\Delta\overset{\rightrightarrows}{p}_{hh}(\,y,\,z) = \overset{\rightrightarrows}{p}(\infty,\,y,\,z) - \overset{\rightrightarrows}{p}_B - \Delta\overset{\rightrightarrows}{p}_h(\,y) - \Delta\overset{\rightrightarrows}{p}_h(\,z) \tag{5.7}$$

The definition of $\Delta\overset{\rightrightarrows}{p}_{hhh}$ is (5.4) itself. The decomposition (5.4) of the pressure tensor is inserted in (5.1). This integral splits in an integral involving $\overset{\rightrightarrows}{p}_B$, 6 integrals involving $\Delta\overset{\rightrightarrows}{p}_h$ (resulting from the deviations of $\overset{\rightrightarrows}{p}$ near the walls), 12 integrals involving $\Delta\overset{\rightrightarrows}{p}_{hh}$ (from the deviations near the edges) and 8 integrals involving $\Delta\overset{\rightrightarrows}{p}_{hhh}$ (from the deviations near the corners). The 6 integrals involving $\Delta\overset{\rightrightarrows}{p}_h$ give the same contribution to $\mathrm{d}\Omega$ by symmetry. We take the deviations near the wall $z=0$ as exemplary. Similarly, we take the deviations near the edge formed by the wall at $z=0$ and $y=0$ as exemplary for the 12 edges. The corner formed by these two walls and the wall at $x=0$ is taken as exemplary for the 8 corners. The decomposition of (5.1) reads

$$\begin{aligned}\mathrm{d}\Omega = -\lambda\,\{ &\int_0^L \mathrm{d}x \int_0^L \mathrm{d}y \int_0^L \mathrm{d}z\; \overset{\rightrightarrows}{p}_B : \overset{\rightrightarrows}{I} + 6 \int_0^L \mathrm{d}x \int_0^L \mathrm{d}y \int_0^\infty \mathrm{d}z\; \Delta\overset{\rightrightarrows}{p}_h(z) : \overset{\rightrightarrows}{I} \\ &+ 12 \int_0^L \mathrm{d}x \int_0^\infty \mathrm{d}y \int_0^\infty \mathrm{d}z\; \Delta\overset{\rightrightarrows}{p}_{hh}(y,z) : \overset{\rightrightarrows}{I} + 8 \int_0^\infty \mathrm{d}x \int_0^\infty \mathrm{d}y \int_0^\infty \mathrm{d}z\; \Delta\overset{\rightrightarrows}{p}_{hhh}(x,y,z) : \overset{\rightrightarrows}{I}\,\}\end{aligned} \tag{5.8}$$

$$\equiv \mathrm{d}\Omega_B + \mathrm{d}\Omega_h + \mathrm{d}\Omega_{hh} + \mathrm{d}\Omega_{hhh} \tag{5.9}$$

(5.9) is the expansion of $\mathrm{d}\Omega$ in orders of L. With the definition of $\overset{\rightrightarrows}{p}_B$, (5.3), the first term is easily calculated

$$d\Omega_B = -\lambda\, p\, L^3 \tag{5.10}$$

Compared with the term of order L^3 in (4.3), (5.10) shows that the constant p which defines $\vec{\vec{p}}_B$ is indeed equal to the pressure of the fluid. The second term, $d\Omega_h$, reads

$$d\Omega_h = -6\lambda\, L^2 \int_0^\infty dz\ \{\ \Delta p_h^{xx}(z) + \Delta p_h^{yy}(z) + \Delta p_h^{zz}(z)\ \} \tag{5.11}$$

which is of the order L^2. The third term, $d\Omega_{hh}$, reads

$$d\Omega_{hh} = -12\lambda\, L \int_0^\infty dy \int_0^\infty dz\ \{\ \Delta p_{hh}^{xx}(y,z) + \Delta p_{hh}^{yy}(y,z) + \Delta p_{hh}^{zz}(y,z)\ \} \tag{5.12}$$

which is of order L. The last term, $d\Omega_{hhh}$, reads

$$d\Omega_{hhh} = -8\lambda \int_0^\infty dx \int_0^\infty dy \int_0^\infty dz\ \{\ \Delta p_{hhh}^{xx}(x,y,z) + \Delta p_{hhh}^{yy}(x,y,z) + \Delta p_{hhh}^{zz}(x,y,z)\ \} \tag{5.13}$$

which is of the order L^0. First, we will discuss the term $d\Omega_h$ to extract the definition of γ_h.

Comparison of $d\Omega_h$ with the term of order L^2 in the thermodynamic expression for $d\Omega$, (4.3), gives for the microscopic definition of γ_h

$$\gamma_h = \frac{1}{2} \int_0^\infty dz\ \{\ \Delta p_h^{xx}(z) + \Delta p_h^{yy}(z) + \Delta p_h^{zz}(z)\ \} \tag{5.14}$$

This expression can be simplified. It can be shown that the term Δp_h^{zz} vanishes (see (A.1) in appendix A) while $\Delta p_h^{xx}(z) = \Delta p_h^{yy}(z)$ by symmetry. We define

$$\Delta p_h^{xx}(z) = \Delta p_h^{yy}(z) \equiv \Delta p_h^{T}(z) \tag{5.15}$$

and (5.14) simplifies to

$$\gamma_h = -\int_0^\infty dz\ \Delta p_h^{T}(z) \tag{5.16}$$

In terms of p^T and p it reads

$$\gamma_h = -\int_0^\infty dz\ (\ p^T(\infty,\infty,z) - p) \tag{5.17}$$

This form is the usual expression$^{4)}$ for γ_h. It was already mentioned, in a slightly different notation, in (1.4). Before we proceed to the term of order L in $d\Omega$, we will derive an extension of (5.16) or (5.17).

The path of integration in (5.16) and (5.17) must be taken far away from the edges of the system. The deviation of p^T from its bulk value p results from the presence of the wall at $z=0$ only. We ask the question what happens if the path of integration is chosen close to an edge and the influence of the edge on $\overset{\rightrightarrows}{p}$ is taken into account. Consider as example the edge formed by the walls at $y=0$ and $z=0$. Define

$$\gamma_h^{yy}(y) = -\int_0^\infty dz \; \{ \; \Delta p_h^{yy}(z) + \Delta p_{hh}^{yy}(y,z) \; \} \tag{5.18}$$

The integrand of (5.18) reads

$$\Delta p_h^{yy}(z) + \Delta p_{hh}^{yy}(y,z) = p^{yy}(\infty,y,z) - p \tag{5.19}$$

Identity (A.2) of appendix A shows that

$$\gamma_h^{yy}(y) = \gamma_h \tag{5.20}$$

for all distances y. At y large, the term Δp_{hh}^{yy} vanishes and (5.18) reduces to (5.16). At the hard wall $y=0$, p^{yy} is equal to $k_B T$ times the density at the wall, c.f. (2.11), and (5.18) becomes the density expression (4.13). Expression (5.18) is a generalisation which contains both the pressure expression (5.17), at $y=\infty$, and the density expression (4.13), at $y=0$.

We proceed with the term of order L in (5.9), $d\Omega_{hh}$ given by (5.12). Comparison with the term of order L in the thermodynamic expression for the change in grand potential, (4.3), gives the microscopic definition of τ_{hh}

$$\tau_{hh} = -\int_0^\infty dy \int_0^\infty dz \; \{ \; \Delta p_{hh}^{xx}(y,z) + \Delta p_{hh}^{yy}(y,z) + \Delta p_{hh}^{zz}(y,z) \; \} \tag{5.21}$$

The second and third term in the integral vanish (see (A.2)) and the definition of τ_{hh} simplifies to

$$\tau_{hh} = -\int_0^\infty dy \int_0^\infty dz \; \Delta p_{hh}^{xx}(y,z) \tag{5.22}$$

which has precisely the same structure as the definition (5.16) of γ_h.

The plane of integration in (5.22) is taken far away from a corner: the integrand is determined by the presence of the edge alone. Analogous to the case of the surface tension, the plane of integration in (5.22) can be taken close to a corner. One can show this by defining

$$\tau_{hh}^{xx}(x) = -\int_0^\infty dy \int_0^\infty dz \; \{ \; \Delta p_{hh}^{xx}(y,z) + \Delta p_{hhh}^{xx}(x,y,z) \; \} \tag{5.23}$$

and demonstrating (see (A.3)) that $\tau^{xx}_{hh}(x)$ is independent of x:

$$\tau^{xx}_{hh}(x) = \tau_{hh} \tag{5.24}$$

In the limit that x is large, Δp^{xx}_{hhh} vanishes and (5.23) reduces to (5.22). At the wall $x=0$, p^{xx} satisfies (2.11) and (5.23) reduces to density expression (4.14). τ^{xx}_{hh} plays the same role for the line tension as γ^{yy}_{h} played for the surface tension. It can be regarded as an expression that interpolates between the density expression (4.14), at $x=0$, and the pressure expression (5.22), at $x=\infty$.

Finally, we consider the term of order L^0, $d\Omega_{hhh}$, in (5.9) which is defined in (5.12). Identity (A.3) tells that the integral over each term in the integrand of (5.12) vanishes

$$d\Omega_{hhh} = 0 \tag{5.25}$$

in accordance with the fact that no terms of the order L^0 appears in the thermodynamic expression for the change in grand potential, (4.3). These terms are absent because the corners are not deformed by displacement field (4.1).

6. Pressure expressions for the surface and line tension: soft wall.

In this section, we replace the hard wall in the plane $z=0$ by a structureless, soft wall and repeat the calculation of the previous section. The microscopic expression (2.10) for the change in grand potential contains the extra term $n\, \vec{u}\cdot\nabla\phi^{ext}$ as compared to (5.1). Using that the soft wall is structureless, i.e.

$$\frac{\partial}{\partial x}\,\phi^{ext}(\vec{r}) = \frac{\partial}{\partial y}\,\phi^{ext}(\vec{r}) = 0 \tag{6.1}$$

this term reads with displacement field (4.1),

$$\vec{u}(\vec{r})\cdot\nabla\phi^{ext}(\vec{r}) = \lambda\, z\, \frac{\partial}{\partial z}\,\phi^{ext}(z) \tag{6.2}$$

The pressure tensor is decomposed in the same fashion as in (5.4) in the previous section but one has to distinguish between distortions of $\vec{\vec{p}}$ near the hard walls and distortions near the soft wall. The distortions near the soft wall, far away from the corners and edges, are denoted $\Delta\vec{\vec{p}}_s$. The distortions near an edge formed by the soft and a hard wall are denoted $\Delta\vec{\vec{p}}_{sh}$. The distortions near a corner formed by two hard walls and the soft wall are denoted $\Delta\vec{\vec{p}}_{shh}$. Decomposition (5.4) is replaced by

$$\begin{aligned}\vec{\vec{p}}(\vec{r}) &= \vec{\vec{p}}_B + \Delta\vec{\vec{p}}_h(x) + \Delta\vec{\vec{p}}_h(y) + \Delta\vec{\vec{p}}_s(z)\\ &+ \Delta\vec{\vec{p}}_{hh}(x,y) + \Delta\vec{\vec{p}}_{sh}(x,z) + \Delta\vec{\vec{p}}_{sh}(y,z) + \Delta\vec{\vec{p}}_{shh}(x,y,z)\end{aligned} \tag{6.3}$$

The local density must also be decomposed. It turns out to be most convenient to decompose it slightly different from (6.3)

$$n(x,y,z) = n_s(z) + \Delta n_h(x) + \Delta n_h(y) + \Delta n_{hh}(x,y) + \Delta n_{sh}(x,z) + \Delta n_{sh}(y,z) + \Delta n_{shh}(x,y,z) \tag{6.4}$$

where $n_s(z)$ denotes the density at a distance z from the soft wall, not influenced by the hard walls. Taking x and y to infinity, (6.4) gives the definition

$$n_s(z) = n(\infty, \infty, z) \tag{6.5}$$

Δn_h is the correction we have to add to n_s if the density is evaluated close to a hard wall, far away from the edges and corners. Taking y and z to infinity yields

$$\Delta n_h(x) = n(x, \infty, \infty) - n_B \tag{6.6}$$

since n_s becomes equal to the bulk fluid density n_B far away from the soft wall. The remaining terms in (6.4) are defined similarly. Δn_{sh} denotes the correction near an edge formed by a hard and a soft wall, Δn_{hh} the correction near an edge formed by two hard walls, Δn_{shh} the correction near a corner formed by two hard walls and the soft wall. Finally, there exists the correction Δn_{hhh} in a corner formed by three hard walls. Note that the correction terms Δn as defined here should not be confused with the terms Δn of section 4.

Now that we have decomposed the density and the pressure tensor, we use them to decompose the change in the grand potential in orders L^n.

$$d\Omega = d\Omega_B + d\Omega_s + d\Omega_h + d\Omega_{sh} + d\Omega_{hh} + d\Omega_{shh} + d\Omega_{hhh} \tag{6.7}$$

with $d\Omega_B$ as in (5.8) and

$$d\Omega_s = -\int_0^L dx \int_0^L dy \int_0^\infty dz \; \{ \; \Delta\vec{\vec{p}}_s : \nabla\vec{u} - n_s \; \vec{u}\cdot\nabla\phi^{ext} \; \} \tag{6.8}$$

$$d\Omega_h = -5 \int_0^L dx \int_0^\infty dy \int_0^L dz \; \Delta\vec{\vec{p}}_h : \nabla\vec{u} \tag{6.9}$$

$$d\Omega_{sh} = -4 \int_0^L dx \int_0^\infty dy \int_0^\infty dz \; \{ \; \Delta\vec{\vec{p}}_{sh} : \nabla\vec{u} - (\; \Delta n_h + \Delta n_{sh} \;) \; \vec{u}\cdot\nabla\phi^{ext} \; \} \tag{6.10}$$

$$d\Omega_{hh} = -8 \int_0^\infty dx \int_0^\infty dy \int_0^L dz \; \Delta\vec{\vec{p}}_{hh} : \nabla\vec{u} \tag{6.11}$$

$$d\Omega_{shh} = -4 \int_0^\infty dx \int_0^\infty dy \int_0^\infty dz \; \{ \; \Delta\vec{\vec{p}}_{shh} : \nabla\vec{u} - (\; \Delta n_{hh} + \Delta n_{shh} \;) \; \vec{u}\cdot\nabla\phi^{ext} \; \} \tag{6.12}$$

$$d\Omega_{hhh} = -4 \int_0^\infty dx \int_0^\infty dy \int_0^\infty dz \; \Delta\vec{\vec{p}}_{hhh} : \nabla\vec{u} \tag{6.13}$$

We verify that all terms in the decomposition of $\vec{\vec{p}}$ and n appear in (6.8)-(6.13). The first term $\vec{\vec{p}}_B$ in the decomposition of $\vec{\vec{p}}$ is included in $d\Omega_B$. There is one correction term $\Delta\vec{\vec{p}}_s$

which is combined with n_s in $d\Omega_s$. There are five terms $\Delta\vec{\vec{p}}_h$, from the five hard walls. They contribute equally to $d\Omega$ and we took the plane $y=0$ as exemple to represent $d\Omega_h$. There are also five terms Δn_h. The product $\Delta n_h\ \vec{u}\cdot\nabla\phi^{ext}$ vanishes however along the wall at $z=L$ since ϕ^{ext} vanishes there. The four remaining terms Δn_h are combined with the four terms Δn_{sh} and the four terms $\Delta\vec{\vec{p}}_{sh}$ in $d\Omega_{sh}$ taking the edge formed by the walls at $z=0$ and $y=0$ as exemplary. There are eight terms $\Delta\vec{\vec{p}}_{hh}$ which are included in $d\Omega_{hh}$ with the edge formed by the walls at $x=0$ and $y=0$ as exemplary. There are also eight terms Δn_{hh} but the product $\Delta n_{hh}\ \vec{u}\cdot\nabla\phi^{ext}$ vanishes along the four edges formed by the wall at $z=L$. The four remaining terms are combined with the four terms Δn_{shh} and the four terms $\Delta\vec{\vec{p}}_{shh}$. Together, they form $d\Omega_{shh}$. The last terms, the four terms $\Delta\vec{\vec{p}}_{hhh}$, form $d\Omega_{hhh}$.

Note that it is necessary to take the combination $(\Delta n_h\ +\ \Delta n_{sh})$ in (6.10). The soft wall becomes infinitely repulsive at small values of z. The product $\vec{u}\cdot\nabla\phi^{ext}$ is therefore in general not integrable over small values of z. Only the combination $n\ \vec{u}\cdot\nabla\phi^{ext}$ can be integrated. The term Δn_{sh} is defined as

$$\Delta n_{sh}(y,z)\ =\ n(\infty,y,z)\ -\ n(\infty,\infty,z)\ -\ \Delta n_h(y) \tag{6.14}$$

The products $n(\infty,y,z)\ \vec{u}\cdot\nabla\phi^{ext}$ and $n(\infty,\infty,z)\ \vec{u}\cdot\nabla\phi^{ext}$ will both be integrable over small distances of z. The combination $\Delta n_h(y)\ \vec{u}\cdot\nabla\phi^{ext}$ however, will not be integrable. Therefore, the term $\Delta n_{sh}\vec{u}\cdot\nabla\phi^{ext}$ can in general not be integrated over z whereas the combination $(\Delta n_h\ +\ \Delta n_{sh})\ \vec{u}\cdot\nabla\phi^{ext}$ is integrable.

Similarly, it is the combination $(\Delta n_{hh}\ +\ \Delta n_{shh})\ \vec{u}\cdot\nabla\phi^{ext}$ which can be integrated and not the seperate terms.

Decomposition (6.7) is the expansion of $d\Omega$ in orders of L. The term $d\Omega_B$ is of the order L^3, $d\Omega_s$ and $d\Omega_h$ are of the order L^2, $d\Omega_{sh}$ and $d\Omega_{hh}$ are of the order L and $d\Omega_{shh}$ and $d\Omega_{hhh}$ of the order L^0. $d\Omega_B$ is the same as in the previous section. First, we analyse the terms of order L^2 to extract the microscopic definition of γ_s from them. (6.9) yields

$$d\Omega_h\ =\ -\lambda\ 5L^2 \int_0^\infty dy\ \{\ \Delta p_h^{xx}(y)\ +\ \Delta p_h^{yy}(y)\ +\ \Delta p_h^{zz}(y)\ \} \tag{6.15}$$

From (5.14) we find

$$d\Omega_h\ =\ \lambda\ \gamma_h\ 10L^2 \tag{6.16}$$

which also occurs in the thermodynamic expression (4.15) for $d\Omega$. Therefore, the definition of γ_s is indeed included in $d\Omega_s$. (6.8) gives for $d\Omega_s$

$$d\Omega_s\ =\ -\lambda\ L^2 \int_0^\infty dz\ \{\ \Delta p_s^T(z)\ +\ \Delta p_s^{zz}(z)\ -\ z\ n_s(z)\ \frac{\partial}{\partial z}\ \phi^{ext}(z)\ \} \tag{6.17}$$

Comparison with (4.15) yields the microscopic definition of γ_s

$$\gamma_s\ =\ -\int_0^\infty dz\ \{\ \Delta p_s^T(z)\ +\ \Delta p_s^{zz}(z)\ -\ z\ n_s(z)\ \frac{\partial}{\partial z}\ \phi^{ext}(z)\ \} \tag{6.18}$$

$$\equiv -\int_0^\infty \mathrm{d}z\ \Delta p_s^T(z) \ - \ I_1 \tag{6.19}$$

which differs from the microscopic expression (5.16) for γ_h by an extra integral I_1. One can however show that this integral vanishes (see (B.1) in appendix B). The microscopic expression for γ_s thus becomes

$$\gamma_s \ = \ -\int_0^\infty \mathrm{d}z\ \Delta p_s^T(z) \tag{6.20}$$

In terms of p^T and p, it reads

$$\gamma_s \ = \ -\int_0^\infty \mathrm{d}z\ \{\ p^T(\infty,\infty,\ z) \ - \ p\ \} \tag{6.21}$$

An alternative form is obtained if $-I_1$ in (6.19) is replaced by I_1, since I_1 is zero, and Δp_s^T, Δp_s^{zz} and n_s are expressed in p^T, p^{zz}, p and n

$$\gamma_s \ = \ -\int_0^\infty \mathrm{d}z\ \{\ p^T(\infty,\infty,\ z) \ - \ p^{zz}(\infty,\infty,\ z) \ + \ z\ n(\infty,\infty,\ z)\ \frac{\partial}{\partial z}\ \phi^{ext}(z)\ \} \tag{6.22}$$

Expressions (6.22) and (6.21) for the surface tension of a soft wall are frequently used⁶⁾. They can be extended in the same way as in the previous section. The path of integration in (6.20) is to be taken far away from the edges where the soft wall borders at a hard wall. As in the case of γ_h, one can show that the path of integration can as well be taken close to the edge. The distortions of p^T due to the neighborhood of the edge have no influence on the integral (5.17). If one defines analogous to (5.18)

$$\gamma_s^{yy}(y) \ = \ -\int_0^\infty \mathrm{d}z\ \{\ \Delta p_s^{yy}(z) \ + \ \Delta p_{sh}^{yy}(y,z)\ \} \tag{6.23}$$

where the integrand is given by (5.19), it follows from (B.3) that

$$\gamma_s^{yy}(y) \ = \ \gamma_s \tag{6.24}$$

for all distances y. Expression (6.23) reduces to (6.20) at large y where Δp_{sh}^{yy} vanishes and becomes equal to density expression (4.23) at $y=0$ where p^{yy} satisfies (2.11). As $\gamma_h^{yy}(y)$, $\gamma_s^{yy}(y)$ can be regarded as an expression for γ_s that interpolates between the density expression and the pressure expression for γ_s.

We proceed with the terms of order L in decomposition (6.7) of the change in grand potential. We start with the term $\mathrm{d}\Omega_{hh}$, (6.11).

$$\mathrm{d}\Omega_{hh} \ = \ -\lambda\ 8L \int_0^\infty \mathrm{d}y \int_0^\infty \mathrm{d}z\ \{\ \Delta p_{hh}^{xx}(z,y) \ + \ \Delta p_{hh}^{yy}(z,y) \ + \ \Delta p_{hh}^{zz}(z,y)\ \} \tag{6.25}$$

From (5.21)-(5.22) one has

$$d\Omega_{hh} = \lambda \; 8L \; \tau_{hh} \tag{6.26}$$

This contribution to $d\Omega$ occurs also in (4.15). The microscopic expression for τ_{sh} is therefore contained in $d\Omega_{sh}$ given by (6.10).

$$\begin{aligned} d\Omega_{sh} = -\lambda \; 4L \int_0^\infty dy \int_0^\infty dz \; \{ \; & \Delta p_{sh}^{xx}(y,z) + \Delta p_{sh}^{yy}(y,z) + \Delta p_{sh}^{zz}(y,z) \\ & - (\; \Delta n_h(y) + \Delta n_{sh}(y,z) \;) \; z \frac{\partial}{\partial z} \phi^{ext}(z) \; \} \end{aligned} \tag{6.27}$$

The integral over Δp_{sh}^{yy} vanishes, c.f. (B.3). Comparison with (4.15) gives the microscopic expression for τ_{sh}

$$\begin{aligned} \tau_{sh} = & -\int_0^\infty dy \int_0^\infty dz \; \Delta p_{sh}^{xx}(y,z) \\ & -\int_0^\infty dy \int_0^\infty dz \; \{ \Delta p_{sh}^{zz}(y,z) - (\; \Delta n_h(z) + \Delta n_{sh}(y,z) \;) \; z \frac{\partial}{\partial z} \phi^{ext}(z) \; \} \end{aligned} \tag{6.28}$$

$$\equiv -\int_0^\infty dy \int_0^\infty dz \; \Delta p_{sh}^{xx}(y,z) - I_2 \tag{6.29}$$

The structure of (6.29) differs from the definition of τ_{hh}, (5.22), in the extra term I_2. One can show again that I_2 is zero (see (B.2)) and the microscopic expression for τ_{sh} simplifies to

$$\tau_{sh} = -\int_0^\infty dy \int_0^\infty dz \; \Delta p_{sh}^{xx}(\; y, \; z) \tag{6.30}$$

As in the case of the surface tensions, the expression for τ_{sh} turns out to be of the same structure as the expression for τ_{hh}, (5.22). Finally, we ask once more the question what happens with the integral in (6.30) if the plane of integration is shifted towards a corner formed by a third hard wall and the influence of the corner on the tensor is taken into account. Define analogous to (5.23)

$$\tau_{sh}^{xx}(x) = -\int_0^\infty dy \int_0^\infty dz \; \{ \; \Delta p_{sh}^{xx}(\; y, \; z) + \Delta p_{shh}^{xx}(\; x, \; y, \; z) \; \} \tag{6.31}$$

and one finds from (B.4)

$$\tau_{sh}^{xx}(x) = \tau_{sh} \tag{6.32}$$

for all distances x. At large distances x, Δp_{shh}^{xx} vanishes and (6.31) reduces to (6.30). At the wall $x=0$, p^{xx} satisfies (2.11) and (6.31) becomes the density expression (4.24). Like

$\tau_{hh}^{xx}(x)$, $\tau_{sh}^{xx}(x)$ includes both the density expression and the pressure expression for τ_{sh}.

Finally, we have to evaluate the terms of order L^0 in (6.7). The term $d\Omega_{hhh}$ vanishes according to (A.3). The term $d\Omega_{shh}$, (6.12), is more cumbersome. With (B.4), this term simplifies to

$$d\Omega_{shh} = \lambda \int_0^\infty dx \int_0^\infty dy \int_0^\infty dz \; \{ \; \Delta p_{shh}^{zz}(x,y,z) - (\; \Delta n_{hh}(\; x, \; y) + \Delta n_{shh}(x,y,z) \;) \; z \; \frac{\partial}{\partial z} \; \phi^{ext}(z) \; \} \tag{6.33}$$

This integral is the third in a hierachy of which the first and second are the integrals (B.1) and (B.2). In the same way as it is shown that these integrals vanish, it can be proven that this integral vanishes, i.e. $d\Omega_{shh}$ vanishes. This means that there is no term of order L^0 in the change of grand potential, in accordance with the fact that this term is also absent in the thermodynamic expression (4.15) for $d\Omega$.

We conclude this section with a consideration of the dependence of γ_s and τ_{sh} on the lower boundary $z=0$ assigned to the system. This dependence was discussed in section 3 where it is made explicit in equations (3.12) and (3.13). The same dependence must be appear in the microscopic definitions of γ_s, (6.23), and τ_{sh}, (6.31). The integrand that appears in (6.23) takes the value $-p$ at $z=0$, c.f. (5.19). If we shift the lower boundary with an amount δz, the integral changes with an amount

$$\delta\gamma_s = -p \; \delta z \tag{6.34}$$

which is equal to (3.12). The integrand in (6.31) becomes at $z=0$

$$\Delta p_{sh}^{xx}(y,0) + \Delta p_{shh}^{xx}(x,y,0) = -\{ \; p^{xx}(x,y,\infty) - p \; \} \tag{6.35}$$

If we shift the lower boundary $z=0$ of integral (6.31) over a distance δz, the integral changes with an amount

$$\delta\tau_{sh} = -\delta z \int_0^\infty dy \; \{ \; p^{xx}(\; x, \; y,\infty) - p \; \} \tag{6.36}$$

Note that $p^{xx}(x,y,\infty)$ is the xx component of $\overset{\rightrightarrows}{p}$ in an edge formed by two hard walls. The integral is recognized as $\gamma_h^{xx}(x)$, the symmetric equivalent of $\gamma_h^{yy}(y)$ defined in (5.18)-(5.19)

$$\delta\tau_{sh} = \gamma_h^{xx}(x) \; \delta z \tag{6.37}$$

which equals with the use of (5.20)

$$\delta\tau_{sh} = \gamma_h \; \delta z \tag{6.38}$$

This is the result (3.13).

7. Surface tension of a structured wall.

Up till now, we have restricted ourselves to hard and structureless, soft walls. The case of a structured, soft wall will be treated in this section in which we focus on the pressure expressions. Density expressions also exist but are far less elegant than in the structureless case, as we discuss below. Moreover, the discussion will be restricted to the level of the surface tension alone since already at this level, the calculation is much more complicated than for the structureless wall.

The box and displacement field are the same as in the previous sections with the wall at $z=0$ replaced by a structured, soft wall. Such a wall is periodic and we denote the length of the period in the x-direction as a_x, the length in the y-direction as a_y. The change in grand potential upon the deformation equals

$$d\Omega = -p\ dV + \gamma_{st}(L)\ dA_{st} + \gamma_h\ dA_h + O(L) \tag{7.1}$$

$$\equiv d\Omega_B + d\Omega_{st} + d\Omega_h + O(L) \tag{7.2}$$

A_{st} denotes the surface of a structured wall, γ_{st} its surface tension (the index "st" stands for "structured"). The increase dA_{st} is the same as the increase dA_s in (4.16). Terms of the order L are neglected since we restrict the discussion to the level of the surface tension.

Because of the structure of the wall, the change in grand potential under an infinitesimal shift of the boundary planes at $x,y=0$ will depend on the location of these planes. The walls at $x=L$ and $y=L$ remain in place under displacement field (4.1). The shift defines a "partial surface tension" $\gamma_{st}(L)$. To obtain the "full" surface tension γ_{st} of the structured wall, one should consider an increase of A_{st} with an integer number of units of area $a_x \times a_y$. This increase is most easily visualised if $a_x = a_y = a$ in which case one can simply increase L with a periodic length a. For simplicity, we consider this case; the case $a_x \neq a_y$ presents no conceptual difficulties. From time to time, we will again distinguish in the notation between a_x and a_y to show what the result is for the general case.

Considering an increase of L with one period, the increase of A_{st} equals

$$\Delta A_{st} = 2a\ L + O(L^0) \tag{7.3}$$

and the surface tension of the structured wall reads

$$\gamma_{st} = \frac{1}{\Delta A_{st}} \int_L^{L+a} dL' \left| \frac{d\Omega_{st}}{dL'} \right| = \frac{1}{a} \int_L^{L+a} dL'\ \gamma_{st}(L') + O(L^{-1}) \tag{7.4}$$

using that $d\Omega_{st} = 2\lambda\ \gamma_{st}(L')\ L'^2$ and $dL' = \lambda\ L'$. The term of order L^{-1} vanishes in the thermodynamic limit.

If we try to obtain a density expression for the surface tension of a structured wall, we readily find that the density at the hard walls is related to $\gamma_{st}(L)$. Therefore, a density expression for γ_{st} also incorporates a shift of the walls over a complete periodic length. In other words, the density expression incorporates an average over all possible locations of the hard wall within a period a as in (7.4). This average makes the density expression far less elegant than the density expressions (4.13) and (4.23) for a structureless wall. This is the reason that we do not consider them further.

In the case of a structured, soft wall -following route (2.10) to the change in grand potential- (6.2) is replaced by

$$\vec{u}(\vec{r})\cdot\nabla\phi^{ext}(\vec{r}) = \lambda \{ (x-L)\frac{\partial}{\partial x}\phi^{ext}(\vec{r}) + (y-L)\frac{\partial}{\partial y}\phi^{ext}(\vec{r}) + z\frac{\partial}{\partial z}\phi^{ext}(\vec{r}) \} \quad (7.5)$$

The pressure tensor and density are decomposed as in the previous section. The decompositions in the corner $x,y,z \geq 0$ read, c.f. (6.3) and (6.4)

$$\begin{aligned} \overset{\rightrightarrows}{p}(x,y,z) &= \overset{\rightrightarrows}{p}_B + \Delta\overset{\rightrightarrows}{p}_h(x) + \Delta\overset{\rightrightarrows}{p}_h(y) + \Delta\overset{\rightrightarrows}{p}_s(x,y,z) \\ &+ \Delta\overset{\rightrightarrows}{p}_{hh}(x,y) + \Delta\overset{\rightrightarrows}{p}^{(1)}_{sh}(x,y,z) + \Delta\overset{\rightrightarrows}{p}^{(2)}_{sh}(x,y,z) + \Delta\overset{\rightrightarrows}{p}_{shh}(x,y,z) \end{aligned} \quad (7.6)$$

$$\begin{aligned} n(x,y,z) &= n_s(x,y,z) + \Delta n_h(x) + \Delta n_h(y) \\ &+ \Delta n_{hh}(x,y) + \Delta n^{(1)}_{sh}(x,y,z) + \Delta n^{(2)}_{sh}(x,y,z) + \Delta n_{shh}(x,y,z) \end{aligned} \quad (7.7)$$

Note that the correction terms Δn and $\Delta\overset{\rightrightarrows}{p}$ involving the soft wall are a function of all three coordinates x,y,z due to the periodicity of the wall. Therefore, we have to distinguish between $\Delta\overset{\rightrightarrows}{p}^{(1)}_{sh}$ referring to the edge formed by the walls at $z=0$ and $x=0$ and $\Delta\overset{\rightrightarrows}{p}^{(2)}_{sh}$ referring to the edge formed by the walls at $z=0$ and $y=0$. A similar distinction exists for $\Delta n^{(1)}_{sh}$ and $\Delta n^{(2)}_{sh}$. The correction terms vanish far away from the walls, at positions $\zeta < x,y,z < L/2$ which we denote as $\bar{r}$. Taking e.g. x and y far away from the hard walls, (7.6) gives the definition of $\Delta\overset{\rightrightarrows}{p}_s$

$$\Delta\overset{\rightrightarrows}{p}_s(\bar{x},\bar{y},z) = \overset{\rightrightarrows}{p}(\bar{x},\bar{y},z) - \overset{\rightrightarrows}{p}_B \quad (7.8)$$

The periodicity of ϕ^{ext} is reflected in $\Delta\overset{\rightrightarrows}{p}_s$: it is a periodic funtion with, in the general case $a_x \neq a_y$, a period a_x in the x and a_y in the y-direction.

Inserting the decomposition of $\overset{\rightrightarrows}{p}$ in (2.10), we obtain decomposition (7.2) of $d\Omega$ with $d\Omega_B$ given by (5.8), $d\Omega_h$ by (6.9) and

$$d\Omega_{st} = -\int_0^L dx \int_0^L dy \int_0^\infty dz \; \{ \Delta\overset{\rightrightarrows}{p}_s : \nabla\vec{u} - n\,\vec{u}\cdot\nabla\phi^{ext} \} \quad (7.9)$$

Note that we did not use the decomposition of the density but included the term $n\,\vec{u}\cdot\nabla\phi^{ext}$ completely in $d\Omega_{st}$ which differs therefore from the term (6.8) for $d\Omega_s$ in the previous section,.

The factor $\vec{u}\cdot\nabla\phi^{ext}$ in $d\Omega_{st}$ consists of three terms: besides the term involving $z\partial_z$, the structured character of the wall has introduced a term involving $(x-L)\partial_x$ and $(y-L)\partial_y$ (see (7.5)). The integral over $n\ z\ \partial_z\phi^{ext}$ is easily evaluated. This integrand is periodic far away from the hard walls. Therefore, all units of area far away from the hard walls contribute equally to the integral which is thus of the order L^2. Similarly, all units of area far away from the hard walls contribute equally to the integral over $\Delta\overset{\rightrightarrows}{p}_s : \nabla\vec{u}$ which is therefore also of the order L^2.

The integrals over $n\ (x-L)\ \partial_x \phi^{ext}$ and $n\ (y-L)\ \partial_y \phi^{ext}$ are more difficult to evaluate. These integrands are not periodic and moreover, they become of the order L near the walls at $x=0$ and $y=0$ respectively. Therefore, it seems as if the integrals are of the order L^3. This is, however, not the case: one can proof that although the integrands are not periodic, each unit of area far away from the hard walls still gives the same contribution to the integral. This follows immediately from the fact that the integrals of $n\ \partial_x \phi^{ext}$ and $n\ \partial_y \phi^{ext}$ over a unit of area in the middle of the soft wall vanish (see (C.1)). As all units of area far away from the hard walls contribute equally to the integrals over $n\ (x-L)\ \partial_x \phi^{ext}$ and $n\ (y-L)\ \partial_y \phi^{ext}$, these integrals are of the order L^2. The fact that the integrand becomes of the order L gives these integrals a remarkable feature: the deviations of the density near the walls at $x=0$ and $y=0$ contribute to the order L^2. We therefore split $d\Omega_{st}$ in two terms

$$d\Omega_{st} = -L^2 \frac{1}{a_x a_y} \int_{cell} dx\, dy \int_0^{\infty} dz\ \{\ \Delta \overset{\Rightarrow}{p}_s(\vec{r}) : \nabla \vec{u}\ -\ \lambda z\ n_s(\vec{r})\ \frac{\partial}{\partial z} \phi^{ext}(\vec{r})\ \}$$
$$+\ \lambda \int_0^L dx \int_0^L dy \int_0^{\infty} dz\ n(\vec{r})\ \{\ (x-L) \frac{\partial}{\partial x} + (y-L) \frac{\partial}{\partial y}\ \}\ \phi^{ext}(\vec{r})\ +\ O(L) \qquad (7.10)$$

where a cell stands for an area $a_x \times a_y$ far away from the hard walls. Dividing (7.10) by $2\lambda\ L^2$, we obtain from (7.1)

$$\gamma_{st}(L) = -\frac{1}{2a_x a_y} \int_{cell} dx\, dy \int_0^{\infty} dz\ \{\ \Delta p_s^{xx} + \Delta p_s^{yy} + \Delta p_s^{zz} - z\ n_s\ \frac{\partial}{\partial z} \phi^{ext}\ \}$$
$$+\ \frac{1}{2L^2} \int_0^L dx \int_0^L dy \int_0^{\infty} dz\ n\ \{\ (x-L) \frac{\partial}{\partial x} + (y-L) \frac{\partial}{\partial y}\ \}\ \phi^{ext}\ +\ O(L^{-1}) \qquad (7.11)$$

To obtain γ_{st}, $\gamma_{st}(L')$ has to be averaged over all values of L' between L and $L+a$ as indicated in (7.4). The first integral in (7.11) does not depend on the location of the hard walls but is entirely given by the properties of the fluid in the middle of the soft wall. The average (7.4) of this integral over different locations of the wall is therefore trivial. The second integral however, does depend on the location of the hard walls since the density in the edges, which contribute to the order L^0, depends on it. Some knowledge about the density in the edges is necessary to be able to perform the average. In appendix D we show, by using an expansion of the density in the activity, that average (7.4) over the second term in (7.11) vanishes. Thus we find

$$\gamma_{st} = -\frac{1}{2a_x a_y} \int_{cell} dx\, dy \int_0^{\infty} dz\ \{\ \Delta p_s^{xx} + \Delta p_s^{yy} + \Delta p_s^{zz} - z\ n_s\ \frac{\partial}{\partial z} \phi^{ext}\ \} \qquad (7.12)$$

As in the previous section, the integral over Δp_s^{zz} cancels against the integral over $z\ n_s\ \partial_z \phi^{ext}$ (see (C.2)) and the expression for γ_{st} simplifies to

$$\gamma_{st} = -\frac{1}{2a_x a_y} \int_{cell} dx\, dy \int_0^{\infty} dz\ \{\ \Delta p_s^{xx}(x,y,z) + \Delta p_s^{yy}(x,y,z)\ \} \qquad (7.13)$$

Instead of displacement field (4.1) we could have used a displacement field that shifts the wall at $x=0$ or $y=0$ only. In that case, we would have obtained

$$\gamma_{st} = -\frac{1}{a_x a_y} \int_{cell} dx\, dy \int_0^\infty dz\, \Delta p_s^{xx}(x,y,z)$$

$$= -\frac{1}{a_x a_y} \int_{cell} dx\, dy \int_0^\infty dz\, \Delta p_s^{yy}(x,y,z) \tag{7.14}$$

which shows that the integrals over a unit of area of Δp_s^{xx} and Δp_s^{yy} are equal. This expression for γ_{st} is a direct generalisation of (6.20).

8. Summary and conclusions.

We have derived microscopic expressions for the surface and line tension of solid-fluid interfaces. They were obtained from a careful analysis of the change in grand potential under a deformation of the fluid's vessel. These expressions fall into two classes: density expressions and pressure expressions. The density expressions relate thermodynamic quantities to the density at a hard wall, the pressure expressions relate them to the pressure tensor.

Density expression (1.1) for the pressure was already well known[3)] and it is shown in this paper that it is the first in a hierachy of three expressions, the second involving the surface tension, the third the line tension. Density expressions for the surface tension relate the density at a hard wall near an edge, to the surface tension of the wall which forms the edge with the hard wall. The second wall can be either a hard or a structureless soft wall, the density expression reads in both cases

$$\gamma = -k_B T \int_0^\infty dz\, \Delta n(z) \tag{8.1}$$

c.f. (4.13) and (4.23). The second wall can also be a structured, soft wall in which case $\Delta n(z)$ depends on the location of the hard wall in the elementary area which is defined by the structured wall. If e.g. the hard wall is placed in the y-z plane, the r.h.s. of (8.1) should be averaged over all locations of the hard wall within the periodic length in the x-direction to obtain the density expression for the structured, soft wall.

Density expressions for the line tension have precisely the same form as (8.1). They relate the density at a hard wall near a corner, to the line tension of the edge which stands tangential to the hard wall and terminates in the corner. The expression reads

$$\tau = -k_B T \int_0^\infty dy \int_0^\infty dz\, \Delta n(y,z) \tag{8.2}$$

c.f. (4.14) and (4.24). The validity of (8.2) has been proven in the cases that the edge is formed by two hard walls and by a hard and a soft wall. One can demonstrate that it also holds in case of an edge between two structureless, soft walls. We did not consider edges which involve a structured wall. However, we have no reason to assume that anything else but the same averaging as in the case of the surface tension has to be applied to (8.2) in that case. In general, density expressions also exist near soft walls as discussed at the end of section 4, but we did not pursue them in this paper.

The pressure equation for the surface tension is also well known[5)]. It reads

$$\gamma = -\int_0^\infty dz\ \Delta p^T(z) \tag{8.3}$$

which holds for both a hard and a structureless soft wall, see (5.16) and (6.20). The derivation of a pressure equation for the structured, soft wall is much more complicated but the result is a straightforward extension of (8.3). In the case of a structured wall, Δp^T depends also on the position along the wall and we have shown that the r.h.s. of (8.3) has to be averaged over a unit of area to obtain the pressure equation for the structured wall.

Pressure equations for the line tension have again the same form as the equation (8.3) for the surface tension. Whereas (8.3) expresses the surface tension of a wall in p^T, the component of $\overset{\rightrightarrows}{p}$ along the wall, the pressure equation for the line tension expresses this quantity in the component of $\overset{\rightrightarrows}{p}$ along the edge, i.e. p^{xx}. The expression is given by

$$\tau = -\int_0^\infty dy \int_0^\infty dz\ \Delta p^{xx}(y,z) \tag{8.4}$$

which is proven for an edge formed by two hard walls and an edge formed by a hard and a soft wall, c.f. (5.22) and (6.30). Again, one easily proves that it holds also for an edge formed by two structureless soft walls and we expect its validity, with the usual averaging procedure, for an edge which involves a structured soft wall, too. The latter assumption however, is probably hard to prove rigorously.

Surprisingly, it turns out to be possible to generalize (8.3). One can evaluate p^T at an arbitrary distance from an edge formed with a hard wall and show that the influence of the edge on p^T does not alter the integral, c.f. (5.20) and (6.24). This generalized expression reduces to the density expression (8.1) if the distance to the wall is taken to vanish since the diagonal components of the pressure tensor become equal to $k_B T$ times the density at a hard wall, c.f. (2.11). The same generalisation is possible for (8.4) where it can be shown that the influence of a corner on p^{xx} leaves the integral unaltered. Reducing the distance to the corner, formed with a hard wall, transforms the generalized expressions to the density expression (8.2).

We have seen various expressions for the surface and line tension, all related to the routes (2.10) and (2.12) to the change in grand potential. The expressions are very symmetric: they are the same for all the models of a wall we have considered and furthermore, each expression for the surface tension has its counterpart at the level of the line tension. The density expressions reveal that the density at a hard wall is related to thermodynamic quantities, a surprising fact. Probably of more practical use are the pressure equations since they are well suited to measure surface and line tensions in a simulation. Especially the pressure equation for the structured soft wall is of immediate interest in view of the many investigations of the solid-fluid surface nowadays. If, however, simulations will ever deal with edges or contact lines, the expressions for the line tension will certainly prove to be equally useful.

References

1) for a review see e.g. P.G de Gennes, Rev. Mod. Phys. **57,** 827 (1985).

2) J.H. Sikkenk, J.O. Indekeu, J.M.J. van Leeuwen, E.O. Vossnack and A.F. Bakker, J. Stat. Phys. **52,** 23 (1988).

3) F. van Swol and J.R. Henderson, Faraday Symp. Chem. Soc. **20,** 1 (1985).

4) J.S. Rowlinson and B. Widom, *Molecular Theory of Capillarity* (Clarendon, Oxford, 1982).

5) S. Ono and S. Kondo, *Encyclopedia of Physics* (ed. S. Flugge), vol 10, (Springer, Berlin, 1960).

6) J.R. Henderson and F. van Swol, J. Chem. Phys. **89,** 5010 (1988).

7) D. Schofield and J.R. Henderson, Proc. R. Soc. Lond. A **379,** 231 (1982).

8) J.H. Irving and J.G. Kirkwood, J. Chem. Phys. **18,** 817 (1950).

9) A. Harasima, Adv. Chem. Phys. **1,** 203 (1958).

10) L.E. Reichl, *A modern course in Statistical Physics* (Edward Arnold (Publishers) Ltd, 1980).

Appendix A.

We proof the following properties of a pressure tensor near the hard wall in the plane $z=0$

$$\Delta p_h^{zz}(z) = 0 \tag{A.1}$$

$$\int_0^\infty dz\ \Delta p_{hh}^{yy}(y,z) = 0 \tag{A.2}$$

$$\int_0^\infty dy \int_0^\infty dz\ \Delta p_{hhh}^{xx}(x,y,z) = 0 \tag{A.3}$$

These properties all follow from the condition that the tensor is divergenceless near hard walls, (2.2) with $\phi^{ext}=0$.

First, we proof (A.1). In terms of p^{zz} and p, Δp_h^{zz} reads

$$\Delta p_h^{zz}(z) = p^{zz}(\infty,\infty,z) - p \tag{A.4}$$

The off-diagonal components of $\overleftrightarrow{p}$ vanish near a hard wall, far away from edges and corners

$$p^{\alpha\beta}(\infty,\infty,z) = 0 \qquad \alpha \neq \beta \tag{A.5}$$

in which case condition (2.2) on the divergence of $\overleftrightarrow{p}$ reads

$$\frac{\partial}{\partial z}\ \Delta p_h^{zz}(z) = 0 \tag{A.6}$$

Since Δp_h^{zz} vanishes in the bulk fluid, at $z=\infty$, it has to vanish at any distance z as stated by (A.1).

Secondly, we proof (A.2). In terms of p^{yy}, Δp_{hh}^{yy} reads

$$\Delta p_{hh}^{yy}(y,z) = p^{yy}(\infty,y,z) - p^{yy}(\infty,\infty,z) \tag{A.7}$$

(2.2) reads in this case

$$\frac{\partial}{\partial y}\ \Delta p_{hh}^{yy}(y,z) = -\frac{\partial}{\partial z}\ p^{zy}(\infty,y,z) \tag{A.8}$$

There appears no derivative with respect to x since the tensor is translationally invariant in the x-direction in the edge formed by the walls at $y=0$ and $z=0$, far away from the plane at $x=0$. From (A.8), we find

$$-\frac{\partial}{\partial y}\int_0^\infty dz\ \Delta p_{hh}^{yy}(y,z) = p^{zy}(\infty,y,\infty) - p^{zy}(\infty,y,0) = 0 \tag{A.9}$$

The term $p^{zy}(\infty,y,\infty)$ denotes an off-diagonal component of $\overleftrightarrow{p}$ near a hard wall, far away from the edges and vanishes due to (A.5). The second term denotes an off-diagonal component at a hard wall which also vanishes, c.f. (2.11). Therefore, the derivative (A.8) vanishes. Since the integral vanishes at $y=\infty$, where the integrand vanishes, the integral has to vanish at any distance y which implies (A.2).

Finally, we proof (A.3). The derivative of Δp_{hhh}^{xx} with respect to x reads

$$\frac{\partial}{\partial x}\ \Delta p_{hhh}^{xx}(x,y,z) = \frac{\partial}{\partial x}\ \{\ p^{xx}(x,y,z) - p^{xx}(x,y,\infty) - p^{xx}(x,\infty,z)\ \} \tag{A.10}$$

With (2.2), the derivative is rewritten as

$$\frac{\partial}{\partial x}\ \Delta p_{hhh}^{xx}(x,y,z) =$$
$$-\frac{\partial}{\partial y}\ \{\ p^{yx}(x,y,z) - p^{yx}(x,y,\infty)\ \} - \frac{\partial}{\partial z}\ \{\ p^{zx}(x,y,z) - p^{zx}(x,\infty,z)\ \} \tag{A.11}$$

This yields for the derivative of the integral (A.3)

$$-\frac{\partial}{\partial x}\int_0^\infty dy \int_0^\infty dz\ \Delta p_{hhh}^{xx}(x,y,z) = \int_0^\infty dz\ [\ p^{yx}(x,y,z) - p^{yx}(x,y,\infty)\ ]_{y=0}^{\infty}$$
$$+ \int_0^\infty dy\ [\ p^{zx}(x,y,z) - p^{zx}(x,\infty,z)\ ]_{z=0}^{\infty} \tag{A.12}$$

The off-diagonal components vanish at and near a hard wall due to (2.11) and (A.5) respectively. The only remaining terms are the terms in the edges

$$-\frac{\partial}{\partial x}\int_0^\infty dy \int_0^\infty dz\ \Delta p_{hhh}^{xx}(x,y,z) = \int_0^\infty dz\ p^{yx}(x,\infty,z) + \int_0^\infty dy\ p^{zx}(x,y,\infty) \tag{A.13}$$

The arguments, based on the microscopic definition of $\overset{\rightrightarrows}{p}$, (2.1), and the symmetry in the pair correlation function, that lead to (A.5) also show that these terms vanish. Thus, the derivative (A.13) vanishes and since the integral vanishes at $x=\infty$, the integral vanishes at any distance x, yielding (A.3).

Appendix B.

We proof the following properties of the tensor near the structureless soft wall in the plane $z=0$

$$\int_0^\infty dz\ \{\ \Delta p_s^{zz}(z) - z\ n_s(z)\ \frac{\partial}{\partial z}\ \phi^{ext}(z)\ \} = 0 \tag{B.1}$$

$$\int_0^\infty dy \int_0^\infty dz\ \{\ \Delta p_{sh}^{zz}(y,z) - (\ \Delta n_h(y) + \Delta n_{sh}(y,z)\ )\ z\ \frac{\partial}{\partial z}\ \phi^{ext}(z)\ \} = 0 \tag{B.2}$$

$$\int_0^\infty \mathrm{d}z \; \Delta p_{sh}^{yy}(y,z) \;=\; 0 \tag{B.3}$$

$$\int_0^\infty \mathrm{d}y \int_0^\infty \mathrm{d}z \; \Delta p_{shh}^{xx}(x,y,z) \;=\; 0 \tag{B.4}$$

First, we proof (B.1). The correction term Δp_s^{zz} is defined as in (A.4) with the hard wall in the plane $z=0$ replaced by a soft wall. Identity (A.5) still holds. Condition (2.2) reads now

$$\frac{\partial}{\partial z} \; \Delta p_s^{zz}(z) \;=\; -n_s(z) \; \frac{\partial}{\partial z} \; \phi^{ext}(z) \tag{B.5}$$

Insert this identity in the integral (B.1), called I_1, and one obtains

$$I_1 \;=\; \int_0^\infty \mathrm{d}z \; \frac{\partial}{\partial z} \; \{ \; z \; \Delta p_s^{zz}(z) \; \} \tag{B.6}$$

since $\Delta p_s^{zz}(z)$ vanishes at large distances z, I_1 vanishes as stated by (B.1).

Secondly, we proof (B.2). The integrands that appear in the integral read in terms of p^{zz}, p and n

$$\Delta p_{sh}^{zz}(y,z) \;=\;$$

$$\{ \; p^{zz}(\infty,y,z) \; - \; p \; \} \; - \; \{ \; p^{zz}(\infty,y,\infty) \; - \; p \; \} \; - \; \{ \; p^{zz}(\infty,\infty,z) \; - \; p \; \} \tag{B.7}$$

$$\Delta n_h(y) \; + \; \Delta n_{sh}(y,z) \;=\; n(\infty,y,z) \; - \; n(\infty,\infty,z) \tag{B.8}$$

so the integral, called I_2, reads in terms of p^{zz}, p and n

$$\begin{aligned} I_2 \;=\; & \int_0^\infty \mathrm{d}y \int_0^\infty \mathrm{d}z \; \{ \; p^{zz}(\infty,y,z) \; - \; p^{zz}(\infty,y,\infty) \; - \; z \; n(\infty,y,z) \; \frac{\partial}{\partial z} \; \phi^{ext}(z) \; \} \\ & - \int_0^\infty \mathrm{d}y \; \mathrm{d}z \; \{ \; p^{zz}(\infty,\infty,z) \; - \; p \; - \; z \; n(\infty,\infty,z) \; \frac{\partial}{\partial z} \; \phi^{ext}(z) \; \} \end{aligned} \tag{B.9}$$

The last integral vanishes due to (B.1). Condition (2.2) on the divergence of the pressure tensor reads in this case

$$\begin{aligned} \frac{\partial}{\partial y} \; p^{yz}(\infty,y,z) \; + \; \frac{\partial}{\partial z} \; \{ \; p^{zz}(\infty,y,z) \; - \; p^{zz}(\infty,y,\infty) \; \} \;=\; & \\ -n(\infty,y,z) \; \frac{\partial}{\partial z} \; \phi^{ext}(z) & \end{aligned} \tag{B.10}$$

Substitution of these identitities in the first integral of (B.9) gives

$$I_2 \;=\; \int_0^\infty \mathrm{d}y \int_0^\infty \mathrm{d}z \; \frac{\partial}{\partial z} \; \{ \; z \; (p^{zz}(\infty,y,z) \; - \; p^{zz}(\infty,y,\infty)) \; \}$$

$$+ \int_0^\infty dy \int_0^\infty dz\ z \frac{\partial}{\partial y} p^{yz}(\infty,y,z) \tag{B.11}$$

Integration with respect to z shows that the first integral of the r.h.s. vanish. The integration with respect to y in the second integral gives

$$I_2 = \int_0^\infty dz\ z\ \{\ p^{yz}(\infty,\infty,z) - p^{yz}(\infty,0,z)\ \} \tag{B.12}$$

The first term of the integrand denotes an off-diagonal component of $\vec{\vec{p}}$ near a soft wall which vanishes. The second term denotes an off-diagonal component at a hard wall which also vanishes, c.f. (2.11). Therefore, I_2 vanishes.

The proofs of (B.3) and (B.4) are the same as the proofs of (A.2) and (A.3). One should merely keep in mind that the hard wall in the plane $z=0$ has been replaced by a soft, structureless one for which (6.3) holds.

Appendix C.

We proof the following properties of the density and pressure tensor near the structured, soft wall in the plane $z=0$

$$\int_{cell} dx\ dy \int_0^\infty dz\ n_s(\vec{r}) \frac{\partial}{\partial x} \phi^{ext}(\vec{r}) = 0 \tag{C.1}$$

$$\int_{cell} dx\ dy \int_0^\infty dz\ \{\ \Delta p_s^{zz}(\vec{r}) - z\ n_s(\vec{r}) \frac{\partial}{\partial z} \phi^{ext}(\vec{r})\ \} = 0 \tag{C.2}$$

where a cell denotes a unit of area far away from the hard walls. Both identities follow from condition (2.2) on the divergence of $\vec{\vec{p}}$.

First, we proof (C.1). Condition (2.2) reads

$$\frac{\partial}{\partial x} p^{xx} + \frac{\partial}{\partial y} p^{yx} + \frac{\partial}{\partial z} p^{zx} = -n_s \frac{\partial}{\partial x} \phi^{ext} \tag{C.3}$$

since n equals n_s far awy from the hard walls. Substituting the l.h.s. in the integral in (C.1), denoted by I_1, one obtains

$$-I_1 = \int_{a_y} dy \int_0^\infty dz\ [\ p^{xx}\ ]_{x=x_0}^{x_0+a_x} + \int_{a_x} dx \int_0^\infty dz\ [\ p^{yx}\ ]_{y=y_0}^{y_0+a_y}$$
$$+ \int_{cell} dx\ dy\ [\ p^{zx}\ ]_{z=0}^{\infty} \tag{C.4}$$

where x_0 and y_0 denote the lower boundaries of the cell. The periodicity of the tensor makes the first two terms vanish. The fact that the tensor vanishes completely at $z=0$ and that its off-diagonal components vanish in the bulk fluid shows that the third term also vanishes, which proves (C.1).

The proof of (C.2) goes similarly. Condition (2.2) reads

$$\frac{\partial}{\partial x} p^{xz} + \frac{\partial}{\partial y} p^{yz} + \frac{\partial}{\partial z} \Delta p^{zz} = -n_s \frac{\partial}{\partial z} \phi^{ext} \tag{C.5}$$

Integrating (C.5) over a unit of area and using the periodicity of $\vec{\vec{p}}$, we obtain

$$\int_{cell} dx\, dy \int_0^\infty dz \frac{\partial}{\partial z} \Delta p^{zz} = -\int_{cell} dx\, dy \int_0^\infty dz\, n_s \frac{\partial}{\partial z} \phi^{ext} \tag{C.6}$$

and thus the integral in (C.2), denoted as I_2, can be written as

$$I_2 = \int_{cell} dx\, dy \int_0^\infty dz \frac{\partial}{\partial z} \{ z\, \Delta p^{zz} \} \tag{C.7}$$

Since Δp^{zz} vanishes in the bulk fluid at $z = \infty$, I_2 vanishes.

Appendix D.

We proof that average (7.4) of the integrals

$$d\Omega_x \equiv \lambda \int_0^L dx \int_0^L dy \int_0^\infty dz\, n(\vec{r})\, (x-L) \frac{\partial}{\partial x} \phi^{ext}(\vec{r}) \tag{D.1}$$

and

$$d\Omega_y \equiv \lambda \int_0^L dx \int_0^L dy \int_0^\infty dz\, n(\vec{r})\, (y-L) \frac{\partial}{\partial y} \phi^{ext}(\vec{r}) \tag{D.2}$$

vanish. It will be proven explicitly for $d\Omega_x$ whereupon it follows for $d\Omega_y$ by symmetry.

At first, we find it more convenient to shift the origin $x,y=0$ to $x,y=L$. Denoting the new coordinates as $\vec{r}'$, $d\Omega_x$ becomes

$$d\Omega_x \equiv \int_0^L dx' \int_0^L dy' \int_0^\infty dz'\, n(\vec{r}')\, x' \frac{\partial}{\partial x'} \phi^{ext}(\vec{r}') \tag{D.3}$$

To be strict, we should have replaced n by n' with $n'(\vec{r}') = n(\vec{r})$ (and similarly for ϕ^{ext}) but since the properties of n' and n are essentially the same, we drop the prime. The density at a position $\vec{r}$ is evaluated in an expansion in the activity z, defined in (2.6) (the activity z should not be confused with the position z).

$$n(\vec{r}_1) = \sum_{N=1}^{\infty} c_N(\vec{r}_1)\, z^N \tag{D.4}$$

where the coefficients are of the form[10)]

$$c_N(\vec{r}_1) = \int_V d\vec{r}_2,...,d\vec{r}_N \; \{ \; F_N^e(\vec{r}_1,...,\vec{r}_N) \; + \; 1 \; \} \; F_N(\vec{r}_1,...,\vec{r}_N) \tag{D.5}$$

with

$$F_N^e(\vec{r}_1,...,\vec{r}_N) = e^{-\beta\{\phi^{\mathrm{ew}}(\vec{r}_1) + ... + \phi^{\mathrm{ew}}(\vec{r}_N)\}} - 1 \tag{D.6}$$

and $F_N(\vec{r}_1, \ldots, \vec{r}_N)$ a function which depends only on the relative distances r_{ij} and is short ranged, i.e. vanishes when one of the r_{ij} becomes large, except for $N = 1$. Furthermore, F_N is symmetric under permutations of its arguments. For $N = 1,2,3$ we have

$$F_1 = 1 \tag{D.7}$$

$$F_2(\vec{r}_1,\vec{r}_2) = f(r_{12}) \tag{D.8}$$

$$F_3(\vec{r}_1,\vec{r}_2,\vec{r}_3) = \frac{1}{2} \; \{ \; f(r_{12}) \; f(r_{13}) \; f(r_{23}) \; + \; f(r_{12}) \; f(r_{13}) \; + \; f(r_{12}) \; f(r_{23}) \; + \; f(r_{13}) \; f(r_{23}) \; \} \tag{D.9}$$

where $f(r_{ij})$ denotes the Mayer f-function

$$f(r_{ij}) = e^{-\beta\phi(r_{ij})} - 1 \tag{D.10}$$

and ϕ stands for the interparticle potential. Inserting expansion (D.5) in $d\Omega_x$ results in the expansion

$$d\Omega_x = \sum_{N=1}^{\infty} d\Omega_N \; z^N \tag{D.11}$$

with, dropping the prime of the arguments,

$$d\Omega_N = \lambda \int_0^L dx_1 \; dy_1 \int_0^{\infty} dz_1 \int_V d\vec{r}_2,...,d\vec{r}_N \; F_N(\vec{r}_1,...,\vec{r}_N) \; x_1 \; \frac{\partial}{\partial x_1} \; F_N^e(\vec{r}_1,...,\vec{r}_N) \tag{D.12}$$

Due to the short ranged character of F_N and the fact that F_N^e vanishes if all the z_i are large, the integration over the z-coordinates can as well be taken from 0 to ∞

$$d\Omega_N = \lambda \int_0^L dx_1,...,dy_N \int_0^{\infty} dz_1,...,dz_N \; F_N(\vec{r}_1,...,\vec{r}_N) \; x_1 \; \frac{\partial}{\partial x_1} \; F_N^e(\vec{r}_1,...,\vec{r}_N) \tag{D.13}$$

The average (7.4) reads

$$\Delta\Omega_x \equiv \frac{1}{2aL} \int_L^{L+a} dL' \; \left| \frac{d\Omega_x}{dL'} \right| \tag{D.14}$$

Expansion (D.11) gives

$$\Delta\Omega_x = \sum_{N=1}^{\infty} \Delta\Omega_N \, z^N \tag{D.15}$$

with

$$\Delta\Omega_N = \frac{1}{2aL} \int_{L}^{L+a} \mathrm{d}L' \left[\frac{\mathrm{d}\Omega_N}{\mathrm{d}L'} \right] \tag{D.16}$$

We will show that all terms $\Delta\Omega_N$ vanish.

To do so, we have to calculate the derivative $\mathrm{d}\Omega_N/\mathrm{d}L$ and integrate it over the increase of L. The derivative is simply calculated by dividing $\mathrm{d}\Omega_N$ by $\mathrm{d}L$ with $\mathrm{d}L = \lambda L$. The integration is most easily performed if the dependence of the derivative on L can be brought from the integration boundary to the integrand. The first step to do this is partial integration

$$\frac{\mathrm{d}\Omega_N}{\mathrm{d}L} = \int_0^L \mathrm{d}y_1 \int_0^L \mathrm{d}x_2,\ldots,\mathrm{d}y_N \int_0^{\infty} \mathrm{d}z_1,\ldots,\mathrm{d}z_N \, [\, F_N \, F_N^e \,]_{x_1=L}$$

$$- \frac{1}{L} \int_0^L \mathrm{d}x_1,\ldots,\mathrm{d}y_N \int_0^{\infty} \mathrm{d}z_1,\ldots,\mathrm{d}z_N \, F_N^e \left\{ F_N + x_1 \frac{\partial}{\partial x_1} F_N \right\}$$

$$\equiv I_1 + I_2 \tag{D.17}$$

The presence of L in the integration boundaries of I_1 can be removed. If one changes the integration variables x_i to x_{1i} ($i=2,\ldots,N$, $x_{1i}=x_1-x_i$), the x_{1i} can be taken to range from 0 to ∞ because of the short ranged character of F_N. The same substitution can be made for the y_i with y_{1i} ranging from $-\infty$ to ∞. This range neglects the presence of the corner: at positions $x_1=L$ and $y_1,z_1 \geq 0$, the y_i should be restricted to $y_i>0$. This restriction however, only adds a correction of the order L^0 to the integral which itself is of the order L. We obtain

$$I_1 = \int_0^L \mathrm{d}y_1 \int_0^{\infty} \mathrm{d}x_{12},\ldots,\mathrm{d}x_{1N} \int_{-\infty}^{\infty} \mathrm{d}y_{12},\ldots,\mathrm{d}y_{1N} \int_0^{\infty} \mathrm{d}z_1,\ldots,\mathrm{d}z_N \, [\, F_N \, F_N^e \,]_{x_1=L}$$

$$+ O(L^0) \tag{D.18}$$

Finally, we use the periodicity of F_N^e to remove the presence of L in the integration boundary of y_1

$$I_1 = \frac{L}{a_y} \int_{a_y} \mathrm{d}y_1 \int_0^{\infty} \mathrm{d}x_{12},\ldots,\mathrm{d}x_{1N} \int_{-\infty}^{\infty} \mathrm{d}y_{12},\ldots,\mathrm{d}y_{1N} \int_0^{\infty} \mathrm{d}z_1,\ldots,\mathrm{d}z_N \, [\, F_N \, F_N^e \,]_{x_1=L}$$

$$+ O(L^0) \tag{D.19}$$

One would also like to remove the presence of L from the integration boundaries of I_2. If it were not for the factor x_1, the integrand of I_2 would be periodic in x_1 and y_1 and the presence of L could be removed by restricting the integral over x_1 and y_1 to one unit of area and changing the integration variables x_i and y_i to x_{1i} and y_{1i}. The restriction on the integration over x_1 and y_1 would be compensated for by multiplying the integral with a factor $L^2/(a_x a_y)$. The integration over the x_{1i} and y_{1i} would range from $-\infty$ to ∞. This range neglects the presence of edges but they only give a correction of order L^0.

The periodicity of the integrand in x_1 is restored if the absolute coordinate x_1 can be replaced by a relative coordinate such as x_{1i}. We show that such a substitution, namely

$$x_1 \frac{\partial}{\partial x_1} F_N \rightarrow \frac{1}{N} \sum_{i=2}^{N} x_{1i} \frac{\partial}{\partial x_1} F_N \tag{D.20}$$

can indeed be made.

Under integral I_2, the term $x_1 \partial_{x_1} F_N$ can be replaced by

$$x_1 \frac{\partial}{\partial x_1} F_N \rightarrow \frac{1}{N} \sum_{i=1}^{N} x_i \frac{\partial}{\partial x_i} F_N \tag{D.21}$$

If F_N is taken to be a function of the relative coordinates $\vec{r}_{ij}$, the r.h.s. of (D.21) can be written as

$$\begin{aligned} \sum_{i=1}^{N} x_i \frac{\partial}{\partial x_i} F_N &= \sum_{i=1}^{N} x_i \sum_{j=1}^{N} \frac{\partial}{\partial x_{ij}} F_N \\ &= \sum_{i=1}^{N} \sum_{j=i+1}^{N} x_{ij} \frac{\partial}{\partial x_{ij}} F_N \end{aligned} \tag{D.22}$$

the r.h.s. of (D.20) is equal to

$$\sum_{i=2}^{N} x_{1i} \frac{\partial}{\partial x_1} F_N = \sum_{i=2}^{N} x_{1i} \sum_{j=2}^{N} \frac{\partial}{\partial x_{1j}} F_N \tag{D.23}$$

The difference between the r.h.s. of (D.22) and (D.23) equals

$$S \equiv \sum_{i=1}^{N} \sum_{j=i+1}^{N} x_{ij} \frac{\partial}{\partial x_{ij}} F_N - \sum_{i=2}^{N} x_{1i} \sum_{j=2}^{N} \frac{\partial}{\partial x_{1j}} F_N \tag{D.24}$$

$$= \sum_{i=2}^{N} \sum_{j=i+1}^{N} x_{ij} \frac{\partial}{\partial x_{ij}} F_N - \sum_{i=2}^{N} \sum_{\substack{j=2 \\ j\neq i}}^{N} x_{1i} \frac{\partial}{\partial x_{1j}} F_N \tag{D.25}$$

$$= \sum_{i=2}^{N} \sum_{j=i+1}^{N} x_{ij} \frac{\partial}{\partial x_{ij}} F_N - \sum_{i=2}^{N} \sum_{j=i+1}^{N} \left(x_{1i} \frac{\partial}{\partial x_{1j}} + x_{1j} \frac{\partial}{\partial x_{1i}} \right) F_N \tag{D.26}$$

Under the integral, the integration variables x_1 and x_i in the second term and x_1 and x_j in the third term can be interchanged

$$\left(x_{1i} \frac{\partial}{\partial x_{1j}} + x_{1j} \frac{\partial}{\partial x_{1i}} \right) F_N \rightarrow \left(x_{i1} \frac{\partial}{\partial x_{ij}} + x_{j1} \frac{\partial}{\partial x_{ji}} \right) F_N \tag{D.27}$$

$$= x_{ij} \frac{\partial}{\partial x_{ij}} F_N \tag{D.28}$$

Therefore we find that over S vanishes under the integral.

$$S = 0 \tag{D.29}$$

This proves that the r.h.s. of (D.20) and (D.21) are the same under integral I_2. Because (D.21) is an allowed substitution, (D.20) must be so. With this substitution, the integrand of I_2 becomes periodic in x_1 and I_2 can be written as

$$I_2 = \frac{L}{a_x a_y} \int_{cell} dx_1 \; dy_1 \int_{-\infty}^{\infty} dx_{12},\ldots,dy_{1N} \int_{0}^{\infty} dz_1,\ldots,dz_N \; F_N^e \; \{ \; F_N + \frac{1}{N} \sum_{i=2}^{N} x_{1i} \frac{\partial}{\partial x_1} F_N \; \} + O(L^0) \tag{D.30}$$

Note that apart from the prefactor L, I_2 is independent of L.

We have now brought the derivative $d\Omega_N/dL$ in such a form that we can perform the integration (D.16). The derivative is the sum of I_1 and I_2, c.f. (D.17). The integral over I_1 reads

$$\Delta I_1 \equiv \frac{1}{2aL} \int_{L}^{L+a} dL' \; I_1(L') \tag{D.31}$$

$$= -\frac{1}{2a_x a_y} \int_{L}^{L+a_x} dx_1 \int_{a_y} dy_1 \int_{0}^{\infty} dx_{12},\ldots,dx_{1N} \int_{-\infty}^{\infty} dy_{12},\ldots,dy_{1N} \int_{0}^{\infty} dz_1,\ldots,dz_N \; F_N \, F_N^e + O(L^{-1}) \tag{D.32}$$

Characteristic of the integral is that all x-positions x_i, $i=2,\ldots,N$ should be below x_1. This restriction is easily removed

$$\Delta I_1 = -\frac{1}{N} \frac{1}{2a_x a_y} \int_{cell} dx_1 \; dy_1 \int_{-\infty}^{\infty} dx_{12},\ldots,dy_{1N} \int_{0}^{\infty} dz_1,\ldots,dz_N \; F_N \, F_N^e + O(L^{-1}) \tag{D.33}$$

the factor $1/N$ compensates for the fact that each particle in the integral (D.33) can have the largest x-coordinate whereas this is always particle 1 in (D.32). Adding ΔI_1 and the similarly defined ΔI_2, $\Delta I_2 = I_2/2$, we obtain

$$\Delta\Omega_N = \frac{1}{2a_x a_y} \int_{cell} dx_1 \; dy_1 \int_{0}^{\infty} dx_{12},\ldots,dy_{1N} \int_{0}^{\infty} dz_1,\ldots,dz_N \; F_N^e \; \{ \; \frac{N-1}{N} F_N + \frac{1}{N} \sum_{i=2}^{N} x_{1i} \frac{\partial}{\partial x_1} F_N \; \} + O(L^{-1}) \tag{D.34}$$

The term of order L^{-1} vanishes in the thermodynamic limit. All the terms in the sum will give the same contribution to the integral. We can take the term with x_{12} as exemplary and write the integral as

$$\Delta\Omega_N = \frac{1}{2a_x a_y} \frac{N-1}{N} \int_{cell} dx_1\, dy_1 \int_{-\infty}^{\infty} dx_{12},\ldots,dy_{1N} \int_0^{\infty} dz_1,\ldots,dz_N\, F_N^e \frac{\partial}{\partial x_1} \{x_{12}\, F_N\} \tag{D.35}$$

One has to apply one more partial integration with respect to x_1 to see that this contribution vanishes

$$\begin{aligned}\Delta\Omega_N = {} & \frac{1}{2a_x a_y} \frac{N-1}{N} \int_{a_y} dy_1 \int_{-\infty}^{\infty} dx_{12},\ldots,dy_{1N} \int_0^{\infty} dz_1,\ldots,dz_N\, x_{12}\, F_N\, [\, F_N^e\,]_{x_1=x_0}^{x_0+a_x} \\ & - \frac{1}{2a_x a_y} \frac{N-1}{N} \int_{cell} dx_1\, dy_1 \int_{-\infty}^{\infty} dx_{12},\ldots,dy_{1N} \int_0^{\infty} dz_1,\ldots,dz_N\, x_{12}\, F_N \frac{\partial}{\partial x_1} F_N^e\end{aligned} \tag{D.36}$$

where x_0 denotes the lower boundary of the unit cell. The first integral vanishes because of the periodicity of F_N^e. Changing the order of integration in the second integral gives

$$\Delta\Omega_N = -\frac{1}{2a_x a_y} \frac{N-1}{N} \int_{-\infty}^{\infty} dx_{12},\ldots,dy_{1N} \int_0^{\infty} dz_1,\ldots,dz_N\, x_{12}\, F_N \int_{cell} dx_1\, dy_1 \frac{\partial}{\partial x_1} F_N^e \tag{D.37}$$

which shows that the periodicity of F_N^e also makes this integral vanish. Therefore, we have obtained the desired result

$$\Delta\Omega_N = 0 \tag{D.38}$$

CHAPTER III

A visual measurement of contact angles

ABSTRACT

We have simulated a liquid-vapor interface which is confined by two parallel walls. Initially, a liquid slab is positioned perpendicular to the walls. The liquid-vapor interface deforms to a cylindrical surface which makes a definite contact angle with the walls. The angle could be varied between 0 and π by changing the solid-fluid interaction strength, showing the presence of both a wetting and a drying transition. The angle is related to the strengths of the wall-liquid, wall-vapor and liquid-vapor surface tensions via Young's law. A previous simulation positioned the liquid parallel to the walls and measured the surface tensions. Compared with the contact angles deduced from those measurements, the visually measured angles in this experiment give a different location of the drying transition.

1. Introduction

A capillary partially filled with liquid, provides a typical example of a system in which three phases are in contact. The contact takes place along the line where the meniscus, formed by the liquid-vapor interface, ends at the surface of the capillary. The three coexisting phases are the liquid, the vapor above the liquid and the solid of which the capillary consists. The meniscus meets the solid surface under a well-defined angle, the contact angle. The law of Young holds in this special case of three-phase contact where two of the phases are fluid-like and the third is rigid with a plane interface$^{1)}$. It relates the contact angle to the relative magnitudes of the three surface tensions involved:

$$\gamma_{sv} = \gamma_{sl} + \gamma_{lv} \cos\theta \tag{1.1}$$

with γ_{sv} the solid-vapor, γ_{sl} the solid-liquid and γ_{lv} the liquid-vapor surface tension; θ denotes the contact angle. The angle is measured between the solid-liquid and the liquid-vapor interface.

Young's law is most easily understood as a condition for mechanical equilibrium. Its validity has been checked by Saville in a molecular dynamics simulation$^{2)}$. That simulation treated the wall as an external potential with a variable solid-fluid interaction strength. Saville measured γ_{sv} and γ_{sl} as a function of the interaction strength. Variation of it does not affect γ_{lv} which is a property of the free liquid-vapor interface. Young's law enabled Saville to calculate θ from the surface tensions. He also measured the contact angle directly. For this purpose, Saville enclosed the liquid and its coexisting vapor between two parallel walls. The meniscus is defined as a surface of constant density which value is between the densities of the vapor and liquid phase. Inspection of the meniscus enabled Saville to measure the contact angle directly. The simulation however, gave no satisfactory agreement between the two ways to measure θ.

The contact angle is a well suited parameter to describe the "wetting" behavior of two coexisting fluids in contact with a wall$^{3)}$. The wall is said to be "completely wet" if θ equals 0 and "completely dry" if θ equals π. If the wall is completely wet the solid-vapor interface is unstable and a liquid layer will intrude between the solid and the vapor. The surface tension of a solid-vapor interface equals the surface tension of a solid-liquid plus a liquid-vapor interface:

$$\gamma_{sv} = \gamma_{sl} + \gamma_{lv} \tag{1.2}$$

Similarly will the vapor phase intrude between the solid and liquid phase if the solid is completely dry:

$$\gamma_{sl} = \gamma_{sv} + \gamma_{lv} \tag{1.3}$$

The system is called "partially wet" if θ is between 0 and $\pi/2$ and "partially dry" in the complementary case. By varying e.g. the temperature or the solid-fluid interaction, as is possible in a molecular-dynamics simulation, one can achieve a transition from a partial to a complete wet or dry state. These are genuine phase transitions, known as the "wetting" and "drying" transition respectively.

Sikkenk *et al*[3]) also investigated the wetting of a wall by a fluid at liquid-vapor coexistence in a molecular-dynamics simulation. Unlike the previous simulation, the wall consists of particles that oscillate around their lattice position. The wall resembles a thermodynamic phase instead of an external potential. The authors measured γ_{sl} and γ_{sv} as a function of the strength of the solid-fluid interaction. They calculated cos θ from the surface tensions for different interaction strengths. Cos θ was found to grow from -1 to 1 as the attraction between wall and fluid particles grew stronger. A wetting and a drying transition have been determined rather accurately, both of first order. The position of the drying transition however, is at variance with the observed behavior of the density profile. One observed that, for a range of solid-fluid attractions at which the wall was dry according to the cos θ data, a liquid layer spontaneously intruded at a solid-vapor interface. The reverse process occurred at lower attractions: a vapor layer settled itself between the wall and the liquid. The behavior of the density profiles suggested a drying transition at a lower value of the solid-fluid attraction than the contact angle data. The authors remarked that it is difficult to measure γ_{sl} and γ_{sv} reliably if the wall is built from strongly coupled particles. This difficulty might be a source of error in their calculation of cos θ.

The purpose of the simulations we present is to check the contact angles calculated in the latter work against a direct measurement of them. Saville's method is used to perform this direct measurement. The conditions, e.g. temperature, interaction potentials and type of the wall, under which the angles are measured are the same as in Sikkenk's experiment to make a comparison possible. These conditions are discussed in the next section. Section 3 contains a calculation of the expected form of the liquid-vapor interface. The same section describes how the knowledge of this form is exploited to obtain the contact angles from the simulations. The results are discussed and related to those of Saville and Sikkenk *et al* in the last section.

2. Description of the system

Our simulations mimick a system in which three phases are present: a liquid, a vapor and a solid phase. Two types of particles are needed to form this system. One type is used to build the solid wall, the other forms the fluid. A particle of type A interacts with a particle of type B via the Lennard-Jones potential ϕ_{AB} where A and B must be replaced by either s for a solid or f for a fluid particle. It reads

$$\phi_{AB}(r) = 4\,\varepsilon_{AB}\{(\sigma_{AB}/r)^{12} - (\sigma_{AB}/r)^{6}\} \tag{2.1}$$

where r is the distance between the particles, ε_{AB} sets the energy scale and σ_{AB} the length scale of the potential. The potentials are cut off at $2.5\sigma_{AB}$. This cut-off is necessary to keep the computation time within reasonable limits. The particles are enclosed in a three dimensional, cubic computational box. The box has a linear size $L = 29.1\,\sigma_{ff}$ and periodic boundary conditions in all the three directions.

The solid substrate consists of three layers of a close-packed FCC lattice. The formation of the three layers requires 2904 solid particles. The layers belong to the (100) planes of the solid, they are placed in the $x-y$ plane of the computational box. Due to the periodic boundary conditions, the fluid is enclosed in the z-direction between the first and the third layer. The solid particles are strongly coupled, $\varepsilon_{ss} = 50\ \varepsilon_{ff}$, and more massive than their fluid counterparts, $m_s = 3\ m_f$, which ensures a rigid substrate wall. The lattice spacing, determined by $\sigma_{ss} = 0.847\sigma_{ff}$ results in a mismatch between solid and fluid. This mismatch prevents solidification of the first adsorbed fluid layers.

The interaction between solid and fluid is characterized by $\sigma_{sf} = 0.921\sigma_{ff}$ which is close to the mean of σ_{ss} and σ_{ff}. The interaction strength ϵ_{sf} is varied during the simulations. The contact angle is determined as a function of the ratio $\epsilon_r = \epsilon_{sf}/\epsilon_{ff}$. The temperature of the system, the size of the box and the number of solid and fluid particles are kept fixed. The box is filled with a number of 8064 fluid particles. This amount of particles guarantees the presence of both a liquid and a vapor phase. The temperature of the system $T^* = k_B T/\epsilon_{ff} = 0.9$ is between the triple point temperature $T_t^* \approx 0.7$ and the critical temperature $T_c^* \approx 1.26$.

The simulations we performed are of the molecular dynamics type. It was possible to follow such a rather large system for long times because of the availability of a special purpose computer: the Delft Molecular Dynamics Processor (DMDP)[4]. The system described above is apart from a somewhat different amount of fluid particles, the same as in ref. 3. But instead of parallel, we place the liquid slab perpendicular to the substrate. The slab is positioned in the $x-z$ plane. It is bounded in the z-direction by two solid-fluid interfaces where it meets the substrate. The layer is translationally invariant in the x-direction due to the periodic boundaries. Figures 1 to 5 show this situation. They indicate where the reduced density $n^*(\vec{r}) = n(\vec{r})\,\sigma_{ff}^3$ averaged over the x-direction is equal to either 0.2 or 0.4. The densities of the bulk vapor phase and the bulk liquid phase at this temperature are $n_v^* = 0.046$ and $n_l^* = 0.66$ respectively[3], if the liquid-vapor interface that separates them is planar. The liquid layer resides around the plane $y^* = y/\sigma_{ff} = 0$. The upper and lower parts of the figures contain the vapor phase. The form of the liquid-vapor interface is seen to change with varying ϵ_r. The figures were obtained by averaging over 2000 configurations, each configuration taken 10 timesteps after the previous one. The reduced timestep $\Delta t^* = \Delta t\sqrt{\epsilon_{ff}}/(\sigma_{ff}\sqrt{m_f})$ was chosen to be 0.01. To obtain a system with a new value of ϵ_r, we took a previous particle configuration and adjusted ϵ_{sf} in the molecular dynamics scheme. We did not measure the density profile of this newly formed system before an equilibration period of approximately 20,000 timesteps had passed. No systematic evolution of the profile was observed afterwards.

3. Calculation of the contact angles

We want to extract a contact angle from the density profiles. Knowledge about the shape of the liquid-vapor interface will facilitate the determination of the angle. The shape results from a minimization of the free energy of the system. The minimization is performed under the assumption that the interface has a negligible width. This implies that its position is a measurable physical quantity. It is the position as it would be seen in a macroscopic observation. The geometry only allows surfaces that are translationally invariant in the x-direction and display an inversion symmetry in the x-axis. We can therefore restrict our attention to y-positions larger than zero.

The minimization of the free energy is performed in two steps. The first step determines the optimal shape of the interface at a fixed height of the contact line. The height is varied in the second step. The variation we consider first is therefore a fluctuation of the liquid-vapor surface that does not shift the contact line. The change of free energy under this variation is equal to

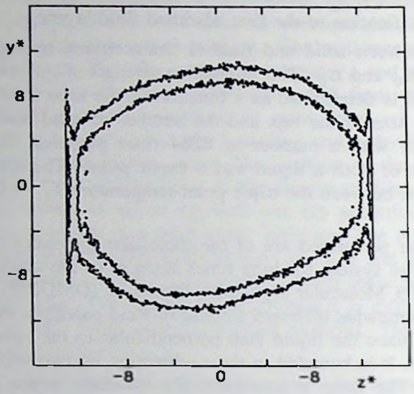

Fig. 1. Interfacial shape for a liquid slab perpendicular to the wall at $\varepsilon_r = 0.3$. The outer curve is the line of density $n^* = 0.2$. The inner curve is at $n^* = 0.4$.

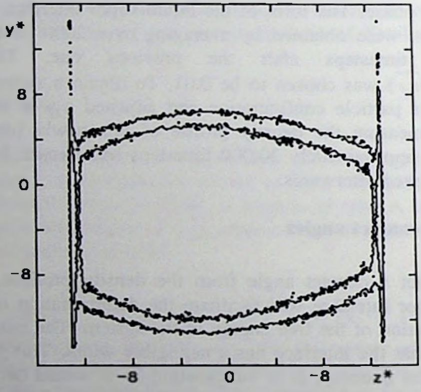

Fig. 2. As fig. 1 but at $\varepsilon_r = 0.4$.

$$\delta F = -\Delta p \, \delta V_l + \gamma_{lv} \, \delta A_{lv} \tag{3.1}$$

where F is the free energy, Δp stands short for $p_l - p_v$ and p denotes the pressure, V_l is the volume occupied by the liquid and A_{lv} is the area of the liquid-vapor surface. All extensive quantities are taken per unit of length in the x-direction. Only the upper half of the

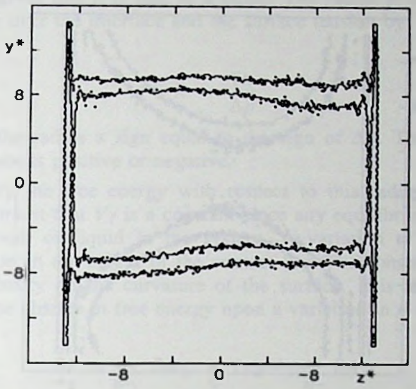

Fig. 3. As fig. 1 but at $\varepsilon_r = 0.5$.

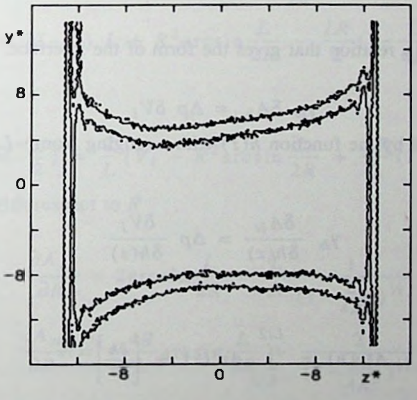

Fig. 4. As fig. 1 but at $\varepsilon_r = 0.6$.

system, $y > 0$, contributes to them. The first term on the right hand side of (3.1) is typical for a curved surface$^{1)}$. The pressure difference over the interface gives the interface its mechanical stability. The free energy must be stationary in its minimum:

$$\delta F = 0 \tag{3.2}$$

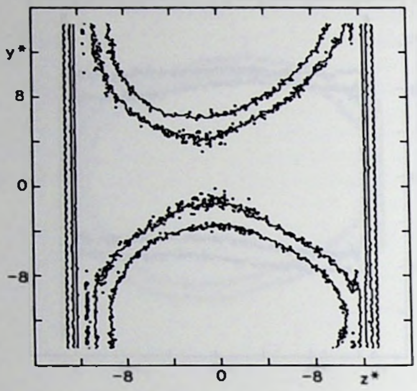

Fig. 5. As fig. 1 but at ε_r = 0.7. This profile is unstable: continuing the simulation, the liquid slab will break after about 5000 timesteps.

which leads with (3.1) to a relation that gives the form of the interface:

$$\gamma_{lv}\ \delta A_{lv} = \Delta p\ \delta V_l \tag{3.3}$$

If the interface is denoted by the function $h(z)$ with z ranging from $-L/2$ to $L/2$, (3.3) reads under a change in h

$$\gamma_{lv}\ \frac{\delta A_{lv}}{\delta h(z)} = \Delta p\ \frac{\delta V_l}{\delta h(z)} \tag{3.4}$$

with

$$A_{lv}[h] = \int_{-L/2}^{L/2} dz\ \left(1 + \left[\frac{\partial h}{\partial z}\right]^2 \right)^{1/2} \tag{3.5}$$

and

$$V_l[h] = \int_{-L/2}^{L/2} dz\ h(z) \tag{3.6}$$

(3.4) becomes

$$-\frac{\partial}{\partial z}\ \frac{\frac{\partial h}{\partial z}}{\left(1 + \left[\frac{\partial h}{\partial z}\right]^2\right)^{1/2}} = \frac{\Delta p}{\gamma_{lv}} \tag{3.7}$$

The solution of (3.7) gives that h is part of a circle. The radius R of the circle is related to the pressure difference over the interface and the surface tension by

$$R = \frac{\gamma_{lv}}{\Delta p} \tag{3.8}$$

This definition gives the radius a sign equal to the sign of Δp. The sign tells whether the curvature of the interface is positive or negative.

Secondly, we vary the free energy with respect to this radius. The variation is performed under the constraint that V_l is a constant since any equilibrium liquid-vapor interface must enclose the amount of liquid in the system. A variation of the radius is therefore equivalent to a variation in the height of the contact line The constraint neglects the dependence of the liquid density on the curvature of the surface. It is assumed that this dependence is very weak. The change in free energy upon a variation in R reads

$$\delta F = \gamma_{lv}\ \delta A_{lv} + (\gamma_{sl} - \gamma_{sv})\ \delta A_{sl} \tag{3.9}$$

The dependence of A_{lv} and A_{sl} can be read from fig. 6 which shows the case $\Delta p < 0$

$$A_{lv} = 2R\arcsin\frac{L}{2R} \tag{3.10}$$

$$V_l = h(-\frac{L}{2})\ L + R^2\arcsin\frac{L}{2R} - \frac{LR}{2}(1-\frac{L^2}{4R^2})^{1/2} \tag{3.11}$$

so that

$$A_{sl} = 2h(-\frac{L}{2}) = \frac{2}{L}\{V_l - R^2\arcsin\frac{L}{2R} + \frac{LR}{2}(1-\frac{L^2}{4R^2})^{1/2}\} \tag{3.12}$$

With the derivatives with respect to R

$$\frac{\partial A_{lv}}{\partial R} = 2\arcsin\frac{L}{2R} - \frac{L}{R}\frac{1}{(1-\frac{L^2}{4R^2})^{1/2}} \tag{3.13}$$

$$\frac{\partial A_{sl}}{\partial R} = -\frac{4R}{L}\arcsin\frac{L}{2R} + \frac{2}{(1-\frac{L^2}{4R^2})^{1/2}} \tag{3.14}$$

Equations (3.10) - (3.14) hold in the case $\Delta p > 0$ as well as $\Delta p < 0$ provided that R has the sign given by (3.8). The variation (3.9) becomes

$$\frac{\partial F}{\partial R} = (2\ \arcsin\frac{L}{2R} - \frac{L}{R}\frac{1}{(1\ -\ \frac{L^2}{4R^2})^{1/2}})(\gamma_{lv} - (\gamma_{sl} - \gamma_{sv})\frac{2R}{L}) \tag{3.15}$$

This derivative must vanish in equilibrium which yields

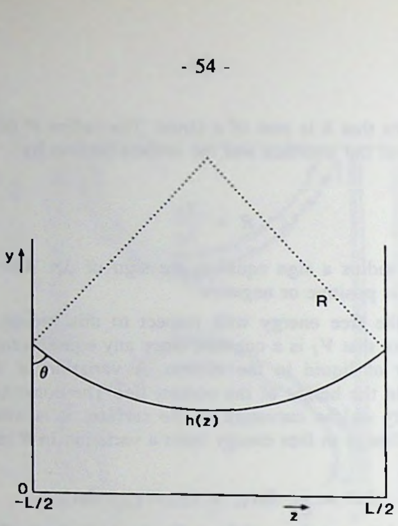

Fig. 6. The meniscus of a liquid-vapor interface confined between two walls. The walls are at $z = -L/2$ and $z = L/2$. The meniscus is denoted by the function $h(z)$ and is a part of a circle with radius R. The liquid resides below the meniscus, the vapor above. The contact angle is θ. The absence of a scale in the y-direction is due to the arbitrariness of the amount of liquid in the system.

$$\frac{\gamma_{sv} - \gamma_{sl}}{\gamma_{lv}} = -\frac{L}{2R} = \cos\theta \tag{3.16}$$

in which one recognizes Young's law. Note that the first factor of the right hand side of (3.15) is $\partial A_{lv}/\partial R$ which is unequal to zero for all finite radii. We conclude that the calculation shows that the shape of the liquid-vapor interface is a part of a circle with a radius given by (3.8) and that the contact angle satisfies Young's law.

The shape of the simulated interface is taken to be the shape of the equidensity lines. Fortunately, the lines are mostly parallel. The shape of the interface is therefore independent of the choice of a specific equidensity line in the majority of the systems. Obviously, the density profiles of figs. 1 till 5 do not show the full symmetry implied by the geometry of the system. The centre of mass of the liquid slab is not in the middle of the system in most cases. It is a result of the finiteness of the time that each system is followed. The number of timesteps appears to be too small to average out the fluctuations. But although the asymmetries prevent the full equidensity lines to be of a circular shape, parts of the lines do display this shape.

A fit of an equidensity line with a circle allows one to obtain a contact angle. Its cosine is calculated directly from the radius via (3.16). We take the equidensity line $n^* = 0.4$ for this purpose. In most cases, the asymmetries did not allow a reasonable fit of the complete line with only one segment of a circle. In that case, we assume that a local equilibrium has established itself near each wall. The two regions of local equilibrium are fitted with a different segment. Both the centre and the radius of the circles are free parameters in the fit. The distance $L/2$ in (3.16) is taken to be the distance between the centre of the circle and the position of the solid-fluid interface. There is some ambiguity in this distance since the interface's position is not sharply defined. This introduces an uncertainty of the order δ/R in $\cos\theta$, δ being approximately one in reduced units. The solid-fluid interface is always located between the outer layer of solid particles and the first absorbed fluid layer. Remark that the disturbances in the density profile caused by the fluid's layering near the wall, form no part of the macroscopic profile of the liquid-vapor interface. This disturbed region plays therefore no role in the determination of the best fitting circle.

Saville used a different method to obtain a contact angle. He determined the tangent to the equidensity line at a position close to the wall. The angle between the tangent and the planar solid-fluid interface gave him the contact angle. The disadvantages of that method are twofold. Namely, it is difficult to determine a tangent accurately and, secondly, the tangent must be determined asymptotically close to the wall. The disturbance of the equidensity lines near the wall make the latter condition a non-trivial one. The method we use is therefore more accurate. It allows one to use a much larger part of the equidensity line in the determination of the best fit. Moreover, the form of a circle excludes the use of the disturbed region in this procedure.

Our method yields at most four different values of $\cos\theta$ per density profile, namely one for each contact line. We obtained two density profiles for almost all values of ε_r, each profile being an average over 20,000 timesteps. The mean of all cosines we measured at a given ε_r determines the equilibrium cosine. The uncertainty in this value is set equal to the standard deviation obtained from the subresults. Figure 7 shows the results, together with the results of Sikkenk *et al.*

The pressure difference Δp has not been measured. An accurate measurement would require the calculation of a local pressure tensor$^{5)}$ which dependence on both y and z-direction would have to be known. Such an involved computation is beyond the capacities of the available hardware. We did however inspect the bulk densities of the liquid and vapor phase. They are shown in fig. 8 for various values of ε_r.
The figure shows a systematically decreasing vapor density. This decrease implies a systematic decrease of the vapor pressure. The pressure difference Δp must change its sign from positive for small values of ε_r to negative close to the wetting transition. A systematic decrease of the vapor pressure can therefore only be explained by an even faster decrease of the pressure in the liquid. In that case, the average pressure in the system would decrease with increasing ε_r. The liquid density scatters too much to tell anything specific about the liquid's pressure. Besides, the densities might be affected by the size of the bulk phases. The size varies with ε_r. Especially near its extremal values, either the liquid or the vapor phase becomes very thin. It seems therefore not possible to draw a conclusion about the pressure difference from the measurement of the bulk densities. Like this difference, the liquid-vapor surface tension will depend on the curvature of the surface. Although one can take the value for a planar surface as a first approximation, a significant correction could occur due to the curvature. A direct measurement of the tension however, is hindered by the lack of a well established, virial theory of the curved surface$^{7)}$. These difficulties in the determination of both Δp and γ_{lv} prevented a verification of (3.8).

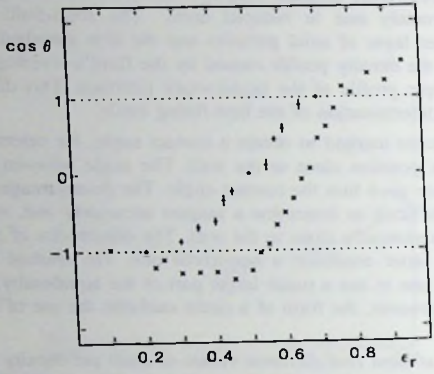

Fig. 7. The cosine of the contact angle versus ε_r from our measurements (+) and from Sikkenk *et al* (×). The error bars of their data are omitted. They are of the order $\Delta\ \cos\theta = 0.1$.

4. Conclusion

We have simulated a curved liquid-vapor interface enclosed between two walls. A visual inspection of the obtained density profiles enabled us to measure the contact angle as a function of the strength of the solid-fluid attraction. The measurements are not very accurate: the density profiles do not fully satisfy the system's geometry and the angle is determined from a fit to the equidensity lines. The fit incorporates three free parameters, the optimal choice of which was judged by the eye. Despite this subjective criterium, the global dependence of the angle on the interaction strength is clear. Its cosine increases monotonically from -1 to 1 as ε_r grows from 0.2 to 0.7. The system proved to be unstable at the extremal values 0.2 and 0.7. At $\varepsilon_r = 0.2$, the liquid slab detached from both sides of the wall after some 10,000 timesteps. It transformed into a layer in between and parallel to the sides of the wall. Both sides were completely covered with vapor in the final state. The opposite state appeared at $\varepsilon_r = 0.7$. The liquid slab lasted for about 20,000 timesteps but broke in the middle then. All the liquid was sucked against the wall such that both sides were covered with a liquid layer in the end.

Our simulations show the presence of a wetting and a drying transition. The wetting transition is estimated at $\varepsilon_w = 0.68 \pm 0.03$, the drying transition at $\varepsilon_d = 0.24 \pm 0.04$. These values might be influenced by the curvature dependence of the liquid-vapor surface tension. A quantitative estimate of this influence is hard to make[8]. The wetting transition is first order. The drying transition appears to be of the same kind. The angle however, with which our data intersects the line $\cos\theta = -1$ in fig. 7, is much smaller than the corresponding angle at the wetting transition. The first order character of the drying transition is therefore less prominent than that of the wetting transition.

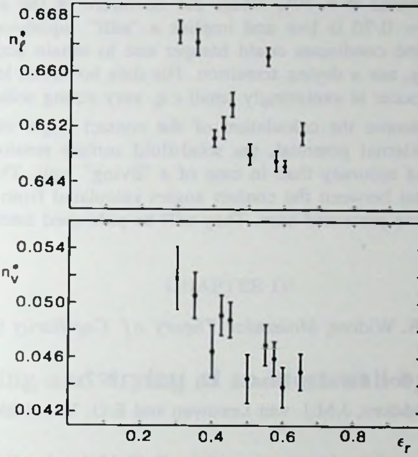

Fig. 8. The reduced liquid density n_l^* and vapor density n_v^* in systems with different ε_r. The data are averages over 40.000 timesteps. The error bars are the standard deviation of 10 subaverages over 4000 timesteps each.

Sikkenk *et al* deduced the contact angles from a measurement of the surface tensions. Figure 7 shows an appreciable discrepancy between their result and ours. They located the wetting transition at $\varepsilon_w = 0.78 \pm 0.03$ which is not too far from our estimate. But the drying transition occurred at $\varepsilon_d = 0.54 \pm 0.03$, a situation which is still partially wet according to our data. A straightforward comparison of the two curves in fig. 7 neglects the fact that Sikkenk's cosines were calculated with the liquid-vapor surface tension of a planar surface. Nevertheless, the difference between the curves can not be ascribed completely to a difference in the liquid-vapor surface tensions. Around $\varepsilon_r = 0.5$ namely, the curvature of the liquid-vapor interface is approximately zero while the difference between the two curves is at its maximum. A location of the drying transition at $\varepsilon_d = 0.20$ furthermore agrees with the behavior of the density profiles observed in Sikkenk's simulations.

This agreement combined with the difficulties in the measurement of γ_{sl} and γ_{sv} strongly plead for the correctness of the visual measurements. The drying transition takes place around $\varepsilon_r = 0.24$ rather than around $\varepsilon_r = 0.54$. The presence of stress in the wall appears to prevent a reliable measurement of a solid-fluid surface tension and hence a reliable calculation of the contact angle. The equality of a contact angle calculated from the surface tensions and a directly measured angle remains unestablished.

Saville tried to verify the equality of the two routes but in his simulation too, they led to different results. These differences might be ascribed to the system size which was rather small. The size of the box was no more than 5 σ_{ff} in the x-direction. The surface radii he encountered became approximately as small as 10 σ_{ff}. Curvature effects could play an important role in that situation. Note furthermore that the two routes do give the same result in Saville's simulation around $\theta = 70^o$, where the curvature of the surface is small. The reduced temperature $T^* = 0.70$ is low and implies a "stiff" liquid-vapor interface with a large surface tension. These conditions could hamper one to obtain accurate results. Saville observed neither a wetting, nor a drying transition. His data however, leaves open the possibility that the transitions occur at vanishingly small c.q. very strong solid-fluid attraction.

At present, we reexamine the calculation of the contact angle via Young's law. By treating the wall as an external potential, the solid-fluid surface tensions can be calculated with greater reliability and accuracy than in case of a "living" wall. The results obtained so far show a good agreement between the contact angles calculated from the tensions and the directly measured angles we presented here. They will be published later.

References

1) J.S. Rowlinson and B. Widom, *Molecular Theory of Capillarity* (Clarendon, Oxford, 1982).
2) G. Saville, J. Chem. Soc. Faraday Trans. **12,** 1122 (1977).
3) J.H. Sikkenk, J.O. Indekeu, J.M.J. van Leeuwen and E.O. Vossnack, J. Stat. Phys. **52,** 23 (1988).
4) A.F. Bakker, *Design and implementation of the Delft Molecular-Dynamics Processor* thesis, Technische Universiteit Delft, unpublished.
5) J.R. Henderson and P. Schofield, Proc. R. Soc. Lond. A **397,** 231 (1982).
6) M.J.P. Nijmeijer, A.F. Bakker, C. Bruin and J.H. Sikkenk, chapter VIII of this thesis.
7) J.R. Henderson, in *Fluid interfacial phenomena* (ed. C.A. Croxton, John Wiley & Sons, 1986).
8) S.M. Thompson, K.E. Gubbins, J.P.R.B. Walton, R.A.R. Chantry and J.S. Rowlinson, J. Chem. Phys. **81,** 530 (1984).

CHAPTER IV

Wetting and drying of an inert wall by a fluid

ABSTRACT

The contact angle in a wall-fluid system can be obtained directly from a visual inspection of the liquid-vapor meniscus or it can be calculated from the solid-liquid, solid-vapor and liquid-vapor surface tensions. These routes were exploited in two previous simulations in which the wetting of a wall was studied. Both simulations showed the existence of a wetting and a drying transition with changing wall-fluid interaction but the location of especially the drying transition was not consistent. It was suggested that the discrepancy was due to the use of a "live" wall in the measurements of the surface tensions. We have replaced the live wall by an inert wall and measured the surface tensions again, treating the wall as an external field now. The contact angles that are calculated from these measurements agree with the visual observations.

1. Introduction.

A typical situation in which wetting phenomena are discussed is the situation of a fluid at liquid-vapor coexistence in contact with a wall. The extent to which the wall is wetted by the liquid is measured by the contact angle θ which is defined as the angle between the wall and the interface between the liquid and vapor phase. The angle can vary between 0 and π. A contact angle equal to 0 means that the wall is preferably covered with liquid, the wall is called to be "completely wet". A contact angle of π means the opposite case: the wall is preferably covered with vapor and is called "completely dry". The intermediate cases $0<\theta<\pi/2$ and $\pi/2<\theta<\pi$ are called "partially wet" and "partially dry" respectively. The contact angle is related to the three surface tensions that act on the contact line -where the meniscus meets the wall- by Young's law$^{1)}$

$$\gamma_{sv} = \gamma_{sl} + \gamma_{lv} \cos\theta \tag{1.1}$$

with γ_{sv}, γ_{sl} and γ_{lv} the surface tensions of the solid-vapor, the solid-liquid and the liquid-vapor interface respectively. In case of a completely wet wall, $\gamma_{sv} = \gamma_{sl} + \gamma_{lv}$ which means that a solid-vapor interface is unstable with respect to a solid-liquid plus a liquid-vapor interface: a liquid layer will always intrude between the wall and the vapor. In case of a partially wet wall, $\gamma_{sv} < \gamma_{sl} + \gamma_{lv}$, the wall would still like to be covered with the liquid but the cost of the additional liquid-vapor interface prevents a liquid layer from intruding. Similarly, a vapor layer will intrude between the wall and the liquid if the wall is completely dry whereas the cost of the liquid-vapor interface prevents this intrusion in the partially dry state.

Surface tensions change with e.g. temperature or strength of the solid-fluid interaction; so a transition from the partially dry to the completely dry or from the partially wet to the completely wet state is possible. These transitions are genuine phase transitions, called the "drying" and "wetting" transition and their nature and location have attracted much attention in recent years.

The contact angle can be measured in a system where the meniscus actually meets the wall such as in a capillary, partially filled with liquid. The angle with which the meniscus borders at the wall can be obtained from a visual inspection of such a system. Young's law gives a second route to this angle: it can be calculated from a measurement of the surface tensions. Both routes were exploited in a molecular dynamics simulation by Saville$^{2)}$ in a study of Young's law. Saville enclosed a liquid and a coexisting vapor phase between two parallel walls, represented as external potentials with a variable interaction strength. The meniscus was defined as a plane of constant density, in between the liquid and the vapor density. By placing the liquid slab perpendicular to the walls, Saville obtained a meniscus that meets the wall and thus, he could measure the contact angle visually. With the slab parallel to the walls, he obtained a common geometry to measure surface tensions and from the latter, Saville calculated the contact angles. Unfortunately, the two routes did not agree upon the value of the angle.

The confrontation of a visually measured contact angle with a calculated one also appeared in the comparison of two other, closely related simulations$^{3,4)}$, the first one by Sikkenk *et al*, the second by the present authors. The type of wall and fluid, the temperature etc., were the same in both simulations. As in Saville's simulations, the liquid and vapor phase were enclosed between two parallel walls but in Sikkenk's and our simulations, the walls were formed by a lattice of solid particles which were allowed to oscillate around their lattice positions. Therefore, the walls represented a thermodynamic phase rather than an external potential. The wetting properties of the system were varied by changing the interaction strength between the solid and the fluid. The liquid slab was placed parallel to the walls in the first series of simulations$^{3)}$ and the contact angles were calculated from measurements of the surface tensions. Starting from the completely dry state and increasing the interaction strength, a drying transition and subsequently a wetting transition were encountered, both of first order. The location of the drying transition however, was at variance with the behaviour of the density profiles. Whereas the contact angles predicted a completely dry wall for a certain range of attractive strengths, it was observed in the same range that a liquid layer, placed between the walls, was eventualy adsorbed at one of them. This spontaneous transition from a completely dry to a partially dry state indicated that the latter state was preferred by the system although the contact angles implied the reverse. Van Swol$^{5)}$ remarked that the calculation of the solid-fluid surface tensions could be a source of errors. The presence of stress in a "live" wall could have influenced the measurement of these surface tensions and in this way have affected the contact angle.

This hypothesis was tested in the second series of simulations$^{4)}$. We placed the liquid slab perpendicular to the walls and measured the contact angle visually. Thus circumventing the calculation of a solid-fluid surface tension, we obtained once more a series of contact angles which showed a drying and a wetting transition under variation of the wall-fluid interaction. The location of the wetting transition was not too far from the result of the first experiment but the drying transition was strongly shifted. Fortunately, it was now located at a position consistent with the behaviour of the density profiles in the previous experiment.

The simulations of Sikkenk *et al* initiated a density functional calculation$^{6)}$ of the wetting properties of the same wall-fluid system. With a non-local density functional combined with an "effective attractive interaction" and including the effects of substrate roughness, Velasco and Tarazona obtained a drying transition which was much closer to the result later on given by the second experiment. The wetting transition was again found to be in the region predicted by both simulations. Moreover, the calculation yielded a stronger first order character in case of the wetting, than in case of the drying transition. The same difference in character had been observed in the visual measurements of the contact angle.

This paper is addressed to a third measurement of contact angles in a wall-fluid system which is the same as before apart from the representation of the wall. By taking an inert wall, the difficulties of determining γ_{sl} and γ_{sv} should be diminished since such a wall is not subject to the effects of stress. Thereby, we hope to achieve consistency between surface tension measurements on the one hand and direct measurements of the contact angle on the other hand. For that purpose, the conditions of the simulations were taken exactly the same as in the previous study$^{3)}$ except for the treatment of the wall particles. Earlier simulations have indicated that the motion of the wall particles is not important for the behaviour of the fluid.

2. Description of the simulations.

The system is the same as described before$^{3)}$ apart from the fact that we fix the solid particles at the positions of a perfect lattice. The fluid particles move in a three dimensional, cubic box with periodic boundary conditions in all directions. The interaction potential ϕ_{AB} between a particle of type A and a particle of type B is of the Lennard-Jones 12-6 form:

$$\phi_{AB}(r) = 4\varepsilon_{AB} \{(\sigma_{AB}/r)^{12} - (\sigma_{AB}/r)^{6}\} \tag{2.1}$$

where A and B stand for either "solid" or "fluid", r denotes the distance between the particles, ε_{AB} sets the energy scale and σ_{AB} the length scale of the potential. The interaction potentials are cut off at $2.5\sigma_{AB}$. The length of the box equals $L = 29.1\sigma_{ff}$.

The solid substrate is built of three layers of a FCC lattice which requires 2904 solid particles. The layers form the (100) planes of the solid and are placed in the x-y plane of the computational box. The particles are fixed at their lattice positions and not allowed to move. The lattice spacing is determined by σ_{ss}, chosen as $\sigma_{ss} = 0.847\ \sigma_{ff}$. This mismatch between σ_{ss} and σ_{ff} prevents a solidification of the first adsorbed fluid layers.

Due to the periodic boundary conditions, the fluid is enclosed in the z direction between the third and the first layer of the lattice. Therefore, there are two solid-fluid interfaces present in the computational box: one at each side of the wall. The system contains some 8500 fluid particles, an amount which ensures the presence of both a liquid and a vapor phase. The interaction strength ε_{sf} between solid and fluid is varied in the simulations and the wetting behaviour is studied as a function of the relative interaction strength $\varepsilon_r = \varepsilon_{sf}/\varepsilon_{ff}$. The length scale σ_{sf} of this interaction is close to the mean of σ_{ss} and σ_{ff}: $\sigma_{sf} = 0.941\ \sigma_{ff}$ 7). The temperature of the system is kept fixed at $T^* = k_B T/\varepsilon_{ff} = 0.9$ which is in between the fluid's triple point temperature $T_t^* \simeq 0.7$ and the critical temperature $T_c^* \simeq 1.26$. The reduced timestep $\Delta t^* = \Delta t\sqrt{\varepsilon_{ff}}/(\sigma_{ff}\sqrt{m_f})$ in the simulations was set to 0.01 where m_f denotes the mass of a fluid particle. The simulations were carried out on a special purpose computer: the Delft Molecular Dynamics Processor (DMDP).

We place a liquid slab in between and parallel to the two sides of the wall. It has been discussed before 3,8) that the following three cases can occur.

a) For low values of ε_r, the liquid layer resides in the middle of the system and both sides of the wall are covered with vapor, see fig. 1 which shows the reduced fluid density $n^* = n\sigma_{ff}^3$ as a function of $z^* = z/\sigma_{ff}$. This situation is the completely dry case, it has a total surface tension of

$$\gamma_{tot} = 2\gamma_{sv} + 2\gamma_{lv} \tag{2.2}$$

b) Increasing ε_r, the liquid is adsorbed at one side of the wall, see fig. 2. This asymmetric configuration is the partially dry or partially wet case. The total surface tension equals

$$\gamma_{tot} = \gamma_{sl} + \gamma_{lv} + \gamma_{sv} \tag{2.3}$$

c) Finally, for large ε_r, both sides of the wall prefer to be covered with liquid, see fig. 3. This is the completely wet case with a total surface tension

$$\gamma_{tot} = 2\gamma_{sl} + 2\gamma_{lv} \tag{2.4}$$

Comparing the total surface tension of a and b, one recognizes that the transition from a to b takes place at the drying point, i.e. $\theta = \pi$ in (1.1). The transition from b to c takes place at

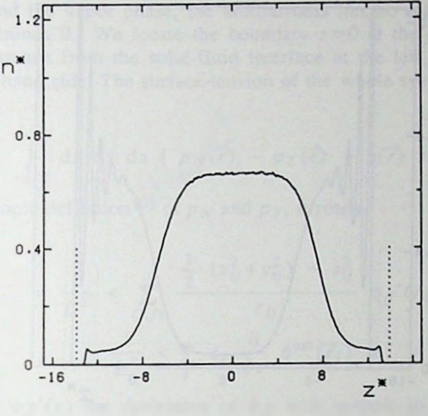

Fig. 1. Symmetric dry density profile at $\varepsilon_r = 0.1$ obtained from an average over 3200 particle configurations generated in a run of 41,600 timesteps. The dotted lines denote the positions of the outer layers of the wall. For convenience, the origin $z^* = 0$ has been placed in the middle.

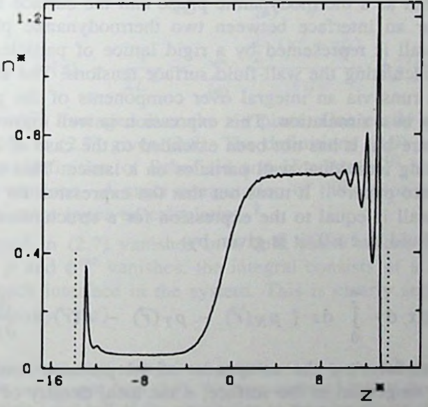

Fig. 2. Asymmetric density profile at $\varepsilon_r = 0.5$ as averaged over 2400 particle configurations generated in 31,200 timesteps. Further as fig. 1.

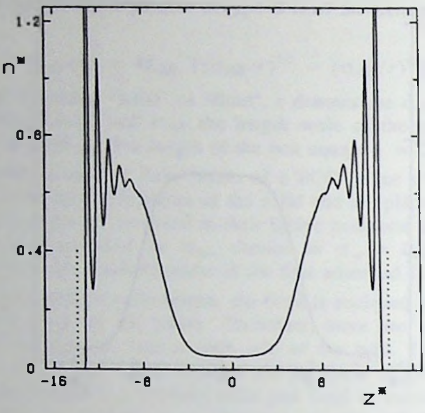

Fig. 3. Symmetric wet density profile at $\varepsilon_r = 0.8$, further as fig. 1.

the wetting point $\theta = 0$.

The solid-fluid surface tensions are measured differently from the previous procedure[3)] where the wall was treated as a thermodynamic phase and the surface tension was measured in a way appropriate for an interface between two thermodynamic phases. In the present experiment, where the wall is represented by a rigid lattice of particles, one encounters the following difficulty in calculating the wall-fluid surface tensions. The standard way to measure the surface tensions runs via an integral over components of the pressure tensor which can be measured directly in a simulation. This expression is well known for a wall potential that has no lateral structure but it has not been extended to the case of a structured wall such as we encounter by placing individual wall particles on a lattice. This extension is nontrivial and presented in a separate paper[9)]. It turns out that the expression for the wall-fluid surface tension of a structured wall is equal to the expression for a structureless wall. With the wall located at $z=0$ and the fluid at $z>0$, it is given by:

$$\gamma_{sf} = \frac{1}{A} \int_A dx\, dy \int_0^\infty dz \, \{ \, p_N(\vec{r}) - p_T(\vec{r}) - n(\vec{r}) \, z \, \frac{\partial}{\partial z} \, \phi^{ext}(\vec{r}) \, \} \tag{2.5}$$

with A the area of the surface, p_N the component of the pressure tensor normal to the surface, p_T the component tangential to the surface, n the local density of the fluid and ϕ^{ext} the external potential that forms the wall. In our case, the external potential is given by

$$\phi^{ext}(\vec{r}) = \sum_l \phi_{sf}(|\vec{r} - \vec{d}_l|) \tag{2.6}$$

where the sum is over all lattice positions $\vec{d}_l$. Note that the surface tension depends on the location of the origin $z=0$. A shift of this integration boundary with δz changes the surface tension with an amount $-p\delta z$ with p the pressure in the fluid. Since the pressure is the same in the liquid and the vapor phase, the arbitrariness has no influence on the difference $\gamma_{sv}-\gamma_{sl}$ which determines θ. We locate the boundary $z=0$ at the middle layer of the wall which is at equal distance from the solid-fluid interface at the left hand and the solid-fluid interface at the right-hand side. The surface tension of the whole system reads in our case

$$\gamma_{tot} = \frac{1}{L^2} \int_{-L/2}^{L/2} dx\, dy\, dz \; \{ \; p_N(\vec{r}) \; - \; p_T(\vec{r}) \; - \; n(\vec{r}) \; z \; \frac{\partial}{\partial z} \; \phi^{ext}(\vec{r}) \; \} \tag{2.7}$$

Inserting the microscopic definition$^{10)}$ of p_N and p_T, it reads

$$\gamma_{tot} = \frac{1}{L^2} < \sum_{(i,j)} \frac{\frac{1}{2}\,(x_{ij}^2+y_{ij}^2) \; - \; z_{ij}^2}{r_{ij}} \; \phi_{ff}'(r_{ij}) > \\ - \frac{1}{L^2} < \sum_i z_i \frac{\partial}{\partial z} \; \phi^{ext}(\vec{r}_i) > \tag{2.8}$$

with $\vec{r}_{ij} = \vec{r}_i - \vec{r}_j$, $\phi_{ff}'(r)$ the derivative of ϕ_{ff} with respect to r and $< >$ a canonical ensemble average. The first summation in (2.8) is over all pairs of fluid particles (i,j), the second summation over single fluid particles i. We measure a $p_N(z)$ and $p_T(z)$ defined by

$$p_N(z) \; = \; k_B T \; n(z) \; - \; \frac{1}{2L^2} \; < \sum_{i \neq j} \frac{z_{ij}^2}{r_{ij}} \; \phi_{ff}'(r_{ij}) \; \delta(z-z_i)> \tag{2.9}$$

$$p_T(z) \; = \; k_B T \; n(z) \; - \; \frac{1}{2L^2} \; < \sum_{i \neq j} \frac{\frac{1}{2}\,(x_{ij}^2+y_{ij}^2)}{r_{ij}} \; \phi_{ff}'(r_{ij}) \; \delta(z-z_i)> \tag{2.10}$$

with $n(z)$ the density $n(\vec{r})$ averaged over the x-y plane. One easily verifies that the substitution of (2.9) and (2.10) in (2.7) gives (2.8). The definitions (2.9) and (2.10) do not strictly conform to the general definition of Schofield and Henderson$^{10)}$ but this modification does not affect the surface tensions. A strict computation of the tensor according to their scheme would require a much more involved calculation [\$].

Since the integrand in (2.7) vanishes in a bulk phase where p_N and p_T both become equal to the pressure p and ϕ^{ext} vanishes, the integral consists of a number of separate contributions, one from each interface in the system. This is clearly seen in fig. 4 which shows the "surface tension density" $\gamma(z)$

[\$] Considering e.g. p_N, the contribution of a pair of particles (i,j) to the integral over p_N is given by $z_{ij}^2 \phi_{ff}'(r_{ij})/r_{ij}$ as can be seen from (2.9). We have attributed half of this contribution to the z-coordinate of particle i and half of the contribution to the z-coordinate of particle j to obtain a local p_N. According to the general definition$^{10)}$, one should draw a contour between particles i and j and distribute the contribution of the pair over the contour in a well-specified manner. Different choices of contour correspond to different microscopic definitions of p_N. The spatial distribution of the contribution of the pair (i,j) however, is irrelevant for the integral over p_N. In other words: the integral over p_N is independent of its microscopic definition.

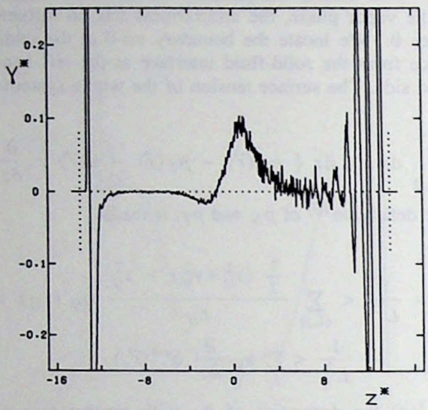

Fig. 4. "Surface tension density" profile at $\varepsilon_r = 0.5$ as averaged over 2400 particle configurations generated in 31,200 timesteps. Further as fig. 1. The reduced surface tension density $\gamma^*(z)$ is defined as $\gamma^*(z)=\gamma(z)\sigma_{ff}^2/\varepsilon_{ff}$.

$$\gamma(z) = p_N(z) - p_T(z) - \frac{1}{L^2}\int_{-L/2}^{L/2} dx\, dy\, n(\vec{r})\, z \frac{\partial}{\partial z} \phi^{ext}(\vec{r}) \qquad (2.11)$$

of the asymmetric system of fig. 2. The contribution of an individual interface is the interface's surface tension which is therefore obtained by restricting the integration over z in (2.7) to an integration over the surface alone.

3. Results.

As before[3)], we simulated a series of asymmetric systems and symmetric dry and wet systems at various ε_r. A symmetric dry starting configuration at $\varepsilon_r=0.1$ was obtained by melting a strip of fluid particles, placed between the walls on a lattice with approximately the appropriate liquid density. An asymmetric starting configuration was obtained by choosing $\varepsilon_r=0.5$ whereupon the same initial strip was adsorbed at one of the sides of the wall during the melting process. A symmetric wet starting configuration resulted from the use of two strips, each one placed near one of the sides of the wall with $\varepsilon_r=0.8$. Systems at different ε_r were obtained by changing ε_r. A newly formed system was equilibrated for approximately 15,600 timesteps before the measurements started. This equilibration time was sufficient to stabilize the particle density profile, the energy of the system and other quantities in most cases. The particle density and surface tension density profiles were sampled each 13^{th} or 15^{th} timestep until an average over some 3200 configurations was obtained. Error bars in the data denote the standard deviation as calculated from subaverages over 400 configurations.

The properties of the bulk liquid and bulk vapor phase and the properties of the liquid-vapor interface should be independent of ε_r. It has been verified that this independence

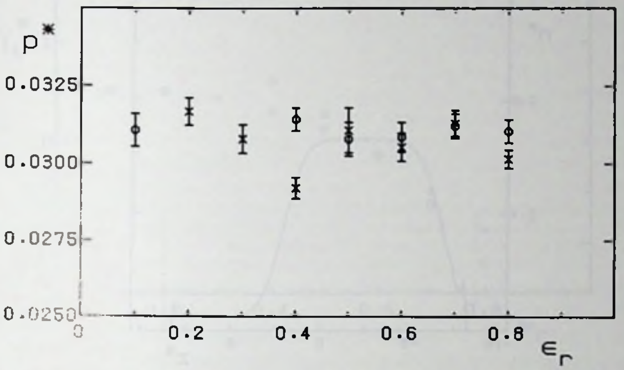

Fig. 5. Reduced pressure $p^*=p\sigma_{ff}^3/\epsilon_{ff}$ as a function of ϵ_r. Circles denote the symmetric systems, crosses the asymmetric systems.

holds for the reduced bulk densities n_l^* and n_v^* and the reduced liquid-vapor surface tension γ_{lv}^* where the latter is listed in table 1. These quantities fluctuate with varying ϵ_r but show no systematic dependence. Averaged over all ϵ_r, their mean values are $n_l^*=0.6640\pm0.0006$, $n_v^*=0.0456\pm0.0006$ and $\gamma_{lv}^*=0.225\pm0.005$, which corresponds with results obtained in a simulation[11)] of a free liquid-vapor interface. Another check on the influence of ϵ_r is a measurement of the pressure in the system which should also be unaffected by ϵ_r. The pressure p can be calculated from[9)]

$$p = \frac{1}{L^3} \int_{-L/2}^{L/2} dx\, dy\, dz\ \{\ p_N(z) - n(\vec{r})\ z\ \frac{\partial}{\partial z}\ \phi^{ext}(\vec{r})\ \} \tag{3.1}$$

The result is plotted in fig. 5 which shows a pressure that does not vary systematically with ϵ_r but fluctuates around an average value of $p^*=0.0308\pm0.0002$.

The completely dry state with the liquid slab in the middle of the system remains stable at $\epsilon_r=0.1$, see fig.1. Increasing ϵ_r to 0.2, one observes a transition to the asymmetric system of fig. 6, the liquid layer being adsorbed at one of the sides of the wall. Before the state of fig. 6 was obtained, the liquid slab, which was initially in the middle of the system, had first collided with the wall at the right whereupon it reflected back and was adsorbed at the left wall. The whole transition from a symmetric dry to the asymmetric system took about 60,000 timesteps. The liquid layer remained adsorbed at the left side of the wall during the 57,000 timesteps we followed it. The precise location of the symmetric-asymmetric transition is hard to tell since it is difficult to determine whether the solid-liquid interface one obtains at $\epsilon_r=0.2$ is indeed a stable solid-liquid interface or should be regarded as a metastable state in which the system is easily trapped due to the limited space between the walls while the completely dry state is the true equilibrium state.

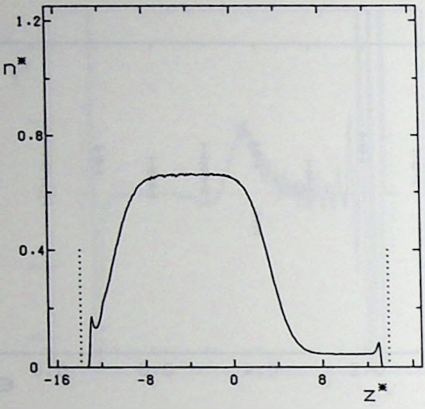

Fig. 6. Asymmetric density profile at ε_r = 0.2, further as fig. 1.

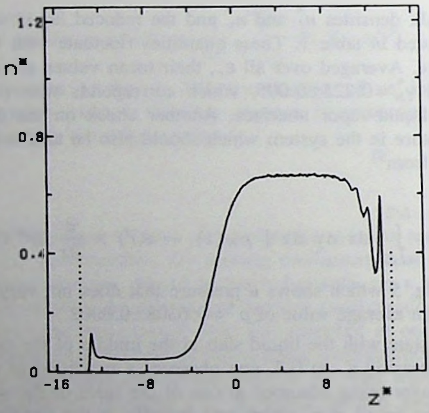

Fig. 7. Asymmetric density profile at ε_r = 0.3, further as fig. 1.

The state at $\varepsilon_r = 0.3$ is far less controversial. Starting with a symmetric dry system, one obtains an asymmetric system with a solid-liquid interface which clearly differs from the solid-vapor interface, c.f. fig 7. The transition from a symmetric dry to an asymmetric system took about 30.000 timesteps in the case $\varepsilon_r = 0.3$.

If we start with an asymmetric system at $\varepsilon_r > 0.2$ and lower ε_r, we observe the inverse transition. At $\varepsilon_r = 0.2$, the asymmetric system evolves again to a system similar to the one of

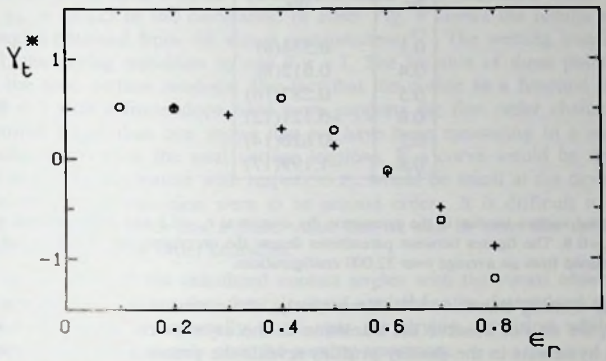

Fig. 8. Reduced total surface tension γ^*_{tot} as a function of ε_r. Circles denote the symmetric systems, crosses the asymmetric ones. The symmetric value at $\varepsilon_r=0.2$ is constructed (see text). The experimental uncertainty is of the order of the symbol size.

ε_r	γ^*_{lv}	γ^*_{sl}	γ^*_{sv}	γ^*_{tot}	cosθ
0.2	0.240(3)	0.263(7)	0.0298(7)	0.533(6)	−1.04(3)
0.3	0.219(7)	0.207(10)	0.0177(8)	0.444(15)	−0.84(5)
0.4	0.207(11)	0.101(8)	−0.0067(6)	0.302(16)	−0.48(4)
0.5	0.234(10)	−0.066(11)	−0.0400(16)	0.128(18)	0.12(5)
0.6	0.241(15)	−0.280(10)	−0.0990(26)	−0.138(20)	0.80(3)
0.7	0.214(11)	−0.541(7)	−0.1653(43)	−0.492(10)	1.67(3)
0.8	0.223(9)	−0.827(14)	−0.2747(45)	−0.879(16)	2.45(6)

Table 1. Reduced surface tensions of the liquid-vapor, solid-liquid and solid-vapor interface, reduced total surface tension and the cosine of the contact angle in the asymmetric systems. The figures between parentheses denote the uncertainty (one standard deviation) in the last or last two digits. The reported γ^*_{sv} at $\varepsilon_r=0.7$ and 0.8 are the surface tensions of the metastable solid-vapor interfaces encountered in the asymmetric systems whereas one has $\gamma^*_{sv} = \gamma^*_{sl}+\gamma^*_{lv}$ in equilibrium since the wall is completely wet. The cos θ of this metastable branch are larger than 1. Most results are obtained from an average over 32,000 configurations.

fig. 6. Decreasing ε_r to 0.1, we obtain a system with two solid-vapor interfaces although even in this case, the liquid phase remains near the wall it just detached from and stays slightly off center during at least 60,000 timesteps.

The behavior of the density profiles thus shows the existence of a drying transition at $\varepsilon_r \approx 0.2$. We can not observe any hysteresis in the location of the transition which indicates that it is possibly second, at least not strongly first order. The situation is quite different at the wetting transition. If we start with an asymmetric configuration and increase ε_r, we never observe a transition to a symmetric wet state, not even at $\varepsilon_r > 1$ which

ε_r	γ_{tot}
0.1	0.534(8)
0.4	0.612(8)
0.5	0.287(16)
0.6	−0.121(12)
0.7	−0.620(14)
0.8	−1.199(17)

Table 2. Reduced total surface tension in the symmetric dry system at $\varepsilon_r=0.1$ and the symmetric wet systems from $\varepsilon_r=0.4$ till $\varepsilon_r=0.8$. The figures between parentheses denote the uncertainty in the last or last two digits. Most results are obtained from an average over 32,000 configurations.

is well above the wetting transition[3,4]. Reversively, if we start with a symmetric wet state and decrease ε_r, we do not observe the transition to the asymmetric state, even not at ε_r as low as 0.4. This hysteresis in the density profiles reveals the presence of a first order wetting transition but prevents an accurate location of the transition from the behaviour of the profiles.

The second route to the location of the transitions is the measurement of the total surface tension in the various systems, the results of which are shown in fig. 8 and listed in the tables 1 and 2. The results are most clear at the wetting side where the strong hysteresis allows one to measure the surface tension of both the symmetric and the asymmetric state over a wide range of ε_r. The two curves intersect at $\varepsilon_r \approx 0.6$, below which the partially wet state is thermodynamically favorable, above which the completely wet state is preferred. The intersection point locates the wetting transition. One could argue that the total surface tension of the completely wet state is not well described by (2.4) since the liquid phases in these states are very small and the solid-liquid and liquid-vapor interfaces are not well separated. In that case, the location of the wetting transition as the intersection point in fig. 8 would be incorrect. The effect of the finite size can be checked by calculating the total surface tension of a well developed, symmetric state from (2.4) with γ_{sl} as obtained in an asymmetric system and $\gamma_{lv}=0.225$. It turns out that γ_{tot} calculated in this way does not significantly differ from γ_{tot} as we measure it in the completely wet systems. Therefore, the restriction on the size of the symmetric wet systems turns out to have no significant effect on the location of the wetting transition.

There is no hysteresis at the drying side. At $\varepsilon_r=0.2$ however, we can once more address the question of the stability of the system of fig. 6 by comparing its total surface tension with the total surface tension of a completely dry system. The latter can be constructed from (2.2) with γ_{sv} measured in the asymmetric system of fig. 6 and $\gamma_{lv}=0.225$. As shown in fig. 8, the two surface tensions can not be distinguished, showing that the solid-liquid interface of fig. 6 has the same thermodynamic probability as a solid-vapor plus a liquid-vapor interface. The same comparison at $\varepsilon_r=0.3$ (not included in fig. 8) shows that the total surface tension of the system of fig. 7 is slightly below the constructed surface tension of a hypothetical, symmetric dry state. We stress once more that the total surface tension in fig. 8 depends on the choice of origin $z=0$ but that the location of the intersection point is unaffected by this choice.

The last route to the wetting and drying transition is the calculation of the contact angles from the surface tensions. The angles are measured in the asymmetric systems which provide at the same time a solid-liquid and a solid-vapor interface while we used a fixed value of $\gamma_{lv} = 0.225$ in the calculation of $\cos\theta$. Fig. 9 shows the results together with the contact angles obtained from the visual measurements[4)]. The wetting transition is given by $\cos\theta = 1$, the drying transition by $\cos\theta = -1$. The location of these points is the same as given by the total surface tensions. The fact that the cosine as a function of ε_r crosses the line $\cos\theta = 1$ with a finite slope once more supports the first order character of the transition. A cosine larger than one shows that we have been measuring in a metastable state, a fact we also observed in the total surface tensions. If a curve would be drawn through the measured angles, its derivative with respect to ε_r would be small at the drying transition and should be zero if the transition were to be second order. It is difficult to tell whether the derivative is indeed zero or has a finite value but we can be sure that the drying transition has at most a weakly first order character.

The comparison of the calculated contact angles with the visual observations in fig. 9 shows that they coincide but that the calculated angles can be determined with greater accuracy. The comparison is especially good near the drying transition while the calculated angles rise slightly more steeply near the wetting transition.

The visually measured angles differ marginally from the angles presented in the original paper[4)]. The angles were obtained by fitting a circle to the liquid-vapor meniscus, a fit which was performed manually in the original work but which we have done presently numerically to exclude the possibility of uncontrolled errors which is inherent to a manual procedure. The numerical method, a least square fit, gives angles that vary a little bit smoother with ε_r but does not shift the curve as a whole. In particular, our estimates[4)] of the position of the wetting and drying transition are not altered.

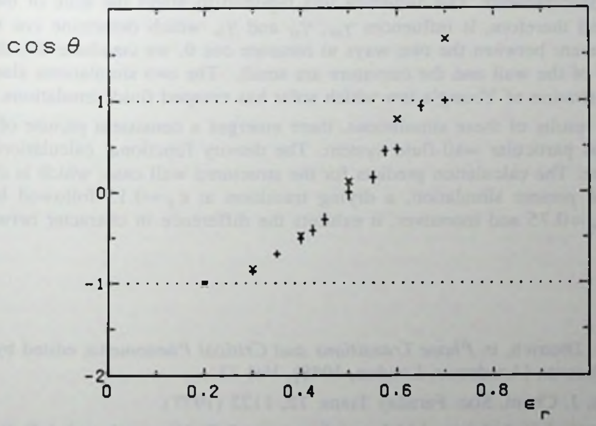

Fig. 9. Cosine of the contact angle versus ε_r. The crosses × are the results as calculated from Young's law in these simulations, the errors are of the order of the symbol size, c.f. table 1. The crosses + are the visual observations[4)], the length of the vertical bar gives the error.

4. Conclusions.

We have examined the wetting properties of a wall-fluid system in a simulation very similar to the one performed by Sikkenk *et al* but with the "live" wall replaced by an inert wall. Of the three routes to the location of the wetting and drying transition, only the behavior of the density profiles is the same as reported previously$^{3)}$. The other two routes involve the measurement of the solid-fluid surface tension, a measurement that is difficult with a live wall which can support stress. We have shown that the replacement of the live by an inert wall removes the inconsistency near the drying transition between the contact angles and the behavior of the profiles$^{3)}$. In the inert case, the three routes all agree on a location of this transition at $\varepsilon_d = 0.20 \pm 0.05$, to be compared with the estimate$^{3)}$ of $\varepsilon_d = 0.54 \pm 0.03$. The drying transition we observe is weakly first or second order. There occurs a relatively smaller shift in the location of the wetting transition. This location can not be obtained with any accuracy from the behavior of the density profiles but it appears very clearly in the data of the total surface tension and the contact angle. From these two routes, we estimate a strongly first order wetting transition to occur at $\varepsilon_w = 0.62 \pm 0.01$, compared with $\varepsilon_w = 0.78 \pm 0.03$ as reported in the previous reference$^{3)}$. Part of these differences could be ascribed to the difference in type of wall but we expect that the relatively small oscillations of the wall particles around their equilibrium positions, have little effect on the location of the transitions.

Moreover, our contact angle measurements agree with the visual measurements$^{4)}$. Those simulations gave estimates of $\varepsilon_d = 0.24 \pm 0.04$ and $\varepsilon_w = 0.68 \pm 0.03$, which coincide with the present measurements. The comparison could again be invalidated by the difference in type of wall and, additionally, by the curvature of the liquid-vapor interface that appears in the visual measurements. The curvature was reported to affect the state of the liquid and vapor phase and therefore, it influences γ_{sv}, γ_{sl} and γ_{lv} which determine cos θ. However, from the agreement between the two ways to measure cos θ, we conclude that the effects of the freezing in of the wall and the curvature are small. The two simulations also provide an explicit demonstration of Young's law which sofar has escaped fluid simulations.

From the results of these simulations, there emerges a consistent picture of the wetting behavior of this particular wall-fluid system. The density functional calculation$^{6)}$ is in line with this picture. The calculation predicts for the structured wall case, which is closest to the situation in the present simulation, a drying transition at $\varepsilon_d = 0.15$ followed by a wetting transition at $\varepsilon_w = 0.75$ and moreover, it exhibits the difference in character between the two transitions.

References

1) see e.g. S. Dietrich, in *Phase Transitions and Critical Phenomena,* edited by C. Domb and J. Lebowitz (Academic, London, 1988), Vol 12.

2) G. Saville, J. Chem. Soc. Faraday Trans. **12,** 1122 (1977).

3) J.H. Sikkenk, J.O. Indekeu, J.M.J. van Leeuwen, E.O. Vossnack and A.F. Bakker, J. Stat. Phys. **52,** 23 (1988).

4) M.J.P. Nijmeijer, C. Bruin, A.F. Bakker and J.M.J. van Leeuwen, chapter III of this thesis.

5) F. van Swol, Phys. Rev. Lett. **60,** 239 (1988).

6) A. Velasco and P. Tarazona, J. Chem. Phys. **91,** 7916 (1989).

7) Erroneously, σ_{sf} was mentioned to be $0.912\sigma_{ff}$ in previous work[3,4,8] while the simulations were carried out with $\sigma_{sf}=0.941\sigma_{ff}$ as in this work.

8) J.M.J. van Leeuwen, M.J.P. Nijmeijer and C. Bruin, Physica Scripta **T25,** 256 (1989).

9) M.J.P. Nijmeijer and J.M.J. van Leeuwen, chapter II of this thesis.

10) D. Schofield and J.R. Henderson, Proc. R. Soc. Lond. A **379,** 231 (1982).

11) M.J.P. Nijmeijer, A.F. Bakker, C. Bruin and J.H. Sikkenk, chapter VIII of this thesis.

CHAPTER V

Accurate determination of the location and order of the drying transition

ABSTRACT

The wetting transition is mostly found to be first-order but the nature of the drying transition in realistic systems is debated. We have simulated the wetting and drying of a wall and, by a careful inspection of the variation of the contact angle on the approach of the transition, find strong evidence for a continuous drying transition. Moreover, the drying point is located an order of magnitude more accurately with respect to previous attempts.

Accurate determination of the location and order of the drying transition.

Wetting and drying phase transitions have drawn a substantial interest in the past decade[1)] not only for their importance in technical applications but also as demonstrations of genuine surface phase transitions. After their discovery by Cahn[2)] and by Ebner and Saam[3)] on theoretical grounds and the experimental demonstration by Moldover and Cahn[4)], most of the theoretical studies have taken place in the context of lattice models[5)], on a mesoscopic level as variants of Landau's mean-field theory[1,6)] or in the framework of density functional theories[7,8)]. None of these theories is capable of making an accurate prediction for the nature of the wetting and drying transitions for realistic systems. The lattice gas models involve interactions which are too much simplified to describe the delicate balance between the driving forces in the wetting or drying of a real substrate. In its simplest form, the basic symmetry between particles and holes makes wetting and drying two mirror images of the same physical mechanism. The Landau type mean field theories help to classify the possible scenarios for wetting and drying but cannot make contact with a microscopic Hamiltonian. Density functional theory should in principle be able to yield information on the phase diagram of realistic systems and some impressive results have indeed been obtained e.g. by Velasco and Tarazona[8)]. The strength and weakness of the density functional theory have recently been reviewed by van Swol and Henderson[7)]. A basic difficulty is an adequate density functional for the liquid-vapor coexistence region which is vital for the description of wetting and drying.

In this situation, computer simulations[9,10,11,12)] are most welcome but so far rare because a large system is needed to accomodate the various phases involved and large fluctuations occur near the phase transitions which slow down the approach to equilibrium. Simulations are especially useful as density functionals can be tailored to study the system that is simulated and the results of the calculation and the computer experiment can be compared directly. There is general agreement about the wetting transition. All simulations point at a first-order phase transition, which is supported in one case by the observation[13)] of the accompanying prewetting phenomenon. Also the agreement between density functional theory and the simulation on the location of the wetting point is satisfactory. The situation about the drying point is less clear. The simulation[9)] of van Swol and Henderson indicates a first-order drying transition. They argue that this is to be expected since the fluid's structure has to interpolate smoothly, even at positions close to the substrate, between a substrate-liquid and a substrate-vapor interface in case of a continuous transition. They consider such a smooth interpolation to be unlikely. Nevertheless, the density functional calculation they carried out subsequently, predicts a continuous (second order) drying transition which is also located rather far from the simulation result. Whether this is due to insufficient or inaccurate simulation data is a point of debate[14)]. As their simulations and density functional theory apply to square-well molecules, their conclusions cannot be easily transferred to more realistically interacting particles. Velasco and Tarazona carried out a density functional calculation on a Lennard-Jones system and found the drying transition to be weakly first-order. Their location of the transition was initially inconsistent with the results of the simulation[10)] of Sikkenk *et al* but this discrepancy has been removed by improved simulations[11,12)]. While these simulations conformed the result of Velasco and Tarazona on the location of the drying transition, they could not decide on its order but were consistent with a continuous as well as a weakly first-order transition. In this letter, we describe a simulation experiment which improves the accuracy by an

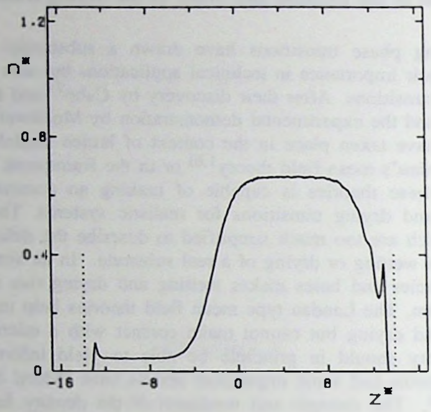

Fig. 1. The fluid's density n averaged over the x-y plane as a function of the position z between the outer layers of the wall. The density and position are expressed in reduced units: n^* equals n/σ_{ff}^3 and z^* denotes z/σ_{ff}. The dotted lines give the positions of the outer wall layers. The profile is calculated as an average over 5200 particle configurations, obtained in a run of 67,600 timesteps at $\varepsilon_{sf}=0.25\varepsilon_{ff}$.

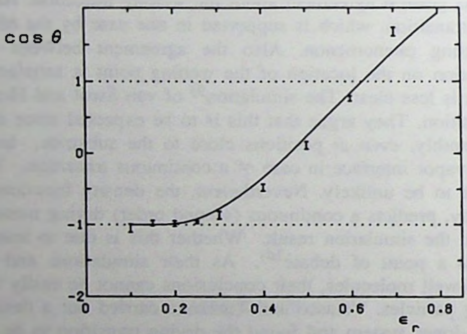

Fig. 2. cosθ as a function of ε_r. The bars denote the measured cos θ, the curve is obtained by integrating the $\partial\cos\theta/\partial\varepsilon_{sf}$ data (see fig. 3). The lengths of the bars denote the uncertainty in the measurement. They are calculated as the standard deviation in subaverages over 5200 timesteps each. The data points comprise 5 to 25 subaverages.

order of magnitude thereby clarifying the simulation results on the drying point.

The simulated system[10,12] consists of a three-dimensional cubic box with periodic boundary conditions in which a substrate is constructed by three layers of a FCC lattice of substrate particles. The remaining volume is occupied by a Lennard-Jones fluid consisting of a liquid and a vapor phase at a fixed temperature. By the boundary conditions, the fluid can wet or dry both sides of the substrate wall (see fig. 1). The Lennard-Jones interactions ϕ_{AB} between particles of type A and B, where A and B stand for s in case of a solid and f in case of a fluid particle, are characterized by an energy scale ε_{AB} and a length scale σ_{AB}. They are truncated at $2.5\sigma_{AB}$. The reduced temperature T^*, defined as $T^* = k_B T/\varepsilon_{ff}$ is kept at 0.9 and the system contains about 8500 fluid particles in a box with a linear dimension L of $29.1\sigma_{ff}$. We are able to simulate such large systems for long simulation runs because of the availability of a special purpose computer: the Delft Molecular-Dynamics Processor (DMDP)[15]. The phase transitions are driven by varying the strength ε_{sf} of the interaction wall and fluid particles. Our set-up is particularly suited to study the partially wet (or dry) situation where $\varepsilon_d < \varepsilon_{sf} < \varepsilon_w$ with ε_d and ε_w the values of ε_{sf} where the drying and the wetting transition take place. In this situation of partial wetting and drying, the free energy favors one of the substrate sides to be covered by the liquid phase and the other by the vapor phase. Thus we have simultaneously realised a substrate-liquid, a substrate-vapor and a liquid-vapor interface and we can obtain their surface tensions γ_{sl}, γ_{sv} and γ_{lv} as integrals over pressure tensor components[12]. This situation is analoguous to a liquid droplet adsorbed at a substrate making a contact angle θ with the substrate. The simulation data are thus interpreted in terms of a contact angle through Young's relation[1]

$$\cos\theta = \frac{\gamma_{sv} - \gamma_{sl}}{\gamma_{lv}} \tag{1}$$

It turns out[11,12] that the difference $(\gamma_{sv} - \gamma_{sl})$ is obtained most accurately when the wall particles are frozen in at their lattice positions. So we use an inert wall representation, where the wall can be viewed as an external potential ϕ^{ext} acting on the fluid, in the present simulations. The results for $\cos\theta$ as a function of the ratio $\varepsilon_r = \varepsilon_{sf}/\varepsilon_{ff}$ are shown in fig. 2. The drying transition, i.e. the point ε_d where $\cos\theta = -1$, is difficult to locate while the wetting point ε_w is fairly accurately given by the $\cos\theta$ data. The reason is that $\cos\theta$ cuts the line $\cos\theta = 1$ at a steep angle while it joins the line $\cos\theta = -1$ much more smoothly. This is related to the nature of the phase transitions: $\cos\theta$ being essentially a free energy, the behaviour of its derivative with respect to ε_{sf} gives the order of the phase transition. On the basis of these $\cos\theta$ measurements, the wetting and drying transitions were estimated[12] at $\varepsilon_w = 0.62 \pm 0.01$ and $\varepsilon_d = 0.20 \pm 0.05$ respectively (with ε_w and ε_d expressed in units of ε_{ff}).

The key to a more accurate analysis is a direct evaluation of the derivative $\partial\gamma_{sf}/\partial\varepsilon_{sf}$. For an inert wall, the derivative is given by the simple expression

$$\frac{\partial\gamma_{sf}}{\partial\varepsilon_{sf}} = \frac{1}{L^2} \int_{-L/2}^{L/2} dx\, dy \int_0^{z_c} dz\; n(\vec{r})\, \frac{\phi^{ext}(\vec{r})}{\varepsilon_{sf}} \tag{2}$$

Here, $n(\vec{r})$ is the fluid density, L the box size and z_c the cut-off in the substrate-fluid interaction which is in our case $2.5\sigma_{sf}$ away from the outer layers of the wall. From (2) we see that only an accurate determination of the fluid density inside the potential of the

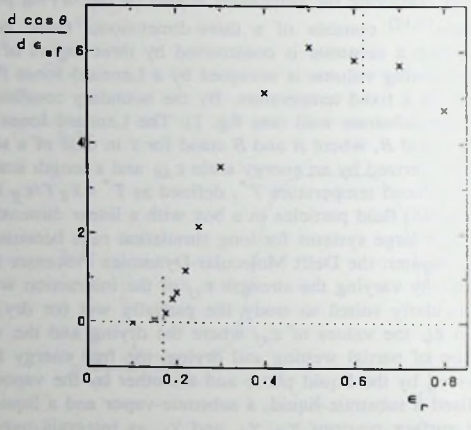

Fig. 3. The measured derivative of cos θ w.r.t. ε_{sf} as a function of ε_r. The error bars are of the order of the symbol size. The vertical dotted lines denote the positions of the drying and wetting transition.

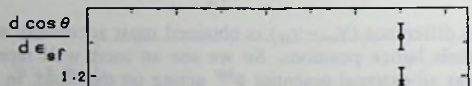

Fig. 4. The derivative of cos θ w.r.t. ε_{sf} as a function of ε_r around the drying transition. The crosses are the same points as in the previous figure, they are obtained by decreasing ε_r. The circles are obtained by increasing ε_r from $\varepsilon_r = 0.1$ onwards. If error bars are omitted, they are of the order of the symbol size. The two vertical dotted lines give the estimated bounds on the location of the drying transition.

substrate is necessary to find the derivative of γ_{sf}. The derivative of cosθ is obtained from Young's law. Equation (2) follows from a direct differentiation of the partition function[7)].

As already indicated in fig. 2, we simulated a series of partially wet (or dry) systems over a range of ε_r varying from 0.1 to 0.8. Typical runs involve 16,000 timesteps for equilibration and some 100,000 timesteps during which the system is sampled for accurate statistics. The longest simulation runs occurred around the drying transition where the fluctuations turned out to be large. Error bars in the data denote the standard deviation as calculated from subaverages over 400 configurations.

For $\varepsilon_{sf}<\varepsilon_d$, the liquid slab is pushed to the middle of the volume and both sides of the substrate are covered with vapor. For $\varepsilon_{sf}>\varepsilon_d$, the liquid slab is attracted to one of the sides of the substrate and this remains so even beyond $\varepsilon_{sf}=\varepsilon_w$ where it is more favorable that the liquid slab splits in two parts, both covering a side of the substrate with a vapor layer in between. Thus the partially wet state can be continued easily as a metastable state into the wet region (the reverse is also true for wet states in the partially wet region). These features can be recognized in fig. 3 in which the $\partial\cos\theta/\partial\varepsilon_{sf}$ data is plotted as a function of ε_{sf}. Whereas the derivative reaches a plateau near the wetting point ε_w, it drops sharply to zero near ε_d. This means that the drying transition is continuous while the wetting transition is first order. The data are compatible with a second order drying transition which is characterized by a behaviour of cosθ as

$$\cos\,\theta \;=\; -1 \;+\; c\;(\varepsilon_{sf}-\varepsilon_d)^2 \qquad\qquad \varepsilon_{sf} \geq \varepsilon_d \tag{3}$$

with c an arbitrary, positive constant. The consistency between the directly measured cosθ and the measurements of its derivative can be seen in fig. 2 which shows that the cosines can be reconstructed by integrating the $\partial\cos\theta/\partial\varepsilon_{sf}$ data with respect to ε_{sf}. To obtain an accurate integration, a cubic spline was fitted to the $\partial\cos\theta/\partial\varepsilon_{sf}$ data, which fit was then integrated from the point cosθ $=-1$ at $\varepsilon_r=0.1$ onwards. The so obtained wetting point $\varepsilon_w=0.62$ is the same as deduced from a directly measured cosθ plot.

The points in fig. 2 and 3 are obtained by decreasing ε_r. We also tested on the occurrence of hystheresis, which should not appear at a continuous transition, by increasing ε_{sf} from a completely dry system at $\varepsilon_r=0.10$ onwards. The two branches of $\partial\cos\theta/\partial\varepsilon_{sf}$ are shown in fig. 4 zooming in on the drying transition. The branch of increasing ε_r remains a little longer in the completely dry state, resulting in a difference in $\partial\cos\theta/\partial\varepsilon_{sf}$ of the increasing and decreasing branch at $\varepsilon_r=0.175$. The small differences at $\varepsilon_r=0.19$ and 0.22 seem not significant in view of the large fluctuations included in the averages. The fluctuations around the drying transition result primarily from small movements of the liquid slab. As the slab moves somewhat closer to the wall, the number of fluid particles in the first adsorbed layer increases significantly and $\partial\gamma_{sl}/\partial\varepsilon_{sf}$ drops while the opposite effect occurs when the slab moves a little bit further away from the wall. Compared with the fluctuations in the derivative of γ_{sl}, the derivative of γ_{sv} is virtually constant. We followed many of these systems till we had obtained 20 subaverages over 5200 timesteps but we sometimes also noticed an apparent correlation between 3 to 5 consecutive subaverages. The circles in fig. 4 give values of $\partial\cos\theta/\partial\varepsilon_{sf}$ which point at an ε_d=0.174 whereas the crosses point at ε_d=0.163 The total surface free energy of the two branches does not differ significantly, also not at $\varepsilon_r=0.175$, and therefore, we can not decide which of the two branches is thermodynamically most stable. Thus, the occurrence of two branches can hardly be viewed as representing a hystheresis loop indicative of a first order transition but we attribute it to the large and persistent fluctuations around the phase transition. On the contrary we see the large fluctuations in the partially dry state as precursor effects of the continuous drying transition. Our best estimate is therefore $\varepsilon_d = 0.169 \pm 0.005$.

We must pay some attention to the centre of mass motion, i.e. the "drift", that is generated in the system by the finite numerical accuracy of the molecular-dynamics calculation. As is customary in such simulations, the total momentum of the fluid is regularly set to zero (once every 5200 timesteps in our case) to prevent the drift from getting a chance to become too large and since almost all the fluid's mass is concentrated in the liquid slab, this most likely implies a slowing down of the slab's motion. Although we observed that the absence of any drift correction changes the motion of the liquid slab in systems around the drying transition, we could not detect a systematic feature in these differences.

So we conclude that, by an inspection of $\partial\cos\theta/\partial\varepsilon_{sf}$ instead of $\cos\theta$, we strongly improved the accuracy in the determination of both the order and location of the drying transition. Our simulations, treating large and rather realistic systems, show a surprising difference in character between the wetting and the drying transition. The simulations form an accurate reference for theoretical considerations, in particular for density functional calculations. The calculation of Velasco and Tarazona, tailored for the system we have studied, also gives a difference in character in the sense that the wetting transition is strongly and the drying transition only weakly first-order. So their density functional underestimates the continuous character of the drying transition. The comparison between a density functional calculation and a simulation is just the opposite in the van Swol and Henderson case: their calculation predicts a continuous drying transition whereas their simulations indicate it to be first-order. In spite of these discrepancies, density functional theories for both square-well and Lennard-Jones interactions thus show a tendency towards continuous drying transitions which our simulations support. The expectation of van Swol and Henderson that a fluid is not likely to change its structure smoothly from a substrate-liquid to a substrate-vapor profile at positions close to the substrate, is not born out by our simulations. The density profiles vary gradually from partially to completely dry as ε_{sf} is decreased towards the drying point. Whether the nature of the transition is sensitive to the details of the intermolecular interaction and differs for a square-well system on the one hand and a Lennard-Jones sytem on the other hand is still an open question.

References

1) for a review see e.g. S. Dietrich, in *Phase Transitions and Critical Phenomena*, edited by C. Domb and J. Lebowitz (Academic, London, 1988), Vol 12.
2) J.W. Cahn, J. Chem. Phys. **66,** 3667 (1977).
3) C. Ebner and W.F. Saam, Phys. Rev. Lett. **38,** 1486 (1977).
4) M.R. Moldover and J.W. Cahn, Science **207,** 1073 (1980).
5) C. Ebner, Phys. Rev. A **23,** 1925 (1981).
6) G. Langie and J.O. Indekeu, Phys. Rev. B **40,** 417 (1989).
7) F. van Swol and J.R. Henderson, Phys. Rev. A **40,** 2567 (1989).
8) A. Velasco and P. Tarazona, J. Chem. Phys. **91,** 7916 (1989).
9) F. van Swol and J.R. Henderson, Faraday Symp. Chem. Soc. **20,** 1 (1985).

10) J.H. Sikkenk, J.O. Indekeu, J.M.J. van Leeuwen, E.O. Vossnack and A.F. Bakker, J. Stat. Phys. **52,** 23 (1988).

11) M.J.P. Nijmeijer, C. Bruin, A.F. Bakker and J.M.J. van Leeuwen, chapter III of this thesis.

12) M.J.P. Nijmeijer, C. Bruin, A.F. Bakker and J.M.J. van Leeuwen, chapter IV of this thesis.

13) J. Finn and P.A. Monson, Phys. Rev. A **39,** 6402 (1989).

14) see the discussion in J. Chem. Soc. Faraday Trans. 2 **82,** 1828 (1986).

15) A.F. Bakker and C. Bruin, in *Special Purpose Computers,* edited by B.J. Alder (Academic, London, 1988).

CHAPTER VI

Wetting and drying of a wall with a long-ranged wall-fluid interaction

ABSTRACT

We have studied the influence of a long-ranged force between a wall and a fluid on the wetting properties of the wall-fluid system. The system with short range forces, i.e. cut-off Lennard-Jones potentials only, has been studied extensively in previous simulations, revealing the presence of a wetting and a drying transition. We have added the attractive tail of the wall-fluid potential to the simulations and reinspected these transitions. The wetting transition turns out to be not much affected by the long-ranged potential. The occurence of a completely dry wall is no longer expected but the tail appears to be too weak to observe the drying transition to vanish completely.

1. Introduction.

The intermolecular forces in simple fluids are long-ranged and their tails are usually described by attractive potentials which decay as $-1/r^6$ where r denotes the intermolecular distance. Although weak, this tail can have a significant influence on the properties of the fluid, especially near an interface. This has been demonstrated explicitly in a simulation[1)] of a "free" liquid-vapor interface which showed that an increase of the interaction range between the fluid particles drastically alters the properties of the coexisting liquid and vapor phase and of the interface between them. It must be expected that similar changes will appear at the interface between a fluid and a wall upon an increase of the interparticle interaction range[2)]. The influence of the tails of the potentials on a wall-fluid interface is of a special interest in the vicinity of a surface phase transition like the wetting or drying transition[3)]. Such transitions may be sensitive to small perturbations of the interaction potentials and although a quantitative estimate of the effect of the attractive tails is hard to give, simple mean field theories[4)] indeed predict them to have a dominant influence on the transitions.

The long-ranged fluid-fluid interactions play a subtle role in the properties of a wetting or a drying transition but the influence of the long-ranged wall-fluid interaction can be understood more easily. The attractive long-ranged tail will facilitate the occurence of a wetting transition while the drying transition is expected to disappear completely. Namely, in the absence of the tail, a liquid slab which is adsorbed at the wall can wander away freely when it detaches. So a vapor layer near the wall of arbitrary thickness is possible. In the presence of the tail, the slab will be attracted to the wall at all distances. The slab may be repelled from the wall by the short-ranged wall-fluid interactions but since it will no longer experience these if it is far enough from the wall, the attractive tail will always tend to keep the slab at a finite distance. So only a microscopically thin layer of vapor near the wall is possible and thus, the system can not be completely dry.

Simulations have difficulties in treating the long-ranged, attractive tails. An increase of the interaction range strongly increases the number of interactions that has to be evaluated in the calculation. The simulation is slowed down considerably, the number of interactions being proportional to $\sim r_c^3$ in three dimensions, where r_c is the interaction range. Furthermore, the boundary conditions, e.g. periodic boundaries, may lead to pathological interactions if the range gets larger than the system size. Therefore, the potentials used in simulations are usually either short-ranged by definition, e.g. hard-sphere potentials, or truncated. In the case of the Lennard-Jones potential, given by

$$\phi(r) = 4\,\varepsilon\,\{(\sigma/r)^{12} - (\sigma/r)^6\} \tag{1.1}$$

a cut-off length $r_c = 2.5\sigma$ is often used (σ is the length scale, ε the energy scale of the interaction).

This is the cut-off length used in a series of simulations[5,6,7)] which studied the wetting of a wall built of a lattice of solid particles. The simulations employed truncated Lennard-Jones potentials only. They differed in the way they treated the wall and measured the contact angles. The first simulation[5)] allowed the wall particles to oscillate around their lattice positions and, measuring the solid-fluid surface tensions, calculated the contact angles via Young's law. The second simulation[6)] also used a "live" wall but measured the contact angle visually. The measurement procedure of the first simulation was repeated in the last one[7)] apart from the treatment of the wall. The solid particles were fixed at their lattice positions now, thus forming an external potential instead of a thermodynamic phase. Starting from a completely dry wall and increasing ε_{sf}, the strength of the solid-fluid interaction, a drying and a wetting transition were observed in all the three simulations. It became apparent that the drying transition is weakly first or second order whereas the wetting transition exhibits a strongly first order character. These wetting properties may vary considerably when r_c grows larger. When all interaction ranges increase, the computing time goes up prohibitively. In this paper, we therefore allow only a larger wall-fluid interaction range. If the solid particles are fixed at their lattice positions, thus forming an inert wall, and the lattice structure is neglected at distances z larger than r_c from the wall, the influence of the wall beyond r_c is described by a structureless external potential. Such a relatively simple external potential can be added to the simulations without a dramatic increase of computing time and it is a step closer to the situation encountered in reality.

Since the last of the three previous simulations[7)] also used an inert wall and moreover, gave the most accurate results for the location and order of the wetting and drying transition, we use the same measurement procedure, while adding the long-ranged potential. The simulation follows a series of symmetric dry, asymmetric and symmetric wet configurations and measures the surface tension of the various interfaces in the system. The systems are studied at varying wall-fluid affinity whereas the temperature is kept fixed. From the behaviour of the density profiles, the total surface tension and the contact angles, calculated with Young's law, the occurrence of a wetting and a drying transition are inspected.

This paper is further arranged in the following way: section 2 describes the technicalities of the simulation; the influence of the long-ranged potential on the bulk phases and the interfaces is discussed in section 3; section 4 treats the effect of the limitation of the bulk phases and of the range of the wall-fluid potential; the location of a wetting and a drying transition is discussed in section 5 and finally, conclusions are drawn in section 6.

2. Description of the system.

The simulations are set up in the same way as before[7)] apart from the fact that a long-ranged potential has been added. We summarize the main features and refer to Nijmeijer *et al*[7)] for a more elaborate description. The fluid is enclosed in a three dimensional box with periodic boundary conditions in all directions. The wall is built from three layers of an FCC lattice, placed in the *x-y* plane. The interaction between fluid particles is of the Lennard-Jones 12-6 type, characterized by σ_{ff} and ε_{ff} and truncated at $2.5\sigma_{ff}$. The system contains 2904 solid particles and some 8500 fluid particles, the box has a length $L=29.1\sigma_{ff}$. The temperature is kept fixed at $T^* = k_B T/\varepsilon_{ff} = 0.9$ and the main parameter in the simulations is ε_r defined by $\varepsilon_r = \varepsilon_{sf}/\varepsilon_{ff}$. The simulations are carried out on the Delft Molecular Dynamics Processor (DMDP)[8)] which is specially designed for molecular dynamics calculations.

The external potential ϕ^{ext} which represents the solid-fluid interaction consists of two parts in these simulations:

$$\phi^{ext}(\vec{r}) = \phi^{ext}_{sr}(\vec{r}) + \phi^{ext}_{lr}(z) \tag{2.1}$$

with the short-ranged part as previously defined[7]:

$$\phi^{ext}_{sr}(\vec{r}) = \sum_{l} \phi_{sf}(|\vec{r} - \vec{d}_l|) \tag{2.2}$$

where ϕ_{sf} denotes the Lennard-Jones 12-6 interaction between a solid and a fluid particle which is truncated at $2.5\sigma_{sf}$ and the sum is over all solid particles, $\vec{d}_l$ being the lattice position of solid particle l. The lattice structure of the wall is neglected in the additional long-ranged potential ϕ^{ext}_{lr} which acts at distances larger than $2.5\sigma_{sf}$ away from the wall only. It is constructed by smearing out the wall particles homogeneously over the wall with density n_s, which equals for our FCC lattice $n_s = 1.05/\sigma^3_{ss}$ (this implies a reduced density $n^*_s = n_s\sigma^3_{ff} = 1.73$). The long-ranged potential thus becomes the Lennard-Jones 9-3 potential between a fluid particle and a half infinite solid continuum. The fluid is enclosed in the z-direction between the outer layers of the wall and is therefore attracted to one outer layer within a certain distance from it and to the other one in the remaining part of the box. If we place the origin $z = 0$ in the middle of the fluid between the outer layers of the wall such that z ranges from $-L/2$ to $L/2$ (as in figs.1 and 5), then we have for the long-ranged part of the potential

$$\phi^{ext}_{lr}(z) = \begin{cases} \phi^{L}_{lr}(z) & -\dfrac{L}{2} < z < z_m \\ \phi^{R}_{lr}(z) & z_m < z < \dfrac{L}{2} \end{cases} \tag{2.3}$$

with the turning point z_m chosen at $z_m = 0$ unless stated otherwise. The potential ϕ^{L}_{lr} acts on the left of the system and attracts the particles to the left outer layer

$$\phi^{L}_{lr}(z) = \begin{cases} 0 & -\dfrac{L}{2} < z < -z_l + 2.5\sigma_{sf} \\ \dfrac{2\pi}{3} n_s \sigma^3_{sf} \varepsilon_{sf} \left\{ \dfrac{2}{15} \left[\dfrac{\sigma_{sf}}{z + \frac{L}{2}} \right]^9 - \left[\dfrac{\sigma_{sf}}{z + \frac{L}{2}} \right]^3 \right\} & -z_l + 2.5\sigma_{sf} < z < z_m \end{cases} \tag{2.4}$$

where the outer layers are located at $z = -z_l$ and $z = z_l$ (with $z_l = 13.89\sigma_{ff}$ in our simulations). Note that the long-ranged part acts at distances larger than $2.5\sigma_{sf}$ away from the wall only. The potential ϕ^{R}_{lr} acts at the right of the system and attracts the fluid to the right outer layer but is furthermore defined analogously to ϕ^{L}_{lr}. The long ranged part of the external potential does not connect smoothly to the short ranged part but the mismatch is small[9] and can e.g. not be recognized in the density profiles. The update of the particle velocities that incorporates the long-ranged force, can not be done on the DMDP since this computer was not designed to handle such forces. The DMDP however, is connected to an array-processor on which the velocity update is performed and the pressure tensor (see below) is measured at the same time. By this construction, the long-ranged potential ϕ^{ext}_{lr} could not easily be applied each timestep. Instead, the fluid was subject to the long-ranged force each 13^{th} timestep with the force 13 times as large as it would be if it were applied each timestep.

The solid-fluid surface tensions γ_{sf} are measured in the same way as before$^{7)}$:

$$\gamma_{sf} = \frac{1}{L^2} \int_{-L/2}^{L/2} dx\, dy \int_0^{z_b} dz \, \{ \, p_N(z) - p_T(z) - n(\vec{r}) \, z \, \frac{\partial}{\partial z} \, \phi^{ext}(\vec{r}) \} \tag{2.5}$$

where the origin $z=0$ is placed at the middle wall-layer and the fluid is imagined to be at $z>0$; p_N denotes the component of the pressure tensor normal to the surface, p_T the tangential component, n stands for the local density of the fluid. In principle, the integration over z should range from 0 to ∞ but in the finite geometry of the box, the integral has to be truncated at a position z_b which is a position in the bulk of the fluid. In the absence of ϕ_{lr}^{ext}, the precise location of z_b does not matter since the integrand of (2.5) vanishes in the bulk fluid. Including however ϕ_{lr}^{ext}, the integrand vanishes only at $z_b=\infty$, even if the fluid is of a bulk character already at a finite distance from the wall, because ϕ_{lr}^{ext} itself vanishes only infinitely far away from the wall. The solid-fluid surface tension depends therefore on the choice of z_b. The effect of the truncation of the integral at z_b can be estimated if one assumes that the fluid is of a bulk character at distances from the wall larger than z_b, an assumption which is reasonable for our simulations. In that case, the difference $(p_N - p_T)$ vanishes and the local density is equal to the bulk density n_B of the fluid at $z>z_b$. Extending the integral over z to infinity, one then adds a correction $\Delta\gamma_{sf}$ to γ_{sf} given by

$$\Delta\gamma_{sf} = -n_B \frac{1}{L^2} \int_{-L/2}^{L/2} dx\, dy \int_{z_b}^{\infty} dz \, z \, \frac{\partial}{\partial z} \, \phi^{ext}(\vec{r}) \tag{2.6}$$

In the case of the Lennard-Jones 9-3 potential, the correction takes the explicit form (since z_b is always chosen further than $2.5\sigma_{sf}$ away from the outer wall layer so that ϕ^{ext} is given by ϕ_{lr}^{ext}):

$$\Delta\gamma_{sf} = -\pi \, n_s \sigma_{sf}^4 \, n_B \varepsilon_{sf} \left(\frac{\sigma_{sf}}{z_b} \right)^2 \tag{2.7}$$

in which we neglected the contribution of the term $\sim 1/(z+(L/2))^9$ in ϕ_{lr}^{ext}. It is noticed by comparing table 2 and 3 that the correction is usually small and of the order of the statistical error in γ_{sf}. In the case of e.g. γ_{sl}, it rises from approximately one third of the uncertainty in γ_{sl} at $\varepsilon_r=0.15$ to twice the uncertainty in γ_{sl} at $\varepsilon_r=0.7$.

3. The density profiles.

As starting configurations in the simulations we either used a configuration of our previous simulations$^{7)}$ with the same ε_r and applied the long-ranged potential to it or we took a configuration at different ε_r for which the external potential had been applied and then changed ε_r. Most systems were equilibrated in some 15,600 timesteps whereupon no systematic evolution in the potential energy, the density profile or the pressure tensor profile

ε_r	γ^*_{lv}	p^*	γ^*_{tot}
0.15	0.211(10)	0.0318(4)	0.52(2)
0.2	0.222(7)	0.0304(4)	0.49(1)
0.25	0.204(10)	0.0305(5)	0.45(1)
0.3	0.212(8)	0.0312(5)	0.39(1)
0.4	0.207(14)	0.0302(4)	0.23(1)
0.5	0.215(10)	0.0305(6)	0.04(1)
0.6	0.214(5)	0.0310(4)	–0.30(1)
0.7	0.214(11)	0.0308(3)	–0.63(1)

Table 1. Liquid-vapor surface tension, pressure and total surface tension in the asymmetric systems. All quantities are in reduced units. The figures between parentheses denote the uncertainty (one standard deviation) in the last one or two digits. The results at $\varepsilon_r=0.15$ are taken from the system obtained by decreasing ε_r from 0.2 to 0.15. Most results are obtained from an average over 32,000 configurations.

ε_r	γ^*_{sl}	γ^*_{sv}	$\cos\theta$
0.15	0.269(9)	0.0366(11)	–1.03(4)
0.2	0.238(8)	0.0290(5)	–0.93(4)
0.25	0.216(6)	0.0205(9)	–0.87(3)
0.3	0.159(8)	0.0140(7)	–0.65(4)
0.4	0.024(11)	–0.0129(18)	–0.16(4)
0.5	–0.145(11)	–0.0453(16)	0.44(5)
0.6	–0.403(9)	–0.1259(23)	1.23(4)
0.7	–0.653(13)	–0.2138(31)	1.95(7)

Table 2. Solid-liquid and solid-vapor surface tension and the cosine of the contact angle in the asymmetric systems. All quantities are in reduced units. The figures between parentheses denote the uncertainty (one standard deviation) in the last one or two digits. The results at $\varepsilon_r=0.15$ are taken from the system obtained by decreasing ε_r from 0.2 to 0.15. The reported γ^*_{sv} at $\varepsilon_r=0.6$ and 0.7 are the surface tensions of the metastable solid-vapor interfaces encountered in the asymmetric systems whereas one has $\gamma^*_{sv} = \gamma^*_{sl}+\gamma^*_{lv}$ in equilibrium since the wall is completely wet. The cos θ of this metastable branch are larger than 1. Most results are obtained from an average over 32,000 configurations.

was observed. After this equilibration, we sampled some 3200 configurations of each system to determine the particle density and pressure tensor profile where the configurations were sampled each 13^{th} timestep. Error bars in the data denote the standard deviation as calculated from subaverages over 400 configurations each. Figure 1 shows an asymmetric particle density profile at $\varepsilon_r=0.5$.

A first question is whether the bulk phases and the liquid-vapor interface are affected by the wall-fluid interaction or not. Compared with the previous case[7)], this question is now more stringent since the fluid moves in an external field everywhere. A first criterion for the bulk character of a phase is the presence of a homogeneous density. As previously[7)], the local density fluctuates around a mean value in the region where we locate the liquid and vapor phase (see fig.1). The size of these regions is approximately the same as previously[7)] and the mean density around which the local density fluctuates does not vary systematically with ε_r. Averaged over all ε_r, the liquid and vapor density are $n^*_l=0.6638\pm0.0004$

ε_r	$\gamma^*_{sl,t}$	$\gamma^*_{sv,t}$	$\cos\theta_t$
0.15	0.266	0.0366	−1.02
0.2	0.232	0.0280	−0.91
0.25	0.208	0.0192	−0.84
0.3	0.149	0.0124	−0.60
0.4	0.009	−0.0143	−0.10
0.5	−0.163	−0.0471	0.51
0.6	−0.422	−0.1275	1.31
0.7	−0.683	−0.2156	2.07

Table 3. Solid-liquid and solid-vapor surface tension and the cosine of the contact angle of the systems listed in table 2, with the tail correction added. The errors are the same as in the corresponding entries without the tail correction in table 2.

and $n^*_v = 0.0462 \pm 0.0004$ (with $n^* = n\sigma^3_{ff}$) which coincides with the values quoted previously[7]. A second criterion for the presence of a bulk phase is the vanishing of $\{p_N(\vec{r}) - p_T(\vec{r})\}$. Fig. 2 shows this difference Δp in the asymmetric system at $\varepsilon_r = 0.5$ from which it is seen that Δp vanishes in the liquid and vapor phase. The liquid-vapor surface tension γ_{lv}, defined as the integral of $\Delta p(z)$ over the liquid-vapor interface, is listed in table 1 for the asymmetric systems. It does not vary systematically with ε_r and $\gamma^*_{lv} = 0.213 \pm 0.002$ averaged over all ε_r. This is some 5% below the previous result[7] which could be an effect of the external field acting on the interface. Finally, we consider the pressure which is measured in the same way as before[7]. Its value in the various systems is listed in the tables 1 and 4 which again show no significant variation of p^* with ε_r. When averaged over all ε_r, it equals $p^* = 0.0309 \pm 0.0002$; it is the same as quoted previously[7]. Therefore, we conclude that also in the presence of the long-ranged external field it is possible to identify a liquid and vapor phase with properties which can not be distinguished from the field-free case. The interface between these phases may be more sensitive to the external field since its surface tension has slightly dropped.

The solid-fluid interfaces experience the presence of the long-ranged potential much stronger. The amount of particles adsorbed at the wall is increased by this potential as can be seen in the figs. 3 and 4 which show the coverage of the solid-vapor and solid-liquid interface for the systems[7] without and the systems discussed here with the long-ranged wall-fluid potential. The coverage Γ of a solid-fluid interface is defined as

$$\Gamma = \int_0^{z_b} dz \, (n(z) - n_B) \tag{3.1}$$

with $n(z)$ the density averaged over the x-y plane and n_B the density of the bulk fluid. The coverage depends on the location of the origin $z = 0$ which is chosen at the middle layer of the wall in our case.

In case of the solid-vapor interface (fig. 3), the difference in coverage between the two types of system grows with increasing ε_r, reflecting the growing stength of the attractive, long-ranged potential. The difference however, becomes significant only beyond $\varepsilon_r = 0.5$

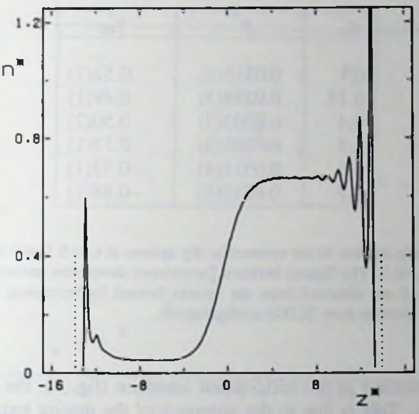

Fig. 1. Asymmetric density profile at ε_r = 0.5 obtained from an average over 4000 particle configurations generated in a run of 52,000 timesteps. The dotted lines denote the positions of the outer layers of the wall.

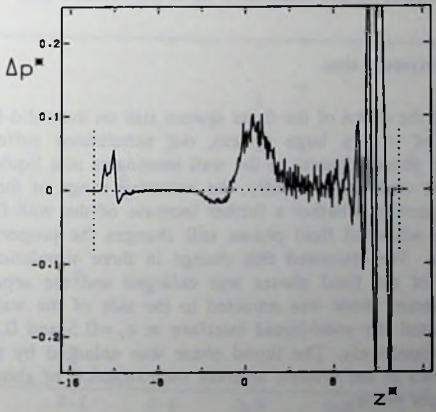

Fig. 2. Pressure difference profile $\Delta p^* = \Delta p \sigma_{ff}^3 / \varepsilon_{ff}$ at ε_r = 0.5, averaged over 26,000 timesteps.

which is already close to the wetting transition 7). Above the transition, the solid-vapor interface is metastable and a liquid layer should intrude between the wall and the vapor. The simulations give some indication of this intrusion since we observe a slow drift in the solid-vapor coverage towards larger coverages at $\varepsilon_r = 0.6$ and 0.7 in the system with a long-ranged potential. The same effect takes place at $\varepsilon_r = 0.8$ in the system with short-ranged interactions

ε_r	p^*	γ^*_{tot}
0.1	0.0315(3)	0.52(1)
0.15	0.0298(3)	0.49(1)
0.4	0.0303(3)	0.50(2)
0.5	0.0302(3)	0.13(1)
0.6	0.0311(4)	–0.32(1)
0.7	0.0316(5)	–0.88(1)

Table 4. Reduced total surface tension in the symmetric dry system at $\varepsilon_r=0.1$ and 0.15 and the symmetric wet systems from $\varepsilon_r=0.4$ till $\varepsilon_r=0.7$. The figures between parentheses denote the uncertainty in the last one or two digits. The results at $\varepsilon_r=0.15$ are obtained from the system formed by increasing ε_r from 0.1 to 0.15. Most results are obtained from an average over 32,000 configurations.

only.

The situation is reversed at the solid-liquid interface (fig. 4): the difference in coverage grows for decreasing ε_r. This is due to the approach of the drying transition. Near the transition, the liquid layer becomes weakly bound to the wall and is sensitive to small changes in the external field. At large ε_r, the liquid layer is tightly bound to the wall and the interface's structure is apparently determined by fluid-fluid and relatively strong wall-fluid interactions. The addition of a weak long-ranged interaction turns out to have little effect on the structure of the interface.

4. Effects of the finite system size.

We also inspected the effect of the finite system size on the solid-fluid interfaces. Compared with the limit of a very large system, our simulations suffer from two obvious shortcomings: the fluid phase adjacent to the wall terminates at a liquid-vapor interface at a finite distance from the wall and, secondly, the attractive range of the external potential is also finite. One can question whether a further increase of the wall-fluid interaction range and of the size of the adsorbed fluid phases still changes the properties of the solid-fluid interfaces significantly. We estimated this change in three simulations of an asymmetric system in which one of the fluid phases was enlarged and the separation point z_m was shifted such that the entire phase was attracted to the side of the wall it was adsorbed at. The simulations inspected the solid-liquid interface at $\varepsilon_r=0.5$ and 0.2 and the solid-vapor interface at $\varepsilon_r=0.6$ respectively. The liquid phase was enlarged by the insertion of about 1800 extra fluid particles in the system, whereas the extraction of about 3000 fluid particles resulted in a larger vapor phase.

The first of the simulations inspected the solid-liquid interface at $\varepsilon_r=0.5$. By the extra fluid particles, the midpoint of the liquid-vapor interface (where the local density $n(z)$ equals $(n_l+n_v)/2$) shifted from $z^*=-0.66$ to $z^*=-3.56$ (with the liquid phase adsorbed at the right hand side such as in fig. 1). The turning point z_m was replaced from the usual choice $z^*_m=0$ to $z^*_m=-10$. It turns out that the thus obtained density profile of the solid-liquid interface can not be distinguished from the profile of the previous case with the smaller liquid phase and $z^*_m=0$. The interface has a coverage $\Gamma^*=-0.910\pm0.012$ and a surface tension $\gamma^*_{sl}=-0.17\pm0.01$ which should be compared with the values $\Gamma^*=-0.918\pm0.006$ and

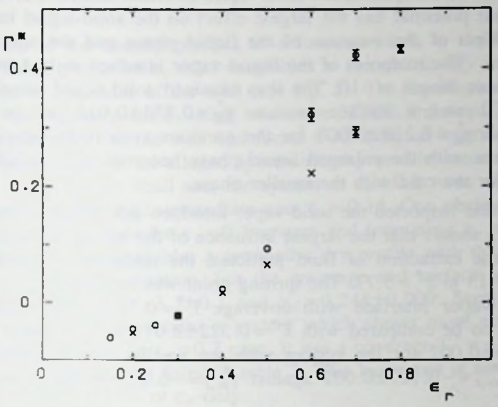

Fig. 3. Reduced coverage $\Gamma^* = \Gamma\sigma_{ff}^2$ for the solid-vapor interfaces as a function of ε_r. Crosses were obtained from the systems without a long-ranged wall-fluid potential7), circles are obtained in this work with the long-ranged potential. When the error bars are omitted, they are of the order of the symbol size.

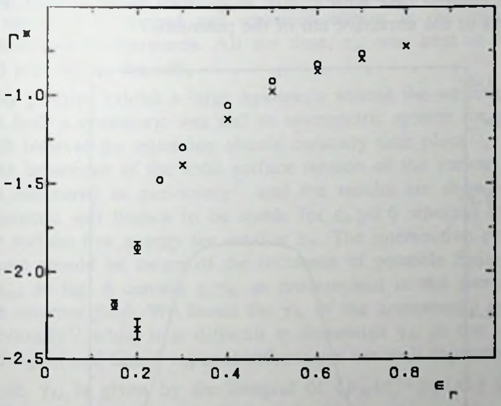

Fig. 4. Reduced coverage for the solid-liquid interfaces. Further as fig. 3.

$\gamma^*_{sl} = -0.14\pm0.01$ for the system with the smaller liquid phase. The comparison of the surface tensions becomes more fair if the tail correction (2.7) is added to make γ_{sl} less dependent on the choice of z_b. Including this correction, the comparison reads $\gamma^*_{sl,t} = -0.18\pm0.01$ for the enlarged system and $\gamma^*_{sl,t} = -0.16\pm0.01$ for the original one.

The second simulation inspected the solid-liquid interface at $\varepsilon_r = 0.2$. Fig. 4 shows that the tail of the external potential has the largest effect on the solid-liquid interface at low ε_r and therefore, the effect of the increase of the liquid phase and the shift of z_m could be larger than at $\varepsilon_r = 0.5$. The midpoint of the liquid-vapor interface shifted from $z^* = -2.44$ to $z^* = -5.08$ and z^*_m was chosen at -10. The thus obtained solid-liquid interface had a coverage $\Gamma^* = -1.81 \pm 0.02$ and a surface tension $\gamma^*_{sl} = 0.233 \pm 0.015$, to be compared with $\Gamma^* = -1.86 \pm 0.04$ and $\gamma^*_{sl} = 0.238 \pm 0.008$ for the previous system. Including the tail correction, γ_{sl} of the system with the enlarged liquid phase becomes $\gamma^*_{sl,t} = 0.226 \pm 0.015$ whereas $\gamma^*_{sl,t} = 0.230 \pm 0.008$ for the case with the smaller phase.

The last simulation inspected the solid-vapor interface at $\varepsilon_r = 0.6$. A rather large ε_r was chosen because fig. 3 shows that the largest influence of the tail on the solid-vapor interface is at high ε_r. By the extraction of fluid particles, the midpoint of liquid-vapor interface shifted from $z^* = -0.13$ to $z^* = 5.77$. The turning point was located at $z^*_m = 10$. We found in this system a solid-vapor interface with coverage $\Gamma^* = 0.314 \pm 0.006$ and surface tension $\gamma^*_{sv} = -0.126 \pm 0.002$, to be compared with $\Gamma^* = 0.322 \pm 0.011$ and precisely the same surface tension $\gamma^*_{sv} = -0.126 \pm 0.002$ for the system with the smaller vapor phase and $z^*_m = 0$. The comparison reads $\gamma^*_{sv,t} = -0.127 \pm 0.002$ against $\gamma^*_{sv,t} = -0.128 \pm 0.002$ when the tail corrections are included.

We therefore conclude that an increase of the fluid phase adjacent to the wall and a shift of z^*_m such that the entire phase is attracted to the side of the wall at which it is adsorbed, hardly affects the structure or surface tension of the solid-fluid interface. The increase of the range of the wall-fluid potential from $2.5\sigma_{ff}$, as in our previous simulation$^{7)}$, to $13.89\sigma_{ff}$, as in the present case with $z^*_m = 0$, away from the outer wall layer, should capture most of the effects of the attractive tail of the potential.

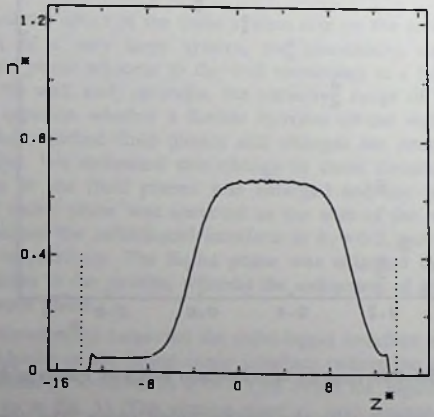

Fig. 5. Density profile at $\varepsilon_r = 0.1$, averaged over 2800 configurations generated in a run of 36,400, further as fig. 1.

5. The wetting and drying transition.

The behaviour of the density profiles as a function of ε_r is nearly the same as previously$^{7)}$. The density profile at $\varepsilon_r=0.1$ resembles a symmetric dry profile with the liquid phase close to one of the sides of the wall (see fig. 5). The liquid phase remained near this wall during the time we followed it which was some 52,000 timesteps. Increasing ε_r to 0.2, the liquid phase gets closer to the wall and forms a solid-liquid interface. The reverse transition, from an asymmetric to an alleged symmetric dry profile, occurs when ε_r is reduced from 0.2 to 0.1. Since, as we shall see, the system at $\varepsilon_r=0.2$ turns out to be still partially dry, we have also inspected the intermediate case $\varepsilon_r=0.15$. One observes some hysteresis at this value of ε_r. Starting from the $\varepsilon_r=0.1$ system and increasing ε_r to 0.15, one obtains a solid-liquid interface which resembles a symmetric dry profile with the liquid phase close to the wall just as the $\varepsilon_r=0.1$ situation. For the coverage and surface tension of this "solid-liquid" interface we find $\Gamma^*=-3.3\pm0.1$ and $\gamma^*_{sl}=0.248\pm0.009$. Starting from the $\varepsilon_r=0.2$ system and decreasing ε_r, one obtains a system which shows more convincingly a genuine solid-liquid interface, like in the $\varepsilon_r=0.2$ case. It has a coverage $\Gamma^*=-2.19\pm0.03$ and a surface tension $\gamma^*_{sl}=0.269\pm0.009$ as listed in table 2. This hysteresis is not observed at $\varepsilon_r=0.2$, it thus occurs in a limited range of ε_r only.

We did a separate test of the tendency of the liquid phase to remain near the wall at $\varepsilon_r=0.1$. Taking a particle configuration of a system like fig. 5 as starting configuration, we shifted the turning point z_m from $z^*_m=0$ to $z^*_m=10$. Thereby, the liquid phase was suddenly attracted to the other side of the wall, i.e. to the left-hand side in fig. 5. As a result, this phase started to travel towards the middle of the system but instead of travelling on to the other side of the wall, it stopped and remained almost in the middle during the 67,000 timesteps we followed it afterwards. All the time, z^*_m was kept at 10 so the entire liquid phase remained attracted to the left.

The density profiles exhibit a large hysteresis around the wetting transition. It is possible to maintain both a symmetric wet and an asymmetric system for all ε_r ranging from 0.4 to 0.7, in which interval the transition should certainly take place$^{7)}$. The transition appears clearly from the behaviour of the total surface tension of the various states. The total surface tension is measured as previously$^{7)}$ and the results are shown in fig. 6. The figure shows the symmetric wet branch to be stable for $\varepsilon_r\geq0.6$ whereas the asymmetric systems have the lower surface free energy for smaller ε_r. The intersection point locates the wetting transition but one should be aware of the influence of possible finite-size effects on it. For example, the γ_{tot} in fig. 6 contain a γ_{lv} as encountered in the simulations, which may be affected by the external field. We found the γ_{lv} of the asymmetric systems to be some 5% lower than previously$^{7)}$ while it is difficult to determine γ_{lv} in the symmetric wet systems where the solid-liquid and liquid-vapor interfaces are not well separated.

Furthermore, γ_{lv} is given by the integral of $\{p_N(z)-p_T(z)\}$ over the interface. We have defined the total surface tension γ_{tot} as the integral of $\{p_N(z)-p_T(z)-n(z)\,z\partial_z\phi^{ext}(\vec{r})\}$ over the entire system$^{7)}$. The contribution of the liquid-vapor interfaces contains therefore the extra term $n(z)\,z\partial_z\phi^{ext}(\vec{r})$, integrated over the interface. This contribution can be determined in the asymmetric systems where it is small, ranging from approximately -0.003 at $\varepsilon_r=0.1$ to -0.02 at $\varepsilon_r=0.7$ in the reduced units of fig. 6. The contribution appears twice in the symmetric systems since they contain two liquid-vapor interfaces and moreover, it is larger in these systems

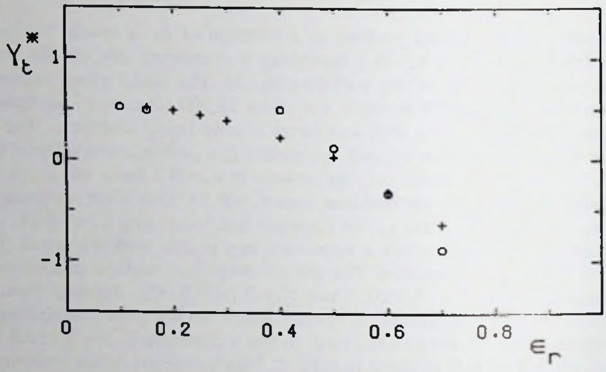

Fig. 6. Reduced total surface tension γ^*_{tot} as a function of ε_r. Circles denote the symmetric systems, crosses the asymmetric ones. The symmetric value at $\varepsilon_r=0.15$ is taken from the system formed by increasing ε_r from 0.1 to 0.15. The asymmetric value was measured in the system formed by decreasing ε_r from 0.2 to 0.15. The experimental uncertainty is of the order of the symbol size.

because these interfaces are closer to the wall. Like γ_{lv} however, the contribution is difficult to determine precisely in the symmetric wet systems. For the same reasons, the contribution of the term $n(z)z\partial_z\phi^{ext}(\vec{r})$ to γ_{sl} is different in the two types of system.

On the other hand, if one compares γ_{tot} as measured in the symmetric wet systems with a γ_{tot} calculated as $\gamma_{tot}=2\gamma_{sl}+2\gamma_{lv}$ with $\gamma^*_{lv}=0.225$ and γ_{sl} as measured in an asymmetric system, one notices that the difference between the two numbers is within or close to the errors in the measurement (except for the case $\varepsilon_r=0.4$). This shows that γ_{tot} obtained in our small sized, symmetric wet system is a reasonable representation of the total surface tension of a symmetric wet system with a well developed liquid phase. Thus, in spite of the objections mentioned above, the intersection point in fig. 6 appears to be a reasonable estimate of the location of the wetting transition. It is however, difficult to determine the transition accurately since the partially and the completely wet branches of the surface free energy are rather parallel and for this reason, the transition is also sensitive to small shifts of the branches. We will therefore rely on the contact angle measurements for a more accurate location of the wetting transition. The total surface tension does not show the presence of a drying transition but it varies smoothly with ε_r at low ε_r.

Finally, we have calculated the contact angles from Young's law with $\gamma^*_{lv}=0.225$. This value was also used in our previous work[7] and is closer to the result obtained at a free liquid-vapor interface[1] than the average γ_{lv} of these simulations. The cosines of the angle are shown in fig. 7 which reveals a first order wetting transition at $\varepsilon_w=0.57\pm0.02$. They locate a drying transition at $\varepsilon_d=0.15\pm0.05$. From this figure, it is difficult to tell whether a curve through the points intersects the line $\cos\theta=-1$ with a finite or with zero angle, i.e. whether the drying transition is weakly first or second order.

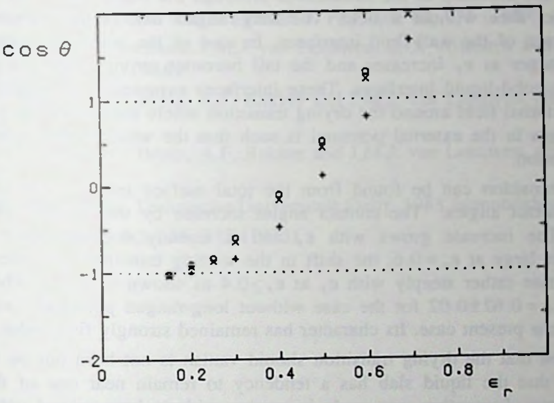

Fig. 7. Cosine of the contact angle versus ε_r. The crosses + are the results without the long-ranged wall-fluid potential[7]. The crosses × are obtained in this work, they shift to the circles O when the tail correction is applied. The error in the cosines is of the order of the symbol size, c.f. tables 2 and 3.

We have also calculated the contact angles from the "corrected" solid-fluid surface tensions, with $\gamma_{lv}^{*}=0.225$ as previously, to estimate the effect of the omitted part of the liquid-vapor interaction on the wetting and drying transition. As we discussed above, this estimate is reliable if the properties of the solid-fluid interface do not change significantly when the extent of the fluid phase and the range of the wall-fluid interface are increased and if the fluid is of a sufficient bulk character at $z>z_b$. These assumptions were found to be valid in the simulations. The "corrected" cosθ are shown in fig.7 and listed in table 3. They are larger than the "bare" results but the difference, growing linear with ε_r, becomes significant beyond $\varepsilon_r \approx 0.6$ only. The wetting transition shifts to $\varepsilon_w=0.56\pm0.02$, which is a marginal correction. The correction of cos θ a posteriori does not shift the alledged drying transition since the correction is still small at small ε_r.

6. Conclusions.

We have applied the long-ranged wall-fluid interaction to a system thoroughly studied in previous simulations. The effect of this interaction is especially interesting in connection with the presence of a wetting and drying transition which were shown to be present in the system with short-ranged forces only. It is expected that the long-ranged force facilitates the wetting and prevents a drying transition. We could increase the range of the wall-fluid interaction from $2.5\sigma_{ff}$ to $13.89\sigma_{ff}$ away from the outer layer of the wall. The potential was treated in an approximate way: it was taken to be a Lennard-Jones 9-3 potential from $2.5\sigma_{ff}$ away from the wall onwards and applied each 13th instead of each timestep but it can reasonably be assumed that these approximations have little effect on the solid-fluid interface.

The long-ranged part is so weak that the bulk character of the liquid and vapor phase is not affected within the accuracy of the simulations although the liquid-vapor surface tension is somewhat smaller than without a field. The long-ranged tail, being attractive, clearly increases the coverage of the wall-fluid interfaces. In case of the solid-vapor interface, the increase becomes larger as ε_r increases and the tail becomes stronger but the situation is more subtle for the solid-liquid interfaces. These interfaces experience the largest influence of the tail of the external field around the drying transition where the sensitivity of the interface to small changes in the external potential is such that the weak attractive tail strongly increases the adsorption.

The wetting transition can be found from the total surface tensions and, more accurately, from the contact angles. The contact angles increase by the addition of the long-ranged potential. The increase grows with ε_r and is already noticable at $\varepsilon_r=0.2$ but although it becomes large at $\varepsilon_r=0.6$, the shift in the wetting transition is modest. This is because the cos θ rise rather steeply with ε_r at $\varepsilon_r \geq 0.4$ as shown in fig. 7. The transition was estimated at $\varepsilon_w=0.62\pm0.02$ for the case without long-ranged potential[7] and shifts to $\varepsilon_w=0.57\pm0.02$ in the present case. Its character has remained strongly first order.

Our expectation that the drying transition should vanish is not born out by the simulations. We observe that the liquid slab has a tendency to remain near one of the walls at $\varepsilon_r=0.1$ but the same observation was made in system without long-ranged potential. In a simulation at $\varepsilon_r=0.1$, it was observed that the slab moves away from the wall when it is attracted to the opposite side of the box by the long-ranged potential. This supports the idea that the slab is bound to the wall by this potential. On the other hand, the liquid slab did not move to the opposite side of the wall but remained in the middle as if, on the contrary, the attractive tail is not strong enough to bind the slab to the wall. The observed hysteresis at $\varepsilon_r=0.15$ pleads for the presence of a phase transition and the contact angles become, within the accuracy of the simulations, also equal to π. We thus conclude that the long-ranged tail becomes so weak at $\varepsilon_r \leq 0.15$ that the slab's character of a bound state can not be observed in the simulations. Instead, they seem to locate a drying transition at $\varepsilon_d=0.15\pm0.05$, to be compared with the estimate[7] of genuine transition at $\varepsilon_d=0.20\pm0.05$.

We have checked the dependence of coverages and surface tensions on the size of the bulk phases and the cut-off of the long-ranged potential. Three simulations in which one of the fluid phases adjacent to the wall was increased and z_m was shifted such that the entire phase was attracted to the side of the wall it was adsorbed at, showed no significant variation of the properties of the wall-fluid interface. Therefore, we expect no considerable changes in the wetting transition in a system with fully extended fluid phases and wall-fluid potentials. Since the theoretical evidence for the vanishing of the drying transition seems inescapable, one would nevertheless expect that a much larger system and much longer simulation times demonstrate the alledged disappearance of the drying transition more clearly. Such simulations could be capable to observe the slab's character of a bound state even at very low ε_r.

References

1) M.J.P. Nijmeijer, A.F. Bakker, C. Bruin and J.H. Sikkenk, chapter VIII of this thesis.

2) M.P. Nightingale and J.O. Indekeu, Phys. Rev. B **32**, 3364 (1985).

3) for a review see e.g. S. Dietrich, in *Phase Transitions and Critical Phenomena*, edited

by C. Domb and J. Lebowitz (Academic, London, 1988), Vol 12.

4) E. Brézin, B.I. Halperin and S. Leibler, J. Physique **44**, 775 (1983).

5) J.H. Sikkenk, J.O. Indekeu, J.M.J. van Leeuwen, E.O. Vossnack and A.F. Bakker, J. Stat. Phys. **52**, 23 (1988).

6) M.J.P. Nijmeijer, C. Bruin, A.F. Bakker and J.M.J. van Leeuwen, chapter III of this thesis.

7) M.J.P. Nijmeijer, C. Bruin, A.F. Bakker and J.M.J. van Leeuwen, chapter IV of this thesis.

8) A.F. Bakker, thesis, Technische Universiteit Delft, 1983 (unpublished).

9) W.A. Steele, Surf. Sci. **36**, 317 (1973).

CHAPTER VII

A search for prewetting

ABSTRACT

A first-order wetting transition should be accompanied by a prewetting transition. Although many of such transitions have been reported, clear observations of prewetting are rare. We report on a search for prewetting in a wall-fluid system which was shown previously to exhibit a first-order wetting transition. The fluid consists of a vapor phase which density is increased towards the coexistence density while the coverage of the wall-vapor interface is monitored. This approach of coexistence is studied as a function of the interaction strength between the wall and the fluid. Although we do recognize the presence of a wetting transition in the adsorption curves, the more subtle effects associated with prewetting cannot unambiguously be observed.

1. Introduction.

Wetting, as a branch of adsorption phenomena, has enjoyed an active interest in recent years[1]. Generally, wetting phenomena occur when two thermodynamic phases compete to be adsorbed at a third phase. A model system to describe these phenomena is that of a fluid at liquid-vapor coexistence in contact with a wall. This model displays a particular form of wetting when the coverage of the substrate is considered as a function of the affinity of the wetting fluid to the substrate which is measured by the interaction strength ε. If the wall is covered by the vapor phase at a low affinity, a liquid layer will form at the solid-vapor interface when ε is increased. The formation of a liquid phase at the substrate may occur via a continuous or a first-order phase transition. In the continuous case, the wetting layer grows from microscopic (or finite) at low values of ε to macroscopic (or infinite) at the wetting point ε_w. When the wetting transition is first-order, the coverage jumps at ε_w from microscopic to macroscopic.

Such a first-order wetting transition is accompanied by a prewetting transition in the undersaturated vapor regime. If the adsorbed vapor is not in coexistence with its liquid, never a macroscopically thick liquid layer can be formed on the substrate but only a microscopically thin layer. Close to saturation there will be a transition from a thin to a thick coverage upon increasing ε.

The phase diagram of prewetting is sketched in fig. 1 in terms of the parameter $\Delta\mu$, controlling the distance of the fluid from liquid-vapor coexistence with the undersaturated vapor at $\Delta\mu<0$, and ε, the affinity of the fluid to the wall. The prewetting line starts at $\Delta\mu=0$ (liquid-vapor coexistence) and $\varepsilon=\varepsilon_w$ and terminates in a critical point at $\Delta\mu=\Delta\mu_{cpw}$ and $\varepsilon=\varepsilon_{cpw}$. The nature of a prewetting line is quite similar to the liquid-vapor coexistence line in a bulk fluid. This is born out when we plot the coverage Γ as a function of the vapor density (see fig. 2). Lines of equal ε show a behaviour similar to the isotherms in an ordinary phase diagram of liquid-vapor coexistence. For large ε, (high temperature isotherms) the coverage Γ increases continuously from a finite value to infinity at the saturated vapor density n_c. For $\varepsilon_w<\varepsilon<\varepsilon_{cpw}$, the coverage jumps from thin to thick at a vapor density n between the prewetting critical density n_{cpw} and the saturated density n_c. The jump increases to infinity and moves to n_c when ε reaches ε_w. For $\varepsilon<\varepsilon_w$ the coverage rises with n to a finite value at n_c.

The interest in prewetting is amongst others triggered by the fact that it is a genuine two-dimensional realisation of a first-order transition ending in a critical point and thus one believes the prewetting critical point to be in the universality class of the $d=2$ Ising model[2]. The prewetting phenomenon is however difficult to observe. This may have to do with the two-dimensional character of the system where critical fluctuations are large and consequently the prewetting line short. In our language this means that n_{cpw} is close to n_c and ε_{cpw} close to ε_w. Moreover, the prewetting line can be shown to merge tangentially with the liquid-vapor coexistence line[3]. Prewetting was predicted together with the wetting transition[4]. Its existence is supported by density functional calculations[5,6] and also many lattice gas models[2,7,8] can be shown to demonstrate the prewetting transition.

Recently, a prewetting line was scanned in a simulation of a Lennard-Jones 12-6 fluid in contact with a wall by Finn and Monson[9]. The wall was taken to be a half-infinite, smeared-out Lennard-Jones wall and thus was represented by the Lennard-Jones 9-3 potential. They studied the adsorption at the wall as a function of the fluid's pressure and

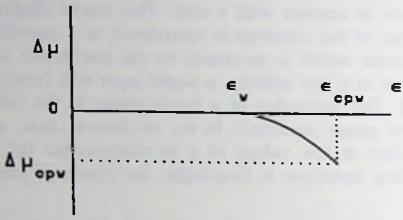

Fig. 1. Schematic wetting phase diagram at a fixed temperature. The attractive wall-fluid strength is measured by ε: a larger ε denotes a stronger attraction; $\Delta\mu$ denotes the difference between the chemical potential μ and its value at liquid-vapor coexistence μ_c. The unsaturated vapor phase is located at $\Delta\mu<0$. The line that deviates from the coexistence line $\Delta\mu=0$ is the prewetting line. It ends in a critical point at ε_{cpw} and $\Delta\mu_{cpw}$.

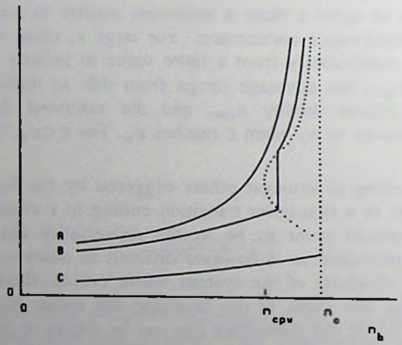

Fig. 2. Prewetting phase diagram at a fixed temperature. Γ denotes the coverage of the wall-vapor interface, n_b the bulk vapor density; n_c is the saturated vapor density and n_{cpw} the density at the prewetting critical point. The curve A is a typical adsorption curve for $\varepsilon>\varepsilon_{cpw}$, curve B is at $\varepsilon_{cpw}<\varepsilon<\varepsilon_w$ and C at $\varepsilon<\varepsilon_w$.

temperature instead of the fluid's density and the wall-fluid affinity but this difference should not change the qualitative nature of the phase diagrams of fig. 1 and 2. The simulation showed jumps in the coverage that neatly behave according to the phase diagram of fig. 2 (with ε replaced by the temperature) and thus forms a convincing observation of prewetting. Any experimental report of prewetting still seems to lack although several prewetting-like phenomena have been observed[10,11)].

In the present paper, we report on a search for the prewetting phenomenon in molecular-dynamics simulations of a previously studied wall-fluid system[12,13,14)]. These simulations have examined the system with the fluid at liquid-vapor coexistence as a function of the wall-fluid affinity ε. They revealed the presence of a strongly first-order wetting transition, so this system seems a good candidate for the observation of prewetting. Moreover, the location of both the wetting transition ε_w and the saturated vapor density n_c are known rather accurately so the main prerequisites for a directed search are fulfilled. The paper is organized in the following way. Section 2 describes the measurement procedure and the technicalities of the simulation, the results are presented in section 3 and the paper is closed with a discussion in section 4.

2. Description of the system.

The system encountered in these simulations is almost the same as the one studied by Sikkenk *et al*[12)]. We recall its main features but refer to Sikkenk *et al* for an elaborate description. The system consists of a three dimensional, cubic box in which a wall and a fluid are contained. The box has periodic boundary conditions in all directions. The particles interact via a Lennard-Jones 12-6 potential ϕ_{AB}

$$\phi_{AB}(r) = 4\varepsilon_{AB} \, \{ \, (\sigma_{AB}/r)^{12} - (\sigma_{AB}/r)^{6} \} \tag{2.1}$$

where A and B denote the type of the two interacting particles, i.e. they stand for either s in case of a solid or f in case of a fluid particle. The interparticle distance is r, ε_{AB} denotes the energy scale and σ_{AB} the length scale of the A-B interaction. The potentials are truncated at $2.5\sigma_{AB}$. The reduced boxlength $L^* = L/\sigma_{ff}$ is $L^* = 29.1$, the reduced temperature $T^* = k_B T/\varepsilon_{ff}$ is kept fixed at $T^* = 0.9$. The simulations are carried out on a special purpose computer: the Delft Molecular Dynamics Processor[15)] (DMDP).

The wall is built of three layers of an FCC-lattice which require 2904 wall particles. The wall particles are strongly interacting, $\varepsilon_{ss} = 50\varepsilon_{ff}$, and have a larger mass than the fluid particles: $m_s = 3m_f$. This choice of parameters guarantees a stable wall, i.e. the lattice positions around which the wall particles oscillate, remain in place during the simulations. The wall layers are placed in the x-y plane and the fluid is in contact with both outer layers due to the periodic boundaries.

The difference with the previous work[12)] is that the number of fluid particles N_f is varied in these simulations to control the vapor density. The second parameter in the simulations is the interaction strength ε_{sf} between the wall and the fluid particles. It is expressed as the ratio $\varepsilon_r = \varepsilon_{sf}/\varepsilon_{ff}$ which we see as a measure for the affinity of the fluid for the substrate wall. The coverage Γ is measured as a function of these two parameters via

$$\Gamma = \frac{1}{L^2} \int_{-L/2}^{L/2} dx \, dy \int_{0}^{z_b} dz \, (\, n(\vec{r}) - n_b) \tag{2.2}$$

with z_b a sufficiently deep position in the bulk vapor, $n(\vec{r})$ the density of the fluid at position $\vec{r}$ and n_b the density in the bulk vapor. The fluid is taken to be located at $z>0$. The bulk vapor density n_b is measured directly in the system. The coverage depends on the location of the origin $z=0$ which we chose to place at the middle wall layer. Note that we cannot fix n_b directly using the number of fluid particles as our control parameter but only the sum

$$N_f = L^3 \; n_b + L^2 \; (\Gamma_l + \Gamma_r) \tag{2.3}$$

where Γ_l denotes the coverage of one of the sides of the wall, say the left one, and Γ_r the coverage of the other side. Particles are added to or subtracted from the region of the box where the fluid has bulk vapor properties.

Gradually changing the amount of fluid particles at a fixed value of ε_r, we expect to observe a prewetting transition as follows. Starting with a system with ε_r below the wetting threshold ε_w and a low density vapor, we add particles so the vapor density and the coverage at both sides of the wall gradually increases. The coverage should be the same at both sides of the wall at all vapor densities and it should still be finite at coexistence, as indicated in fig 2. When the saturation density has been reached and one continues to add particles, a liquid layer should grow at one of the sides of the wall, forming a partially wet system in which one side is covered with liquid, the other with vapor$^{12)}$.

This growth behaviour should be different for ε_r between ε_w and ε_{cpw}. In that case, one expects the density and the coverage to grow with the addition of fluid particles until the density at which the prewetting transition takes place, has been reached. Till that moment, the coverage should be the same at both sides of the wall. From that moment on, the added particles are used to form a thick film at one of the sides of the wall. The area covered with the thick film forms an "island" on the wall which borders at the area covered by the thin film along a contact line. The line tension of this contact line will minimize the total length of the line and therefore, all of the thick film should ideally be present in one island. The average coverage of the side of the wall at which the thick film has formed, grows as the size of this island increases by the addition of fluid particles. The average coverage of the other side of the wall should not change since this side should be covered entirely with the thin film. Thus, there appears a difference in the coverage at the two sides which reaches a maximum when one side has become covered entirely with the thick film while the other side is still completely covered with the thin film. From that moment on, the difference decreases because the thick film is also formed at the other side and finally, it vanishes when both sides of the wall are covered with the thick film. Continuing to add particles, one has passed the prewetting transition and the vapor density increases again while the coverage grows with the same rate at both sides of the wall. The coverage diverges as coexistence is approached since a liquid layer is formed at both walls for ε_r above ε_w.

The growth behaviour is again much simpler for $\varepsilon_r > \varepsilon_{cpw}$. In that case, one does not pass a prewetting transition and both the vapor density and the coverage should grow continuously under the addition of fluid particles. The coverage should remain the same at both walls and diverge at the approach of the saturation density.

Thus we expect the presence of a prewetting transition to be signaled by two main characteristics: a difference in the coverage at the two sides of the wall and, secondly, no change in the vapor density under the addition or subtraction of fluid particles but only a change in the coverage at one of the sides of the wall.

In some cases, we also measured the surface tension of the wall-vapor interface. The measurement of the surface tensions is a delicate problem. In principle, the wall with wall particles that are free to move, represents a thermodynamic phase and the surface tension should be measured in a way appropriate to an interface between two thermodynamic phases. This was the way originally employed[12)] in the wall-fluid surface tension measurements. It was however suggested[16)] that the thickness of only 3 layers and the possibility of the wall to support stress, caused the thus obtained surface tensions to be unreliable. This suggestion was confirmed by two subsequent simulations[13,14)]. In the last of these[14)], the wall particles were frozen in at the lattice positions and, consequently, the surface tension was measured in a way appropriate to the interface of a fluid in an external potential. These measurements turned out to give far more reliable results.

In these prewetting simulations, we again employ a "live" wall but do however, not measure the surface tensions as they should be measured formally since this way has proven to be too inaccurate. Instead, we treat the fluid as moving in an external field and measure the wall-vapor surface tension accordingly. Such a measurement[14)] probes only the state of the fluid and neglects the contribution of the solid-solid interactions to the surface tension γ. These interactions probably dominate γ but, since we are only interested in differences in surface tension, we can neglect them if we assume that the solid-solid contributions to γ are the same for the interfaces that are compared. In view of the success of the measurements at a fixed wall and the observation that the effect of the oscillations of the wall particles on the adsorbed fluid is small, we expect that it is indeed sufficient to evaluate only the state of the fluid to compare solid-vapor surface tensions. The original expression for the wall-vapor surface tension of a fixed wall is averaged over the degrees of freedom of the wall particles when it is applied to the live wall case:

$$\gamma = \frac{1}{L^2} \int_{-L/2}^{L/2} dx\, dy \int_0^{z_b} dz < p_N(\vec{r}) - p_T(\vec{r}) - n(\vec{r})\, z \frac{\partial}{\partial z} \phi^{ext}(\vec{r}) > \tag{2.3}$$

with p_N and p_T the components of the fluid's pressure tensor normal c.q. tangential to the wall. The origin $z=0$ is placed at the middle wall layer and the average $< >$ denotes the ensemble average over the positions of the wall particles. The quantities p_N, p_T, n and ϕ^{ext} depend also on the configuration of the wall but this dependence has been suppressed in the notation of (2.3). A description of the measurement of p_N and p_T can be found in a previous paper[14)]. The definition of ϕ^{ext} has been described there as well, apart from the fact that the positions of the wall particles are no longer fixed at lattice positions:

$$\phi^{ext}(\vec{r}; \vec{r}_1, \ldots, \vec{r}_{N_s}) = \sum_{i=1}^{N_s} \phi_{sf}(|\vec{r} - \vec{r}_i|) \tag{2.4}$$

where $\vec{r}_i$ denotes the position of the i-th wall particle and N_s the number of wall particles ($N_s = 2904$ in our case).

An accurate knowledge of the location of the wetting transition is of great help in the investigation of the prewetting transition. The wetting transition was located in the three previous simulations[12,13,14)] which differed apart from the treatment of the wall in the measurement of the "contact angles". The first of these measured the contact angles via Young's

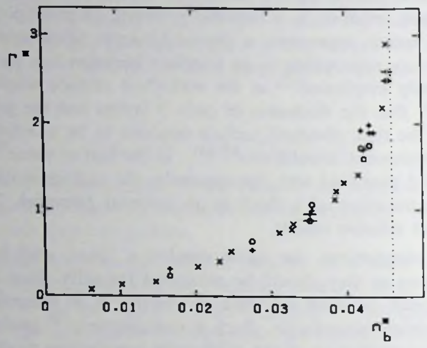

Fig. 3. Adsorption curve at $\varepsilon_r = 0.85$; Γ^* denotes the reduced coverage $\Gamma^* = \Gamma\sigma_{ff}^2$, n_b^* the reduced bulk vapor density $n_b^* = n_b\sigma_{ff}^3$. The dotted line marks the reduced saturation density $n_c^* = 0.046$. The coverage of the left and right-hand side of the wall are plotted separately, the left-hand side by a circle O, the right-hand side by a cross +, both at the same value of n_b. However, if they cannot be distinguished, both are plotted as one cross ×. The error in the coverages is of the order of the symbol size. The error in the vapor density is given by a horizontal bar through the symbols but is omitted if the error is of the order of the symbol size.

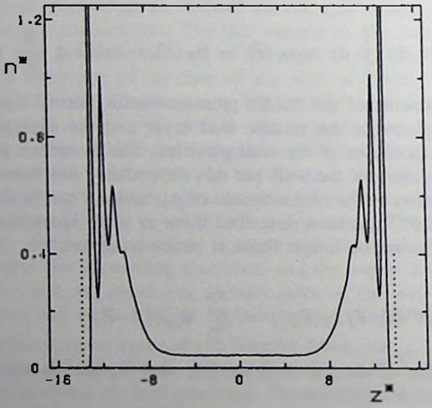

Fig. 4. Density profile at $\varepsilon_r = 0.85$ obtained as an average over 2000 configurations. The two wall-vapor interfaces are the interfaces with the left-hand and the right-hand side of the wall. The dotted lines give the positions of the outer wall layers. The reduced vapor density of this system is equal to 0.044.

law, the second series of simulations measured the angles visually whereas the last series used again Young's law. The first simulations gave a wetting transition at $\varepsilon_w = 0.78 \pm 0.03$ but this value has turned out to be not so accurate because of the difficulties in obtaining the wall-fluid surface tensions. The second and third series of simulations gave $\varepsilon_w = 0.68 \pm 0.03$ and $\varepsilon_w = 0.62 \pm 0.01$ respectively, which results agree rather well. The difference between them could be due to the difference in the representation of the wall and the fact that curved liquid-vapor interfaces were employed in the second simulation whereas planar interfaces were used in the last one. We thus know the wetting transition to be in the range between $\varepsilon_r \simeq 0.62$ and $\varepsilon_r \simeq 0.68$. All the three simulations agree on a value of the saturation vapor density $n_c^* = 0.046 \pm 0.0005$ at the temperature $T^* = 0.9$.

3. Results

The most complete adsorption curve was obtained for $\varepsilon_r = 0.85$. It is shown in fig. 3. A typical density profile from which the coverages and the bulk density are obtained is shown in fig. 4. For this ε_r, the number of fluid particles varies between 271 for the systems with the lowest vapor density and 6034 for the system with the largest density and coverages. Almost all points in this curve are formed by the addition of fluid particles but in general, points are either obtained by the addition or subtraction of fluid particles or they origin from a previous system with the same number of particles but a different ε_r. In all cases, an equilibration time was taken into account after the formation of a new system before the actual measurements started. The equilibration time is taken as long as necessary to obtain stable density profiles which can vary between 2000 and 78,000 timesteps. The length of the actual measurement time also varies, depending on the size of the fluctuations and the desired accuracy of the results. A measurement takes at least 26,000 timesteps but it may become up to eight times as long. Such long simulations are typically run for systems close to coexistence where the fluctuations are large and indications of prewetting are to be expected. The density and pressure tensor profiles are sampled every 13^{th} timestep. Error bars in the data denote the standard deviation calculated from subaverages over 5200 timesteps each.

The case $\varepsilon_r = 0.85$ was expected to be well above the wetting transition and this is confirmed by fig. 3 in which the coverage diverges as coexistence is approached. The dotted line is at the saturation density $n_c^* = 0.046$. The coverages at the left-hand and right-hand side of the system are usually equal although small but significant differences appear at various densities, especially around $n_b^* \simeq 0.043$. We do however not believe them to be related to prewetting, as will become clear later on. The fluctuations in the systems close to equilibrium are huge. The subaverages of the density may spread over a range larger than 0.01 in those systems.

A very different adsorption curve is obtained at $\varepsilon_r = 0.65$, as shown in fig. 5. These points are all obtained by decreasing ε_r in a previous system at $\varepsilon_r = 0.70$ except for the system with the lowest density which was made by subtracting particles from the next system with higher density. The curve is far less complete than fig. 3 but it shows that the coverage seems not to diverge near coexistence, i.e. the system is partially wet. Note that the figure shows one bulk density that is clearly above the coexistence density. The subaverages of this result show densities that range from below the coexistence density to values larger than 0.05 and it is very hard to tell when equilibrium has been achieved. Apparently, the equilibrium state is not reached at the timescale of the simulations (the system has been followed

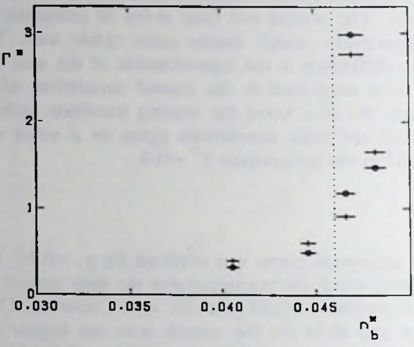

Fig. 5. Adsorption curve at $\varepsilon_r=0.65$, further as fig. 3.

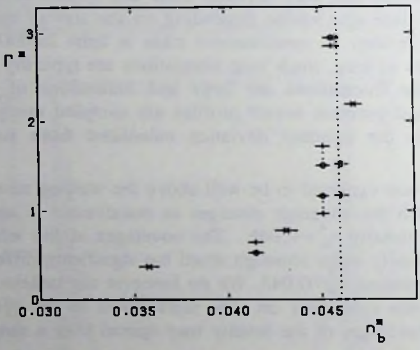

Fig. 6. Adsorption curve at $\varepsilon_r=0.70$, further as fig. 3. The two pairs of coverage at $n_b^*=0.045$ are distinguished from each other by the dotted lines which connect the corresponding coverages at the left and right-hand side of the wall.

for 130,000 timesteps). If the system is partially wet, it should form a liquid phase at one of the sides of the wall from the moment coexistence has been reached while it maintains a solid-vapor interface at the other side. This does not occur: the coverages of the left-hand and the right-hand side both increase and the system remains approximately symmetric. On

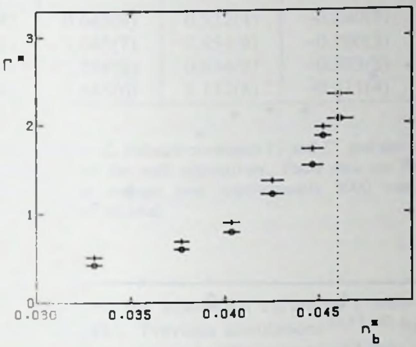

Fig. 7. Adsorption curve at $\varepsilon_r = 0.75$, further as fig. 3.

the other hand, we verified that if one startes with an asymmetric system at coexistence with a difference in coverage $\Delta\Gamma^* = 1$, this difference turns out to be stable as well. Extracting particles from the vapor phase then, the coverage decreases at both walls while the system remains at coexistence although the successive differences in coverage become smaller.

The adsorption curve at $\varepsilon_r = 0.70$ is given in fig. 6. Some of the points in this figure are obtained by changing the amount of particles in a previous system at the same ε_r, some are obtained by changing ε_r while leaving the amount of particles unaltered. The curve is less conclusive as to whether we have passed the wetting transition or not: it shows a steep rise in coverage of which it is hard to determine whether it occurs at or just before coexistence. The two systems just before coexistence and the one next to them at coexistence have been followed for 208,000 timesteps after the equilibration time, which is longer than any other system. We wanted to locate these points so accurately because the occurence of such a rise at a density lower than the saturation density would imply the presence of a prewetting transition. The points however, are too close to the coexistence line to interprete them as a clear prewetting phenomenon.

At ε_r equal to 0.75, the adsorption curve of fig. 7 is obtained. As in the previous figure, some of the systems are obtained by changing ε_r while others result from a change in the amount of fluid particles. This curve looks like the adsorption curve at $\varepsilon_r = 0.85$: a gradually diverging coverage, characteristic for a completely wet wall. Little differences in the coverage at the left and the right-hand side of the wall appear at various densities. We have also measured the adsorption curves at ε_r equal to 0.80 and 0.90 and found them to be qualitatively the same as the curves at ε_r equal to 0.75 and 0.85.

We expected the appearence of asymmetric coverages to be a sign of prewetting but this turns out to be an unreliable criterion: significant differences in coverage appear in many cases. This implies that one is easily trapped in metastable configurations which appear to be stable on the timescale of the simulations. We tried to shed more light on this

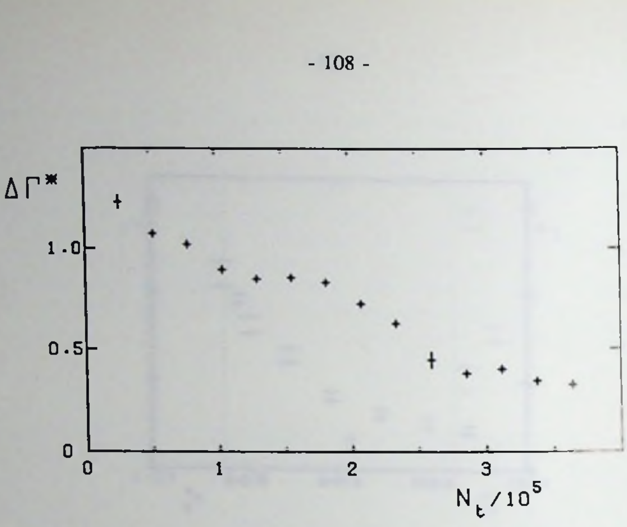

Fig. 8. Evolution of the difference $\Delta\Gamma$ between the left-hand and the right-hand side of the wall in case of an asymmetric system at $\varepsilon_r=0.70$. N_t denotes the number of timesteps. The points are averages over 26,000 consecutive timesteps.

metastability by surface tension measurements. Starting with a system in which the fluid particles were placed on a lattice with more lattice layers near the l.h.s. of the wall than near the r.h.s., we formed a system that was strongly asymmetric. The wall-fluid affinity was set at $\varepsilon_r=0.70$. This system was followed for an extremely long time and fig. 8 shows the evolution of the difference in coverage $\Delta\Gamma=\Gamma_l-\Gamma_r$. It can be seen from the figure that the difference gets smaller but so slowly that the determination of the final equilibrium state is probably beyond the reach of these simulations. We have both extracted particles from and added particles to the gas phase to obtain strongly asymmetric systems at other vapor densities. All these states are listed in table 1 in which the data are averages over the last few subruns of the slowly evolving systems. The coverages in this table are roughly at the adsorption curve of fig. 6.

If the system does exhibit a prewetting transition, it is expected that the side of the wall with the lowest coverage has the lowest surface tension at vapor densities below the transition whereas the side with the largest coverage has the lowest surface tension above the transition. Table 1 lists the surface tensions of the two sides, measured in the way explained in section 3. The table shows that the left-hand side of the wall, which has the largest coverage, has the lowest surface tension at all vapor densities. It does therefore not point at the presence of a prewetting transition.

We have increased the ε_r of these systems to 0.75 to inspect whether these large asymmetries can also be maintained at larger ε_r. This is indeed the case: one obtains asymmetric systems with vapor densities between $n_b^*=0.04$ and the coexisting density which seem to relax very slowly towards a symmetric state. The surface tension of the side of the wall with the largest coverage is always the lowest. So the phenomena are essentially the same as in the $\varepsilon_r=0.70$ case.

n_b^*	Γ_l^*	Γ_r^*	γ_l^*	γ_r^*
0.0411(4)	0.643(9)	0.522(4)	−0.240(3)	−0.218(3)
0.0431(4)	1.043(7)	0.654(6)	−0.280(3)	−0.243(2)
0.0450(5)	1.298(8)	0.934(9)	−0.303(3)	−0.278(3)
0.0454(4)	1.685(6)	1.132(8)	−0.311(4)	−0.292(2)

Table 1. Reduced bulk vapor density n_b^*, reduced coverages Γ_l^* and Γ_r^* and the reduced surface tensions γ_l^* and γ_r^* of the left and right-hand side of the wall respectively. These data are for four asymmetric systems at $\varepsilon_r=0.70$ and are calculated as an average over approximately 8000 configurations. Numbers between parentheses denote the error in the last decimal.

4. Conclusions.

We have carefully examined the adsorption curves of a wall-vapor interface at several values of the wall-fluid affinity ε_r. Previous simulations[12,13,14] have revealed the presence of a strongly first-order wetting transition in this system and thus, a prewetting transition is to be expected. The adsorption curves also show the presence of a wetting transition: the coverage remains finite on the approach of coexistence at $\varepsilon_r=0.65$ while it seems to diverge at $\varepsilon_r=0.75$. It can be disputed whether the coverage diverges or not in the intermediate case $\varepsilon_r=0.70$. We thus estimate the wetting transition to occur at $\varepsilon_w=0.70\pm0.05$, in agreement with the previous estimates.

The more subtle effects associated with prewetting cannot unambiguously be observed in our simulations. The simulations suffer from a number of disadvantages. At first, we have seen that the fluctuations and the relaxation times in the system are very large and could mask the signals of a prewetting transition. Secondly, we expected that the use of effectively two walls, which are in fact the two sides of the same wall, enables one to observe a prewetting transition as a difference in the coverage at the two sides. However, the sides turn out to be "decoupled" on the timescale of the simulations in the sense that local equilibria are reached at both sides of the wall but a global equilibrium of the entire system is not obtained. This is e.g. clearly demonstrated by the systems at coexistence at $\varepsilon_r=0.65$. They are partially wet according to the fact that the coverage remains finite on the approach of coexistence. Nevertheless, the liquid condenses at both walls at coexistence whereas the equilibrium configuration is one with the entire liquid phase adsorbed at one side and the vapor phase adsorbed at the other side of the wall[12]. The coupling between the walls is poor because they have to communicate via the dilute vapor phase. The only way to provide transport of particles between the two sides of the wall is via diffusion through the vapor phase which is a slow mechanism. The coupling via the vapor phase is therefore not efficient. When the walls are decoupled, the subtle growth behaviour of the coverage on the passage of the prewetting transition as sketched in section 2, will not occur. Therefore, we have no advantage of the use of "two" walls.

As a third disadvantage, our simulations with a fixed temperature and volume may be less suited to observe prewetting than the isobaric simulations of Finn and Monson[9]. Gradually changing the amount of particles, we should encounter walls that are partially covered with the thick and partially covered with the thin film as we pass the prewetting transition. On the contrary, the prewetting transition is observed as a true discontinuity in the coverage as the transition is passed in the isobaric simulations. Such a discontinuity may be more easy to observe. Furthermore, the distance to coexistence can be tuned exactly, i.e. in terms of the pressure, in the isobaric simulations whereas the vapor density cannot be fixed directly in our canonical simulations.

In spite of these objections, we would expect that a prewetting transition with an appreciable difference in coverage between the coexisting films which occurs not too close to coexistence, would be observable. Compared with the simulations of Finn and Monson, our simulations differ apart from the simulation techniques, isobaric Monte-Carlo versus canonical molecular-dynamics simulations, from theirs in two respects. Namely, the representation of the wall is different and we scan a range of wall-fluid affinities ε_r at a fixed temperature whereas Finn and Monson scan a range of temperatures at a fixed wall-fluid interaction. These differences should not affect the qualitative character of the prewetting transition but the quantitative differences may be considerable.

From the estimate of ε_w as $\varepsilon_w = 0.70 \pm 0.05$ and the absence of any sign of prewetting at $\varepsilon_r = 0.75$, our simulations indicate the critical wall-fluid interaction of the prewetting transition ε_{cpw} to be within $0.1\varepsilon_{ff}$ of the wetting threshold ε_w. The adsorption curves seem to exclude the possibility of prewetting effects at densities of $0.003/\sigma_{ff}^3$ below n_c so we estimate the critical vapor density within $0.003/\sigma_{ff}^3$ of the saturation vapor density. These estimates agree with a density functional calculation of Velasco and Tarazona[17]. Previously, they have carried out a calculation[18] of the location of the wetting and drying transition in this particular wall-fluid system, a calculation which they have extended to investigate the prewetting line. They locate the wetting transition at $\varepsilon_w = 0.75$ and the coexistence density at $n_c^* = 0.042$ but of more importance with regard to the present work is that they predict the prewetting line to be very small. The difference between ε_{cpw} and ε_w is estimated to be 0.1 and the difference between n_c^* and n_{cpw}^* only 0.005. Especially the latter is very small, implying that the whole prewetting line remains very close to the coexistence line and that it will be hard to observe it with the accuracy of our simulations.

References

1) for a review see e.g. S. Dietrich, in *Phase Transitions and Critical Phenomena*, edited by C. Domb and J. Lebowitz (Academic, London, 1988), Vol 12.

2) D. Nicolaides and R. Evans, preprint.

3) E.H. Hauge and M. Schick, Phys. Rev. B **27**, 4288 (1983).

4) J.W. Cahn, J. Chem. Phys. **66**, 3667 (1977).

5) C. Ebner and W.F. Saam, Phys. Rev. Lett. **38**, 1486 (1977).

6) A. Velasco and P. Tarazona, Phys. Rev. A **39**, 6402 (1989).

7) C. Ebner, Phys. Rev. A **23**, 1925 (1981).

8) A.K. Sen and C. Ebner, Phys. Rev. B **33**, 5076 (1986).

9) J. Finn and P.A. Monson, Phys. Rev. A **39**, 6402 (1989).

10) J.W. Schmidt and M.R. Moldover, J. Chem. Phys. **84**, 4563 (1986).

11) G. Ascarelli and H. Nakanishi, J. Phys. France **51**, 341 (1990).

12) J.H. Sikkenk, J.O. Indekeu, J.M.J. van Leeuwen, E.O. Vossnack and A.F. Bakker, J. Stat. Phys. **52**, 23 (1988).

13) M.J.P. Nijmeijer, C. Bruin, A.F. Bakker and J.M.J. van Leeuwen, chapter III of this thesis.

14) M.J.P. Nijmeijer, C. Bruin, A.F. Bakker and J.M.J. van Leeuwen, chapter IV of this thesis.

15) A.F. Bakker and C. Bruin, in *Special Purpose Computers*, edited by B.J. Alder (Academic, London, 1988).

16) F. van Swol, Phys. Rev. Lett. **60**, 239 (1988).

17) A. Velasco and P. Tarazona, private communication.

18) A. Velasco and P. Tarazona, J. Chem. Phys. **91**, 7916 (1989).

CHAPTER VIII

The Lennard-Jones liquid-vapour interface

ABSTRACT

The surface tension of a Lennard-Jones liquid-vapour interface has been determined accurately in a molecular dynamics simulation. Our values tend to be smaller than those from previous simulations. It is shown that the usually truncated tail of the potential strongly increases the surface tension if taken into account.

I. Introduction

The thermodynamic description of an interface goes back to Gibbs[1)]. In a thermodynamic language, the properties of a fluid change stepwise between those of the coexisting bulk phases. Van der Waals was the first to recognize that the bulk phases connect smoothly in the interface. He expressed the free energy as an integral over a local free energy density which includes the contributions due to the inhomogeneity of the system through a squared gradient term of the density profile[2)]. It took until around 1950 before two exact expressions[3-4)] appeared for the surface tension in terms of molecular distribution functions. Up to now no first principle theory exists for the calculation of these correlation functions. However, plausible assumptions (density functionals) have led to fairly succesful descriptions of interfacial profiles.

For a long time, the theories could only be checked against measurements of real physical systems, e.g. an argon liquid-vapour interface[5)]. The surface tension is however, as we shall see below, a delicate function of the potential. Thus computer simulations can provide for an important test for theories as the molecular interactions are completely specified in such experiments. Moreover, possible discrepancies between model systems and reality can be brought to focus unambiguously. By computer simulations, the molecular correlations needed for a computation of the surface tension can be determined with an accuracy limited only by statistics.

A typical fluid potential used is the Lennard-Jones 12-6 potential

$$\phi(r) = 4\varepsilon\ \{(\sigma/r)^{12} - (\sigma/r)^{6}\} \tag{1.1}$$

where r is the interparticle distance, ε the well of the potential and σ the length scale. A special difficulty presents the tail of the Lennard-Jones potential. In order to keep the computer simulations within an acceptable time, the interaction has to be cut off beyond some distance r_c. Such a truncated Lennard-Jones potential reads

$$\phi_c(r) = \begin{cases} 4\varepsilon\ \{(\sigma/r)^{12} - (\sigma/r)^{6}\} & r \le r_c \\ 0 & r > r_c \end{cases} \tag{1.2}$$

The surface tension γ of a Lennard-Jones fluid with a truncated potential is believed to be rather strongly dependent on r_c. Some theories[6)] predict a change in γ varying from about 40% at the triple point temperature until 90% at the critical temperature as r_c grows from 2.5σ to ∞.

A number of simulations of a 3-dimensional Lennard-Jones liquid in equilibrium with its vapour have been carried out since 1974. These include both molecular dynamics and Monte Carlo simulations of different systems: various numbers of particles, boundary conditions and ways to cut off the Lennard-Jones potential are reported. The attention in these simulations has been focussed on the form of the interface profile and the surface tension. An outline of the resulting values of the surface tension (without any tail correction) is given in figure 1 where the reduced surface tension $\gamma^* = \gamma\sigma^2/\varepsilon$ is plotted against the reduced temperature $T^* = k_B T/\varepsilon$ (k_B is Boltzmann's constant). Comparing the various values one sees a large variation in results. We present accurate values of the surface tension for four different temperatures as found in molecular dynamics simulations of large systems with a

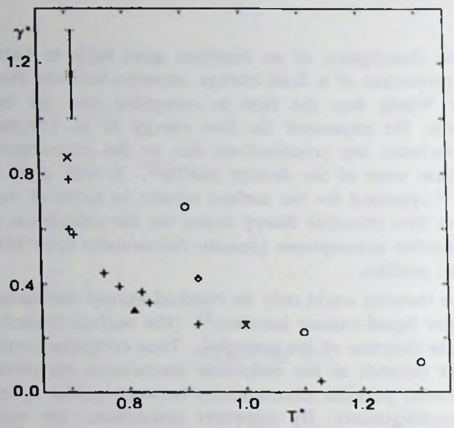

Fig. 1. Reduced surface tension of a Lennard-Jones fluid versus reduced temperature as found in previous simulations. The following simulations are included: + Chapela *et al*[6], × Rao and Levesque[8], ◇ Rao and Berne[9], O Liu[10], Δ Opitz[11], * Lee *et al*[12], ☓ van Swol and Henderson[13]. The result of van Swol and Henderson regards a square-well fluid.

truncated potential. In addition, a simulation of a smaller system with a three times larger cut-off distance was carried out to measure the effect of the truncation.

2. Description of the system

Apart from those in the smaller system, our measurements have been carried out on the Delft Molecular-Dynamics Processor (DMDP)[7], which is specially designed for molecular dynamics simulations of simple fluids. The use of this computer enabled us to simulate large systems .

A 3-dimensional system of coexisting liquid and vapour was simulated on the DMDP at four different temperatures: T^*=0.72, T^*=0.80, T^*=0.90 and T^*=1.00. These temperatures scan the range between the triple point temperature $T_t^* \approx 0.70$ and the critical temperature $T_c^* \approx 1.25$. For the two lowest temperatures, our system contains 10,390 particles while for T^*=0.90 and T^*=1.00 it has 7968 resp. 7619 particles. For all these temperatures, the particles are enclosed in a computational box of dimensions $L_x \times L_y \times L_z = 29.1\sigma \times 29.1\sigma \times 29.1\sigma$ with periodic boundary conditions. The particles interact via a Lennard-Jones 12-6 potential truncated at 2.5σ. Initially, a fluid strip with a width of $\sim 16\sigma$ was placed in the box parallel to the x-y plane and the remaining space was filled with vapour. There was no external potential applied: the system proved to be stable by itself. We allowed the system to equilibrate during 10×10^3 timesteps which was long enough to obtain a steady density profile, internal energy and surface tension. The reduced timestep $\Delta t^* = \Delta t\sqrt{\varepsilon}/(\sigma\sqrt{m})$ (where m is the mass of the particle) we used in our algorithm, was chosen to be 0.01. After the equilibration period, the density and pressure profiles (see next section) were

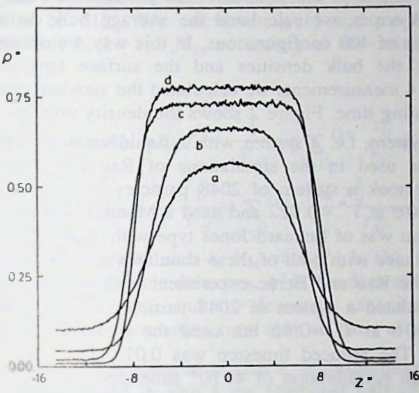

Fig. 2. Density profiles of liquid-vapour interfaces at coexistence for the reduced temperatures 1.00 (a), 0.90 (b), 0.80 (c) and 0.72 (d) as simulated with the DMDP. The profiles are obtained from simulations of 20.8×10^3 timesteps each.

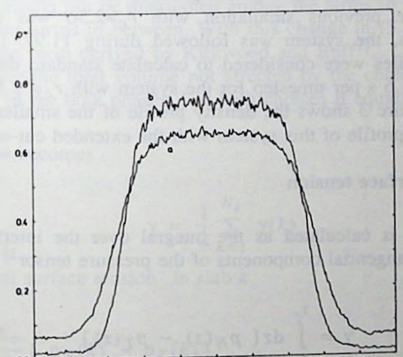

Fig. 3. Density profiles of liquid-vapour interfaces at coexistence for systems with a cut-off radius of 2.5σ (a) and 7.33σ (b) respectively, as simulated with the IBM. The profiles are obtained from simulations of 12×10^3 timesteps each.

measured each thirteenth timestep. We sampled 1600 profiles for each temperature. In order to estimate the statistical errors, we calculated the average bulk densities and the average surface tensions of subsets of 400 configurations. In this way we obtained for each temperature 4 measurements of the bulk densities and the surface tension, which we took as independent. From these 4 measurements we calculated the standard deviation. Each timestep costed about 2.5 s computing time. Figure 2 shows the density profiles.

The same type of system, i.e. a system with 2 liquid-vapour interfaces and no external boundary conditions was used in the simulations of Rao and Levesque[8)] and Rao and Berne[9)]. Rao and Berne took a system of 2048 particles in a periodic box of dimensions $14.66\sigma \times 14.66\sigma \times 25.10\sigma$ at $T^* = 0.922$ and used a Monte Carlo procedure to generate the configurations. The system was of Lennard-Jones type with a cut-off distance r_c=2.5σ. Our DMDP results are at variance with both of these simulations, as will be seen later on. Therefore, we have repeated the Rao and Berne experiment with a general purpose computer, an IBM 3083-JX1. We simulated a system of 2048 particles in a periodic box of dimensions $14.66\sigma \times 14.66\sigma \times 25.10\sigma$ at $T^* = 0.92$ but used the molecular dynamics instead of the Monte Carlo technique. The reduced timestep was 0.01. This system was followed over 12×10^3 timesteps after an equilibration of 4×10^3 timesteps. The pressure and density profiles were measured each timestep. Errors are estimated by averaging over subsets of 1.2×10^3 timesteps. This gives us 10 measurements which we used to calculate standard deviations.

To study the effect of the attractive tail of the interparticle potential, the cut-off radius in this system was increased to r_c=7.33σ. Other features of the system, e.g. the temperature T^*=0.92, remained the same. As a starting configuration for this simulation, a particle configuration obtained by the previous simulation with r_c=2.5σ was used. After 1.68×10^3 timesteps of equilibration, the system was followed during 11.97×10^3 timesteps. Sixteen subsets of 0.63×10^3 profiles were considered to calculate standard deviations. The computing time increased from 1.6 s per timestep for the system with r_c= 2.5σ to 22 s for the system with r_c= 7.33σ. Figure 3 shows the density profile of the smaller system with r_c=2.5σ together with the density profile of this system with the extended cut-off radius.

3. Calculation of the surface tension

The surface tension is calculated as the integral over the interface of the difference between the normal and tangential components of the pressure tensor[1)]

$$\gamma = \int_{z_l}^{z_v} dz\{\, p_N(z) - p_T(z) \} \tag{3.1}$$

where bulk liquid is assumed to be at the left of the interface and bulk vapour at the right, z_l is an arbitrary position in the bulk liquid, z_v an arbitrary position in the bulk vapour. The normal component $p_N(z)$ and tangential component $p_T(z)$ are equal to the thermodynamic pressure p in the bulk phases. The components differ from each other in the interface zone. In the case of our system with two interfaces the surface tension is calculated as

$$\gamma = \frac{1}{2}\int_{0}^{L_z} dz\{\, p_N(z) - p_T(z) \} \tag{3.2}$$

To evaluate this integral, we divide the box into N_s slabs of length L_z/N_s parallel to the x-y plane. N_s was taken to be 512. We calculate $p_N(k)$ and $p_T(k)$, the local normal and tangential pressures in slab k, $k=1,\ldots,N_s$, according to the statistical mechanical expressions[1])

$$p_N(k) = < n(k) > k_B T - \frac{1}{V_{sl}} < \sum_{(i,j)}^{(k)} \frac{z_{ij}^2}{r_{ij}} \phi'(r_{ij}) > \tag{3.3}$$

$$p_T(k) = < n(k) > k_B T - \frac{1}{V_{sl}} < \sum_{(i,j)}^{(k)} \frac{\frac{1}{2}(x_{ij}^2 + y_{ij}^2)}{r_{ij}} \phi'(r_{ij}) > \tag{3.4}$$

where $n(k)$ is the particle density in slab k, $V_{sl} = L_x L_y L_z / N_s$ is the volume of a slab, x_{ij}, y_{ij}, z_{ij} and r_{ij} are the interparticle distances, ϕ' is the derivative of the full interparticle potential, it is truncated beyond $r=r_c$, and $< >$ denotes a canonical ensemble average. The summation $\sum_{(i,j)}^{(k)}$ means that the summation runs over all pairs of particles (i,j) of which at least one of the particles i and j is situated in slab k. It furthermore means that, if only one particle, either i or j, was situated in slab k we attributed half of the contribution of pair (i,j) to slab k while when both particles were situated in slab k we attributed the total contribution to that slab. The contribution of pair (i,j) is $z_{ij}^2 \phi'(r_{ij})/r_{ij}$ in the case of p_N, $(x_{ij}^2 + y_{ij}^2)\phi'(r_{ij})/(2r_{ij})$ in the case of p_T as expressed in (3.3) and (3.4).

We should remark that definition (3.3) of the local pressure $p_N(k)$ is used for computational efficiency but formally not correct. To obtain a correct definition of $p_N(k)$, the contribution of a pair (i,j) should not be distributed among the strips in which the particles i and j reside but among all the strips in between. With this change in (3.3) and (3.4) unaltered, the pressure tensor is in the form derived by Kirkwood and Buff[2]). Clearly, the surface tension is as an integration over the total volume not affected by the choice of the distribution. The same holds for $p_N(k)$ in the bulk phases. For both choices it equals the thermodynamic pressure p there.

Integral (3.2) now becomes

$$\gamma = \frac{1}{2} \sum_{k=1}^{N_s} \gamma(k) \tag{3.5}$$

where $\gamma(k)$ is the "local surface tension" in slab k

$$\gamma(k) = \frac{L_z}{N_s} \{ p_N(k) - p_T(k) \}$$
$$= \frac{1}{L_x L_y} < \sum_{(i,j)}^{(k)} \frac{\frac{1}{2}(x_{ij}^2 + y_{ij}^2) - z_{ij}^2}{r_{ij}} \phi'(r_{ij}) > \tag{3.6}$$

Besides the necessity of a constant bulk density, a second condition for the presence of a well defined bulk liquid or bulk vapour in a slab k becomes

$$\gamma(k) = 0 \tag{3.7}$$

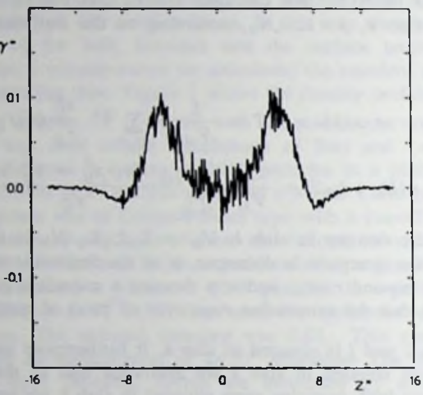

Fig. 4. Profile of the "local surface tension" for a liquid-vapour interface at coexistence for T^* =0.90 as simulated with the DMDP. The profile is obtained from a simulation of 20.8×10^3 timesteps.

T^*	γ^*	ρ_l^*	ρ_v^*	r_c	
0.72	0.55 ±0.01	0.7764±0.0002	0.0093±0.0002	2.5σ	DMDP
0.80	0.39 ±0.01	0.7315±0.0003	0.0195±0.0007	"	
0.90	0.224±0.009	0.662 ±0.001	0.0439±0.0009	"	
1.00	0.088±0.007	0.565 ±0.001	0.103 ±0.001	"	
0.92	0.24±0.02	0.649±0.003	0.063±0.003	2.5σ	IBM
0.92	0.63±0.02	0.740±0.002	0.018±0.001	7.33σ	

Table 1. Reduced surface tension and bulk densities for the investigated temperatures, the fifth and sixth column specify to which system the data pertains (see also text).

As an example, figure 4 shows the profile of the local surface tension of the system at T^*=0.90. The reduced surface tensions, reduced bulk liquid densities $\rho_l^* = \rho_l\sigma^3$ and the reduced bulk vapour densities $\rho_v^* = \rho_v\sigma^3$ resulting from our simulations are listed in table 1.

4. Comparison with other results and conclusion

The outline given in fig 1 shows rather widely varying results. Some of these were obtained in systems that were rather small (e.g. 129 particles used by Liu[10)], 300 particles used by Opitz[11)]), had an external potential to stabilize it (Lee *et al*[12]) or exhibited an oscillatory structure in the density profile (Lee *et al*) that has not been reproduced afterwards. Opitz modified the Lennard-Jones potential to make it vanish beyond 2.94σ while Liu does not specify a cut-off radius. The influence of these aspects on the surface tension is not well understood. A special case is the square-well fluid result of van Swol and Henderson[13]; a comparison with their number is difficult anyhow. Notice that, if necessary and not specified in the original publication, we took σ=3.405Å and ε/k_B=119.4K to convert the data into reduced units.

Such objections do not hold for the systems of Rao and Berne and Rao and Levesque. Their simulations seem capable of giving accurate surface tensions. We obtain nevertheless different results. But the agreement on the surface tension between the repetition of the Rao and Berne experiment and the DMDP results, favours our values. It also indicates that no errors occurred in the rather involved computer programs. The results of Chapela *et al*[6] are confirmed by our experiment. If we make a more detailed analysis of the way Chapela *et al* calculated the surface tension, we remark that they did not determine the local pressure tensor. Thus they had to guess from the density profile at which point the influence of their "wall" has vanished and bulk conditions start. An "effective surface" was introduced at that point to compensate for the fact that they did not take interactions over this "surface" into account. This "effective surface" gives corrections on their simulation results, varying from 39% till 90% for the various temperatures. These considerations make us believe that our measurements, being direct and in large systems, form the most accurate determination of the surface tension of a Lennard-Jones liquid-vapour interface.

We must remark that for the temperature T^*=1.00 the interface becomes so broad that our system is too small to establish 2 genuine bulk phases. But since we are very close to the situation with 2 well developed bulk phases we do not believe that this restriction will significantly influence our data.

The tail of the interaction influences the interface significantly. Our simulation shows an increase of the surface tension with a factor 2.8 at T^*=0.92 as the interaction range is changed from 2.5σ to 7.33σ. The discrepancy between simulation results with r_c=2.5σ and the observed surface tension of noble gases[5], γ^*=0.50 at T^*=0.92, can be ascribed partly to the omittance of the attractive tail. Besides the change in surface tension, the bulk liquid density increases with 14% while the vapour density diminishes with a factor 3.5.

References

1) S. Ono and S. Kondo, *Encyclopedia of Physics* (ed. S. Flugge), vol 10, (*Springer, Berlin*, 1960).

2) J.S. Rowlinson and B. Widom, *Molecular Theory of Capillarity* (*Clarendon, Oxford*, 1982).

3) F.P. Buff, Zeit. Elektrochem. **56,** 311 (1952).

4) D.G. Triezenberg and R. Zwanzig, Phys. Rev. Lett. **28,** 1183 (1972). previously presented by Yvon in 1948 but not published

5) D. Stansfield, Proc. Phys. Soc. London **72,** 854 (1958).

6) G.A. Chapela, G. Saville, S.M. Thompson and J.S. Rowlinson, J. Chem. Soc. Faraday Trans. 2 **8,** 1133 (1977).

7) Bakker A.F., *Design and implementation of the Delft Molcular-Dynamics Processor* thesis, Technische Universiteit Delft (1983), unpublished
A.F. Bakker, C. Bruin and H.J. Hilhorst, Phys. Rev. Lett. **62**, 449 (1984).

8) M. Rao and D. Levesque, J. Chem. Phys. **65**, 3233 (1976).

9) M. Rao and B.J. Berne, Mol. Phys. **37**, 455 (1979).

10) K.S. Liu, J. Chem. Phys. **60**, 4226 (1974).

11) A.C.L. Opitz, Phys. Lett. **47A**, 439 (1974).

12) J.K. Lee, J.A. Barker and G.M. Pound, J. Chem. Phys. **60**, 1976 (1974).

13) F. van Swol and J.R. Henderson, J. Chem. Soc. Faraday Trans. 2 82, 1685 (1985).

CHAPTER IX

Measurement of the surface tension of a drop

ABSTRACT

The curvature dependence of the liquid-vapor surface tension is described in the limit of small curvatures by Tolman's length. Knowledge about this length, both experimentally and theoretically, is scarce. From an analysis of the pressure difference over the interface, we obtain an expression for Tolman's length in terms of the pressure tensor which is independent of the choice of the tensor. This pressure difference is studied in a simulation of liquid drops, leading to an estimate of Tolman's length. This length appears to be small and we give bounds on it.

1. Introduction.

Curved interfaces appear in many contexts but the influence of the curvature on e.g. the surface tension is still poorly understood. The curvature is not only reflected in the properties of the interface but also in the state of the bulk phases that are separated by the interface. This was already understood by Laplace who considered a liquid droplet "floating" in a vapor phase and noticed that the surface tension of the liquid-vapor interface, which he viewed as a mechanical force, tries to contract the spherical surface of the droplet. The droplet must therefore be stabilized by a pressure difference over the interface that balances the contraction. This condition for mechanical equilibrium is expressed by Laplace's law[1)] which reads for a three-dimensional fluid

$$\Delta p = \frac{2\gamma}{R} \tag{1.1}$$

where Δp is the pressure in the liquid minus the pressure in the vapor phase, γ the surface tension and R the radius of the droplet. The question of the effect of the curvature on the properties of the interface, however, is more subtle. The argument behind (1.1) does not tell anything about the value of γ : one can only say that it will become equal to that of a planar surface as the radius of the droplet grows larger. In practical applications, the influence of the curvature on γ is usually neglected as giving rise to small corrections, an assumption which can be justified if the radii of curvature are large. However, in cases like the nucleation of droplets in a supersaturated vapor, where small radii necessarily occur, it has been noticed that, depending on the sensitivity of γ on the curvature, the so called "critical radius of nucleation" may be changed significantly[2)]. The curvature dependence also appears in the capillary wave theory[3)] of the liquid-vapor interface in which the interface is viewed as an "intrinsic" interface with a fluctuating position. The statistical weight of the fluctuations depends on the surface tension of the intrinsic interface and since short-wavelength fluctuations display large curvatures, they may be suppressed if the surface tension increases with curvature or amplified otherwise.

From a macroscopic point of view such as taken by Laplace, the interface between the droplet and the surrounding vapor is sharp and therefore, the radius of the drop is well defined. Microscopically however, the interface has a finite width and there is some freedom in the choice of the droplet radius R. Moreover, as will be discussed in the next section, the surface tension attributed to the surface depends on the choice of R and the Laplace equation (1.1) has to be modified to account for this dependence. A convenient radius to measure the size of the droplet is the "equimolar dividing radius" R_e. The surface tension associated with the choice for R_e as the droplet radius is denoted γ_e (see the next section).

Since the surface tension $\gamma_e(R_e)$ of a spherical interface with radius R_e approaches the planar limit γ_∞ for large radii, it seems reasonable to expand it in powers of $1/R_e$:

$$\frac{\gamma_e(R_e)}{\gamma_\infty} = 1 - \frac{2\delta}{R_e} + O(R_e^{-2}) \tag{1.2}$$

The coefficient δ is called Tolman's length after Tolman[4)] who derived expansion (1.2) on the basis of thermodynamic arguments thereby obtaining an identity for δ which reads

$$\delta = z_e - z_s \tag{1.3}$$

where z_e denotes the equimolar dividing surface of the planar interface and z_s a special choice of dividing surface which we will discus in the next section. All knowledge about δ has been obtained from theoretical considerations and simulations as there is no reliable experimental estimate of this length. A statistical-mechanical theory should try to connect δ or, if possible, the full $\gamma_e(R_e)$ to the microscopic properties of the interface. Such relations have indeed been derived from a combination of mechanical and thermodynamic arguments and express γ_e and δ in terms of the normal and tangential component p_N and p_T of a pressure tensor[1,5]. The relation between γ_∞ and the pressure tensor of a planar interface is well understood but the extension to finite curvatures is not free from ambiguities. The proposed expression for δ for example, reads[6]

$$\delta = \frac{1}{\gamma_\infty} \int_{-\infty}^{\infty} dz \; (z_e - z) \; (p_N^\infty(z) - p_T^\infty(z)) \tag{1.4}$$

where p_N^∞ and p_T^∞ are the tensor components for a planar interface. The above defined δ, however, depends[5] on the choice of the pressure tensor which is unacceptable if $\gamma_e(R_e)$ is to represent a physical quantity.

Further work has been done in various directions. Expressions of the type (1.4) relate δ via the pressure tensor to the paircorrelation function of the fluid. The ambiguities in this so called "virial route" has directed the attention to the "compressibility route" in which the correlations are described by the direct correlation function. One has obtained[7] expressions for γ and δ in terms of this function which are certainly of a theoretical importance but have little practical implications since the direct correlation function cannot be evaluated easily. Curved surfaces have also been studied[8] in the framework of the Landau-van der Waals theory in which Tolman's length can be expressed entirely in terms of the density profile of the planar interface. The behaviour of δ as the temperature approaches the critical temperature T_c can also be studied in this context and the theory predicts δ to diverge with an explicitly given critical exponent. Tolman's length can further be calculated[9] explicitly in the model of penetrable spheres.

An extensive effort to obtain Tolman's length for a realistic system has been made in a molecular-dynamics simulation of Thompson *et al*[10]. They have simulated liquid drops of Lennard-Jones particles immersed in a coexisting vapor phase at various temperatures. These systems consist of a maximum of 2048 particles. For two temperatures, they scan a range of droplet radii from 3 to 6σ (where σ determines the core of the Lennard-Jones potential) while at several other temperatures, they simulate only one or two drop sizes. Their results for δ show large statistical uncertainties and vary, for those two temperatures for which a range of droplet sizes has been studied, with the droplet radius. Nevertheless, the values they obtain for δ are nearly all positive and therefore they conclude that it seems clear that δ is positive which would imply that γ_e decreases with increasing curvature according to (1.2).

We have carried out simulations of the same type but try to scan an as large as possible range of droplet sizes at one teperature. By the use of a special-purpose computer, we can simulate droplets with a radius up to 13σ which turns out to be already so large that the effect of the curvature on γ can no longer be detected. Before we describe the simulations in section 3, we will recapture the thermodynamics of curved interfaces in the next section. We show that δ can be obtained from a measurement of the pressure difference Δp as a function of the droplet radius R_e. Moreover, the same analysis shows that (1.4) can be replaced by an expression which is independent of the choice of the tensor. The simulations are described in sections 3 and 4 and finally, conclusions are drawn is section 5.

2. Thermodynamics.

Consider a d-dimensional volume V in which a droplet, surrounded by a coexisting vapor phase, is contained. We do not specify the dimensionality to generalize the discussion although the case $d=3$ will be the one we are finally interested in. The volume V is considered to be a volume with periodic boundaries in which a fixed number of N particles are enclosed at a fixed temperature T, such as encountered in the simulations. On a microscopic level, the liquid-vapor interface is not sharp but has a finite width so the radius of the drop is not uniquely defined. We have to choose a "dividing surface" with a "dividing radius" R which represents the interface. This choice is in principle free but only a location of the dividing surface within the physical interface makes sense. The dividing surface separates the volume in a volume V_l attributed to the liquid phase and a volume V_v attributed to the vapor phase with

$$V_l + V_v = V \tag{2.1}$$

and

$$V_l = \omega_V R^d \tag{2.2}$$

where the numerical constant ω_V depends on the dimensionality. The liquid-vapor interface is attributed an area A equal to

$$A = \omega_A R^{d-1} \tag{2.3}$$

The surface tension γ is defined as an excess free energy. This excess can only be well defined if the liquid and vapor phase are so large that they exhibit the properties of a bulk phase, in spite of the fact that they should be of a finite size for the drop to be stable. In particular, one should be able to attribute a bulk density n_l and pressure p_l to the liquid phase and density n_v and pressure p_v to the vapor phase. These requirements turn out to be satisfied in the simulations except for very small drops where the liquid phase is not well developed. The surface tension can then be defined from the free energy F of the entire system as

$$F = (-p_l + \mu n_l)\, V_l + (-p_v + \mu n_v)\, V_v + (\gamma + \mu\Gamma)\, A \tag{2.4}$$

where μ denotes the chemical potential of the system and the coverage Γ is the number of particles attributed to the interface:

$$N = n_l V_l + n_v V_v + \Gamma A \tag{2.5}$$

Solving (2.4) for γ one finds with the aid of (2.1)-(2.3) and (2.5)

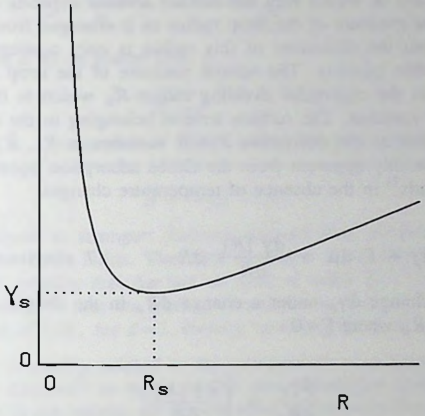

Fig. 1. Schematic plot of the dependence of the surface tension γ on the choice of dividing radius R. The minimum of the curve is at (R_s, γ_s).

$$\gamma\,[R] \;=\; \frac{F-\mu N+p_v V}{\omega_A}\,\frac{1}{R^{d-1}} \;+\; \frac{\Delta p}{d}\,R \tag{2.6}$$

where we also used that the ratio ω_A/ω_V equals d. Equation (2.5) shows the unfortunate feature that γ depends on the choice of R. As introduced by previous authors[1,8], we denote such a dependence by square brackets to stress the difference with a dependence on the physical size of the droplet. Note that Δp is positive because of the arguments of Laplace. For physical reasons, it is to be expected that the sum $(F-\mu N + p_v V)$ is also positive because otherwise γ can be made negative and arbitrarily large for very unphysical, namely very small, choices of R whereas one would expect an unphysical choice of R to be paid for by a large surface tension. Assuming the sum to be positive, the variation of γ with R is depicted in fig. 1. The choice of R that minimizes γ is called the "radius of tension" R_s and it is expected to be within the physical location of the interface. The corresponding minimum in the surface tension is denoted γ_s. From (2.6) one finds that γ satisfies the generalized Laplace equation

$$\Delta p \;=\; \frac{(d-1)\gamma}{R} \;+\; \frac{\partial\gamma\,[R]}{\partial R} \tag{2.7}$$

γ satisfies the original Laplace equation (1.1) exactly at R_s where the derivative $\partial\gamma/\partial R$ vanishes. Since γ obtains a minimum in R_s, it depends only weakly on the choice of R:

$$\frac{\gamma\,[R_s+\xi]}{\gamma_s} \;=\; 1 \;+\; O((\xi/R_s)^2) \tag{2.8}$$

where ξ denotes a distance of the order of the zeroth power of R_s, R_s^0.

The problem is now in which way the surface tension depends on the physical size of the droplet. The natural measure of the drop radius as it emerged from these thermodynamic considerations is R_s but the definition of this radius is only conceptual and R_s is not yet related to any observable quantity. The natural measure of the drop radius as it is deduced from the simulations is the equimolar dividing radius R_e which is the choice of radius for which the coverage Γ vanishes. The surface tension belonging to the equimolar dividing surface is denoted γ_e. Just as the derivative $\partial\gamma/\partial R$ vanishes at R_s, it satisfies a special property at R_e which is readily apparent from the Gibbs adsorption equation for the curved surface. This equation reads1) in the absence of temperature changes

$$d\gamma + \Gamma\, d\mu = \frac{\partial\gamma\,[R]}{\partial R}\, dR \qquad (T \text{ constant}) \tag{2.9}$$

If one considers the change $d\gamma_e$ under a change dR_e in the droplet radius, one finds from (2.9) evaluated at $R=R_e$ where $\Gamma=0$

$$\frac{d\gamma_e}{dR_e} = \left[\frac{\partial\gamma\,[R]}{\partial R}\right]_{R=R_e} \tag{2.10}$$

Returning to the question of the dependence of γ on the droplet size, we pursue again the idea of an expansion of γ in powers of the inverse droplet radius, especially since the definition of γ makes sense for not too small drops only. The expansion for γ_s is written as

$$\frac{\gamma_s}{\gamma_\infty} = 1 + \frac{a}{R_s} + O(R_s^{-2}) \tag{2.11}$$

with a yet undetermined expansion coefficient a. However, because of (2.8), a does not depend on the choice of dividing surface and we can write with equal validity

$$\frac{\gamma_e}{\gamma_\infty} = 1 + \frac{a}{R_e} + O(R_e^{-2}) \tag{2.12}$$

provided that the difference $\bar{\delta}=R_e-R_s$ is of the order R_s^0. Evaluating (2.7) at $R=R_s$ and substituting (2.11) one expresses Δp in a and R_s

$$\Delta p = \gamma_\infty \left(\frac{d-1}{R_s} + \frac{a(d-1)}{R_s^2} + \cdots\right) \tag{2.13}$$

Evaluating (2.7) at $R=R_e$ one finds with (2.10) and (2.12)

$$\Delta p = \gamma_\infty \left(\frac{d-1}{R_e} + \frac{a(d-2)}{R_e^2} + \cdots\right) \tag{2.14}$$

The latter equation is especially useful since it relates the unknown quantity a to the observables Δp, γ_∞ and R_e. The comparison of (2.13) and (2.14) implies a condition on a. Substitution of $R_e=R_s+\bar{\delta}$ in (2.14) gives

$$\Delta p = \gamma_\infty \left(\frac{d-1}{R_s} + \frac{a(d-2) - \delta(d-1)}{R_s^2} + \cdots \right) \tag{2.15}$$

where we have replaced $\bar{\delta}$ by its planar limit δ,

$$\delta = \lim_{R_s \to \infty} \bar{\delta} \equiv z_e - z_s \tag{2.16}$$

in the term of order R_s^{-2}. Comparison of (2.13) and (2.15) gives the Tolman[4] result

$$a = -(d-1)\,\delta \tag{2.17}$$

In fact, Tolman's analysis is stronger: Tolman showed that, provided the limit in (2.16) exists, the expansion in (2.11) holds. That this condition is not trivial can be seen in $d=2$ where expansion (2.14) implies that Δp has no term of order R_e^{-2} in this particular dimension. It has been suggested[11] that the leading correction on the r.h.s. of (2.12) should be of order $\log R_s/R_e$ instead of $1/R_e$ for $d=2$, thereby retaining the term of order R_e^{-2} in (2.14).

The coefficient a is readily related to the components of a local pressure tensor $\overleftrightarrow{p}(\vec{r})$. Such a tensor can be defined[5] in terms of the pair correlation function of the fluid and although this definition is not unique, all tensors have in common that they satisfy the condition

$$\nabla \cdot \overleftrightarrow{p}(\vec{r}) = 0 \tag{2.18}$$

in the absence of an external field. Furthermore, all tensors become isotropic in a bulk phase with diagonal components p, the pressure in the bulk. In a spherical symmetry, the tensor has only two independent components

$$\overleftrightarrow{p}(\vec{r};\, R_e) = p_N(r;\, Re)\, \hat{r}\hat{r} + p_T(r;\, R_e)\, (\overleftrightarrow{I} - \hat{r}\hat{r}) \tag{2.19}$$

with $\hat{r}$ a unit vector in the direction $\vec{r}$ and r the distance from the origin; the parameter R_e denotes the dependence of the tensor on the size of the droplet. (2.18) transforms to

$$\frac{\partial p_N}{\partial r} = -\frac{(d-1)}{r}\,(p_N - p_T) \tag{2.20}$$

Note that p_N and p_T both become equal to the bulk pressure p in a bulk phase. Integrating (2.20) from $r=0$ to a position R_v sufficiently deep in the vapor phase gives the pressure difference Δp

$$\Delta p = (d-1) \int_0^{R_v} dr\, \frac{1}{r}\, (p_N(r;\, R_e) - p_T(r;\, R_e)) \tag{2.21}$$

We expand (2.21) in powers of $1/R_e$ which is most easily done if we keep r at a fixed distance from R_e and expand the dependence of the tensor on the droplet size:

$$p_N(r - R_e;\, R_e) = p_N^\infty(z - z_e) + \frac{p_N^{(1)}(z - z_e)}{R_e} + O(R_e^{-2}) \tag{2.22}$$

where z_e is the position of the equimolar dividing surface of a planar interface. The expansion for p_T is analoguous . Inserting this expansion in (2.21) we obtain

$$\Delta p = \frac{(d-1)}{R_e} \int_{-\infty}^{\infty} \mathrm{d}z \, \{p_N^{\infty}(z) - p_T^{\infty}(z)\}$$

$$- \frac{(d-1)}{R_e^2} \int_{-\infty}^{\infty} \mathrm{d}z \, \{(z-z_e)\,(p_N^{\infty}(z)-p_T^{\infty}(z)) - (p_N^{(1)}(z)-p_T^{(1)}(z))\} \qquad (2.23)$$

The first integral on the r.h.s. gives[1,5] γ_{∞}; on comparison with (2.14) and (2.17) the second integral gives

$$\delta = \frac{1}{(d-2)\gamma_{\infty}} \int_{-\infty}^{\infty} \mathrm{d}z \, \{(z-z_e)\,(p_N^{\infty}(z)-p_T^{\infty}(z)) - (p_N^{(1)}(z)-p_T^{(1)}(z))\} \qquad (2.24)$$

Contrary to (1.4), this expression for δ is independent for the choice of the tensor since it is derived from (2.18) which holds for all tensors. Unfortunately, δ is not expressed in the pressure tensor of the planar interface alone but one needs to know how the tensor approaches its planar limit. It also shows that, unless the integral vanishes or expansion (2.22) is not correct, δ diverges in $d=2$ which implies that leading order in (2.12) should be $\log R_e/R_e$ instead of $1/R_e$. The notion that the integrand of (2.21) can be expanded in inverse powers of the droplet radius has already been made by Schofield and Henderson[5] but, since they neither invoke the pressure tensor, nor connect the coefficient of the second order term to δ, they do not obtain the result (2.24).

3. Description of the simulations.

We have simulated three-dimensional droplets enclosed in a cubic box with periodic boundary conditions. The fluid particles that are enclosed in the box interact through the Lennard-Jones 12-6 potential $\phi(r)$,

$$\phi(r) = 4\varepsilon \left[\left(\frac{\sigma}{r}\right)^{12} - \left(\frac{\sigma}{r}\right)^{6} \right] \qquad (3.1)$$

with r the interparticle distance, ε the energy scale and σ the length scale of the potential. The potential is truncated at 2.5σ. The simulations are of the molecular-dynamics type and are carried out on a special purpose computer, the Delft Molecular-Dynamics Processor (DMDP)[12], which enables us to study large systems for long times. The reduced timestep $\Delta t^* = \Delta t\sqrt{\varepsilon}/(\sigma\sqrt{m})$, where m is the mass of the particles, equals 0.01 in the simulations. The number of particles N, the length L of the box and the temperature T of the system are fixed in a simulation run. The sizes of the systems are listed in table 1. The table shows that the boxlength L is chosen smaller for smaller drops to avoid large vapor phases. Large vapor phases cause long equilibration times and, since one needs more particles to form the vapor phase, slow down the simulations. The temperature is chosen to be at a reduced value $T^* = k_B T/\varepsilon$ of 0.9 throughout the simulations, which is in between the triple point

N	L^*	R_e^*	N_C
2299	31	5.63(2)	44,000
5165	42	6.87(2)	24,000
6131	43	8.73(2)	16,800
9295	50	10.15(1)	10,000
10,420	50	11.53(1)	8,000
12,138	50	13.03(1)	8,000

Table 1. The sizes of the simulated systems. N denotes the number of particles, L^* the reduced boxlength, R_e^* the reduced equimolar radius and N_C the number of equilibrated particle configurations we have sampled to calculate the density and pressure tensor profiles. The values between paranthceses denote the error in the last decimal of R_e.

temperature $T_t^*=0.7$ and the critical temperature $T_c^*=1.26$. It is kept fixed in a way which is standard in constant temperature molecular-dynamics simulations, namely by regularly rescaling the velocities of all the particles to keep the average kinetic energy of the system at the value that corresponds with the desired temperature. The velocities are rescaled each 150^{th} timestep in our simulations which limits the temperature fluctuations to the order of 0.5% to 1% of the average temperature $T^*=0.9$.

Special attention was paid to the preparation and equilibration of the droplets because extremely long equilibration times are encountered if the system is not prepared carefully. We obtained reasonable, although still long, equilibration times by starting from initial configurations in which part of the fluid particles are placed in the centre of the box at a "crystal" of an FCC lattice. This "crystal" has a cubic shape and a density which is approximately the liquid density. The remaining part of the box is filled with a FCC lattice of particles at approximately the vapor density. The particles are given random velocities, drawn from a normal distribution appropriate to the temperature $T^*=0.9$. Starting the simulations, the lattices begin to melt and and a droplet and a vapor begin to form. We observed however, that the temperature of the "drop" almost always rapidly started to differ from the temperature of the "vapor" during the melting process. Although the difference vanished during the equilibration afterwards, it took such a long time that we sped up
the equilibration by adjusting the temperature of the drop and the vapor separately. This is simply done by calculating the kinetic energy of all particles in a volume attributed to the drop separately from the kinetic energy of the particles in the remaining volume, which is attributed to the vapor. The velocities of the particles in the drop volume are then scaled independently from the velocities of the vapor particles to bring both kinetic energies at the appropriate value. As soon as thermal equilibration had been obtained, we no longer distinguished between a temperature of the drop and a temperature of the vapor but scaled the velocity of each particle with the same factor to keep the kinetic energy of the entire system fixed. The equilibration takes approximately 60,000 timesteps (for the system with $N=5165$) to 120,000 timesteps ($N=2299$) for systems prepared this way but may become 260,000 ($N=12,138$) or even 500,000 ($N=9295$) timesteps in case of a less careful preparation. The equilibration is monitored most sensitively by the potential energy of the system and the density profile and we took care that they had stabilized before the measurements started. The number of configurations sampled in the equilibrated systems is also listed in table 1.

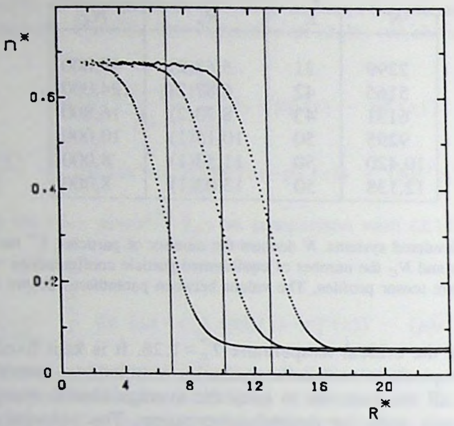

Fig. 2. Density profiles for three different system sizes: $N = 5165$, $N = 9295$ and $N = 12,138$. The reduced density n^* is defined as $n\sigma^3$. Vertical lines denote the equimolar radii of the droplets. The number of configurations included in the averages are listed in table 1.

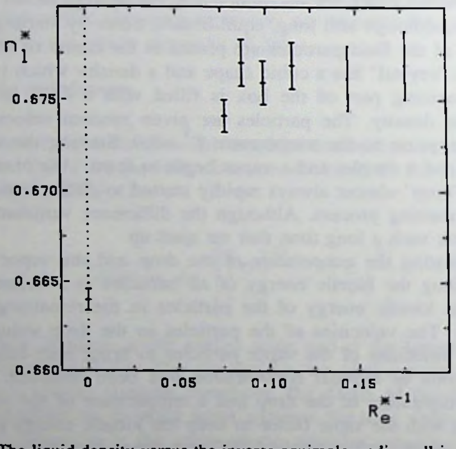

Fig. 3. The liquid density versus the inverse equimolar radius, all in reduced units.

The configurations are sampled each 15th timestep. Error bars in the data denote the standard deviation as calculated from subaverages over 200 particle configurations each.

The droplet is kept in the middle of the box by keeping the centre of mass of the drop in the middle. The centre of mass of the drop is determined as the centre of mass of the fluid in a cubic volume which just encloses the droplet. This centre of mass is evaluated regularly and, since it is never precisely at the origin of the computational box, the entire system is translated after each evaluation such that the centre of mass is placed back at the origin. The frequency with which the centre of mass is shifted back ranges from each 500^{th} timestep for the large drops to each 75^{th} timestep for the smallest. For large drops, it would suffice to take as the centre of mass of the droplet the centre of mass of the entire fluid since nearly all the mass is concentrated in the drop. Moreover, since the centre of mass of the entire system is a conserved quantity of the equations of motion and all centre of mass motion thus results from rounding off errors in the molecular-dynamics scheme, large droplets remain almost in place by themselves. However, this does not hold for the smallest drops we encounter: the restriction on the centre of mass of the entire fluid is not sufficient to keep the droplet in place if there is not enough mass concentrated in it. As a result, the position of the small drops fluctuates strongly and we have to calculate the centre of mass from the drop and its immediate surrounding itself to fix the drop in the middle of the box.

4. Results

From the sampled particle configurations, we calculate the local density $n(r)$ and the pressure tensor components $p_N(r)$ and $p_T(r)$ as a function of the distance r from the centre of the box. The density at a distance r from the centre is measured as the average number of particles in a spherical shell with a small width w around the radius r (the width w equals $\sqrt{3}\,L/1024$ in our simulations) divided by the volume of the shell. Figs. 2 shows some typical density profiles for droplets of different sizes. In general, the noise on these profiles increases near the origin since the volumes of the shells become smaller and therefore, the fluctuations in the average number of particles in the shell grow. These increasing fluctuations are suppressed in fig. 2 by averaging over a varying number of shells near the origin which explains why the resolution in the figure is less near $r=0$. From these profiles, we obtain the liquid and vapor bulk densities n_l and n_v as the average number of particles per volume within respectively outside a sensibly chosen radius R. The equimolar dividing radius is calculated from (2.5) with the condition $\Gamma=0$ which leads to the following equation for R_e:

$$N = n_l \, \frac{4\pi}{3} \, R_e^3 + n_v \, (L^3 - \frac{4\pi}{3} R_e^3) \tag{4.1}$$

The reduced droplet radii $R_e^* = R_e/\sigma$ are listed in table 1. They range from $R_e^* = 13.03 \pm 0.01$ for the largest system we could study to $R_e^* = 6.87 \pm 0.02$ below which the drops became unstable. We tried to form a droplet in a system with 1977 fluid particles and a boxlength $L^* = 30$ but the droplet evaporated and the box became filled with a homogeneous vapor phase.

The reduced bulk densities n_l^* and n_v^* are shown in fig. 3 and 4 as a function of $1/R_e^*$. The density of the bulk vapor can be determined very accurately since the vapor phase is always large but to calculate the density of the liquid, we have to choose R, the radius within which the average density is determined, rather small when the droplet becomes small. For example, the radius R is chosen at $R^* = 2$ for the droplet with $R_e^* = 5.63$ so the region in which bulk liquid conditions are assumed becomes very small (see fig. 5). It is clearly seen that the bulk phases are off their planar coexistence states: both the liquid and

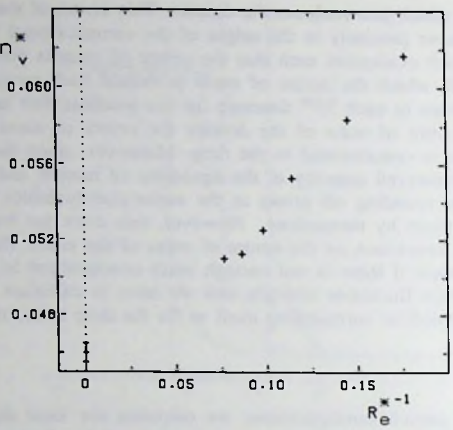

Fig. 4. The vapor density versus the inverse equimolar radius, all in reduced units. Error bars are smaller than the symbol sizes.

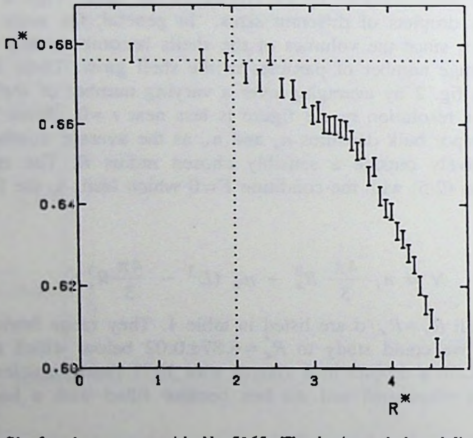

Fig. 5. Density profile for the system with $N=5165$. The horizontal dotted line denotes the liquid density, determined as the average density in a sphere with radius $R^*=2$ (vertical dotted line). The number of configurations included in the average is listed in table 1.

the vapor phase are compressed. The vapor density strongly increases with decreasing droplet size, showing that small drops are only stable in a surroundings of a high pressure vapor phase. The liquid density appears to be constant in the range of droplet radii we can access, although it is well above its planar value and should decrease for larger drops. Note that

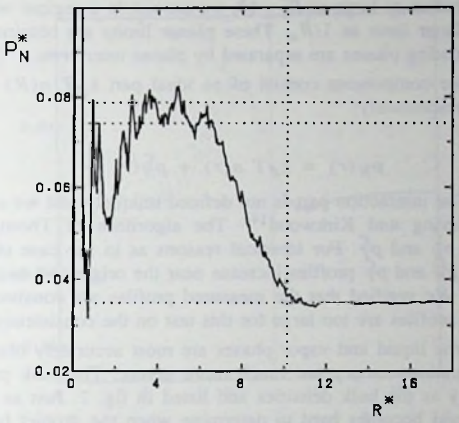

Fig. 6. Normal component of the pressure tensor in reduced units $p_N^* = p_N \sigma^3 / \varepsilon$ for the system with $N = 9295$. Upper two horizontal dotted lines show the estimated bounds on the pressure of the liquid, lower horizontal dotted line shows the pressure of the vapor. The vertical dotted line denotes the position of the equimolar radius. The number of configurations included in the average is listed in table 1.

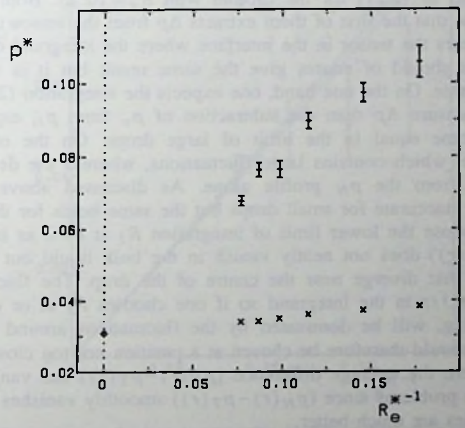

Fig. 7. Pressure in the liquid (+) and vapor phase (×) versus the inverse equimolar radius, all in reduced units. The planar limit is the same for both phases.

even for drops with a radius as large as $R_e^* = 13$, we are not in a regime where the bulk densities approach their planar limit as $1/R_e$. These planar limits are obtained[13)] from simulations in which the coexisting phases are separated by planar interfaces.

The pressure tensor components consist of an ideal part $k_B T\ n(R)$ and an interaction part $p_N^C(r)$ and $p_T^C(r)$ respectively:

$$p_N(r) \ = \ k_B T\ n(r) \ + \ p_N^C(r) \tag{4.2}$$

and similarly for p_T. The interaction part is not defined uniquely and we chose to measure it as it is defined by Irving and Kirkwood[14)]. The algorithm of Thompson *et al*[10)] was employed to calculate p_N^C and p_T^C. For identical reasons as in the case of the density $n(r)$, the fluctuations in the p_N^C and p_T^C profiles increase near the origin. An example of a p_N profile is given in fig. 6. We verified that the measured profiles are consistent with (2.20) but the fluctuations on the profiles are too large for this test on the consistency to be very strict.

The pressures in the liquid and vapor phases are most accurately obtained from the p_N profile since the fluctuations on p_T are much more severe. The bulk pressures are determined in the same way as the bulk densities and listed in fig. 7. Just as the liquid density, the pressure in the liquid becomes hard to determine when the droplet becomes small. The planar limit is obtained from previous measurements in a planar system[13)].

The pressure difference Δp can be obtained in two ways: by subtracting the pressures p_l and p_v from each other as they are determined from the plateaux in the p_N profile or from (2.21) with $d=3$. As an example, fig. 8 shows the difference $(p_N(r) - p_T(r))$ that appears in the integrand of (2.21) for the droplet with $R_e = 10.15$. Both ways to Δp are independent in the sense that the first of them extracts Δp from the tensor in the bulk phases while the second monitors the tensor in the interface where the integrand of (2.21) does not vanish. The two routes should of coures give the same result but it is not clear a priori which is the most accurate. On the one hand, one expects the integration (2.21) to be a more sensitive method to measure Δp than the subtraction of p_v from p_l, especially since the latter two should become equal in the limit of large drops. On the other hand, (2.21) involves the p_T profile, which contains large fluctuations, whereas the determination of p_l and p_v can be done from the p_N profile alone. As discussed above, the first route, $\Delta p = p_l - p_v$ becomes inaccurate for small drops but the same holds for the second. This is because we can not choose the lower limit of integration R_l at $r=0$ as in (2.21) since the difference $(p_N(r) - p_T(r))$ does not neatly vanish in the bulk liquid but fluctuates around zero with fluctuations that diverge near the centre of the drop. The fluctuations are even amplified by the factor $1/r$ in the integrand so if one chooses R_l at or close to $r=0$, the integral, if not diverging, will be dominated by the fluctuations around the centre of the drop. The lower limit should therefore be chosen at a position not too close to $r=0$ but still in the bulk liquid where the average difference $(p_N(r) - p_T(r))$ has vanished. The upper limit R_v gives no such problems since $(p_N(r) - p_T(r))$ smoothly vanishes in the bulk vapor phase where the statistics are much better.

The results for both routes are shown in fig. 9 which demonstrates that the two routes give, within the error bars, the same result. The increasing difficulties in the determination of Δp when the drop becomes small are reflected in the increasing error bars at small R_e. The pressure difference is well described by the asymptotic result $\Delta p = 2\gamma_\infty / R_e$ for the largest drops but deviations seem to occur when the drops become smaller. Unfortunately, these

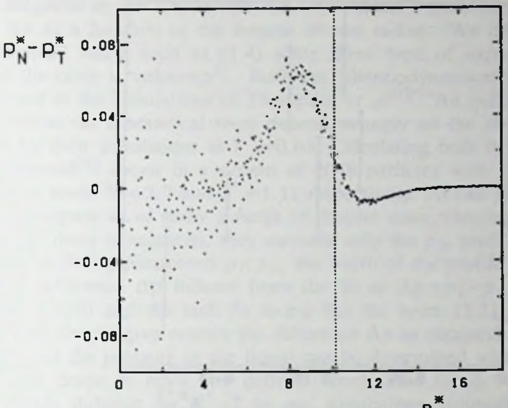

Fig. 8. Difference between the normal and tangential component of the pressure tensor for the system with $N = 9295$. The vertical dotted line denotes the position of the equimolar radius. The number of configurations included in the average is listed in table 1.

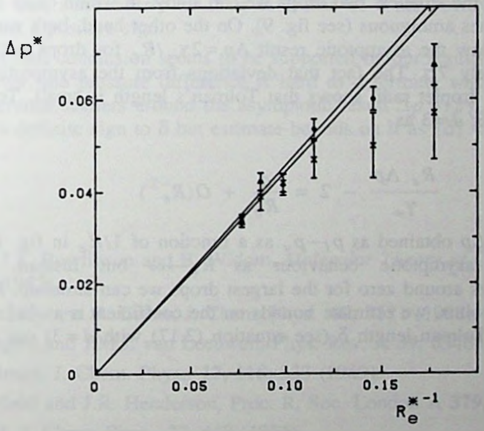

Fig. 9. Pressure difference versus the inverse equimolar dividing radius, all in reduced units. Crosses are obtained from the integral (2.21), circles are obtained by the subtraction of p_v from p_l as given in fig. 7. The lines denote the asymptotic result $\Delta p = 2\gamma_\infty / R_e$ with $\gamma_\infty = 0.223$ and $\gamma_\infty = 0.229$ which are the estimated[16)] bounds on γ_∞ according to one standard deviation.

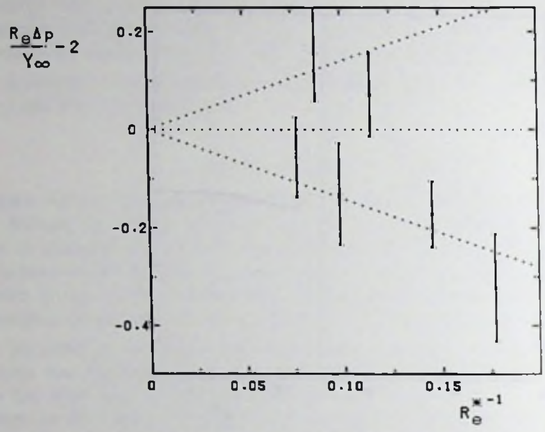

Fig. 10. The l.h.s. of equation (4.3) versus the inverse equimolar radius. The outer dotted lines give the estimated bounds on the coefficient *a*.

deviations occur only for the smallest two drops we can study, in which cases the determination of Δp already becomes ambiguous (see fig. 9). On the other hand, both ways to measure Δp indicate that it is below the asymptotic result $\Delta p = 2\gamma_\infty / R_e$ for drops with a radius R_e smaller than approximately 7σ. The fact that deviations from the asymptotic result occur only for relatively small droplet radii shows that Tolman's length is small. To estimate this length, we write (2.14) for $d=3$ as

$$\frac{R_e \, \Delta p}{\gamma_\infty} - 2 = \frac{a}{R_e} + O(R_e^{-2}) \tag{4.3}$$

and plot the l.h.s., with Δp obtained as $p_l - p_v$ as a function of $1/R_e$ in fig. 10. We do not find a well defined asymptotic behaviour as $R_e \to \infty$ but instead, the quantity $((R_e \Delta p / \gamma_\infty) - 2)$ scatters around zero for the largest drops we can simulate. From the location of these scattering points, we estimate bounds on the coefficient a as $|a| < 1.4\sigma$. Since a equals two times the Tolman length δ (see equation (2.17) with $d=3$) our estimate for δ reads $|\delta| < 0.7\sigma$.

5. Conclusions.

By a thermodynamic analysis of the pressure difference over the interface of the drop, one obtains an expression for the Tolman[4)] length δ in terms of a pressure tensor which differs from the classical result (1.4). The expression we propose is independent of the choice of the tensor but, unfortunately, it does not express δ in the tensor of a planar interface alone but one also needs to know how the tensor approaches its planar limit.

The same procedure we followed to obtain the statistical mechanical expression (2.24) for δ was followed in the simulations, i.e. we extract δ from measurements of the pressure difference Δp as a function of the inverse droplet radius. We did not try to obtain δ from any "mechanical" route such as (1.4) since these type of expressions are not rigorously correct and the error is unknown$^{5)}$. Both the "thermodynamical" and the mechanical route were employed in the simulations of Thompson *et al*$^{10)}$. An indication that the results for δ as obtained from the mechanical route depend strongly on the choice of the pressure tensor is provided by their simulations at $T^* = 0.63$. Calculating both the Harasima$^{15)}$ and the Irving and Kirkwood$^{14)}$ tensor in a system of 2048 particles with $R_e^* = 8.38$ they obtain from the mechanical route $\delta^* = 2.7$ and $\delta^* = 1.11$ respectively. At two temperatures, $T^* = 0.71$ and $T^* = 0.80$, Thompson *et al* study a range of droplet sizes, varying from $R_e^* \approx 2$ to $R_e^* \approx 6$. In the majority of these simulations, they measure only the p_N profile which is fitted to a tanh function with as fitting parameters p_l, p_v, the width of the profile and the profile's location. The pressure difference Δp follows from the fit as $\Delta p = p_l - p_v$. The p_T profile is constructed from (2.20) and the tanh fit to p_N but the route (2.21) to Δp is then no longer independent but should give exactly the difference Δp as obtained from the fit. However, we do not think that the pressure in the liquid can be determined with a large enough accuracy for such small drops to draw any definite conclusions for δ. The determination of Δp becomes already dubious for $R_e^* \leq 7$ in our simulations although for temperatures below $T^* = 0.9$, this limit could be somewhat lower because the interfaces are sharper. It should e.g. be noted that their estimates of δ at the temperatures $T^* = 0.71$ and $T^* = 0.80$ as obtained from their "thermodynamic route" become smaller with increasing droplet size. These objections were also recognized by the authors themselves and they give no precise estimate of δ but, since nearly all their estimates of δ are positive, conclude that it seems clear that δ has a positive sign.

This cautious conclusion seems to be supported by our results for the smallest drops for which, however, the pressure difference is hard to determine while for the large drops, the pressure difference scatters around the asymptotic result $\Delta p = (2\gamma_\infty)/R_e$. Therefore, we can not attribute a definite sign to δ but estimate bounds on it as $|\delta| < 0.7\sigma$ at $T^* = 0.9$.

References

1) see e.g. J.S. Rowlinson and B. Widom, *Molecular Theory of Capillarity* (Clarendon, Oxford, 1982).

2) D.W. Oxtoby and R. Evans, J. Chem. Phys. **89,** 7521 (1988).

3) J.V. Sengers and J.M.J. van Leeuwen, Phys. Rev. A **39,** 6346 (1989).

4) R.C. Tolman, J. Chem. Phys. **17,** 118, 333 (1949).

5) D. Schofield and J.R. Henderson, Proc. R. Soc. London A **379,** 231 (1982).

6) F.P. Buff, J. Chem. Phys. **23,** 419 (1955).

7) S.J. Hemingway, J.R. Henderson and J.S. Rowlinson, Proc. R. Soc. London A **379,** 231 (1982).

8) M.P.A. Fisher and M. Wortis, Phys. Rev. B **29** 6252 (1984).

9) S.J. Hemingway, J.R. Henderson and J.S. Rowlinson, Faraday Sympos. Chem. Soc. **16,** (1981)

10) S.M. Thompson, K.E. Gubbins, J.P.R.B. Walton, R.A.R. Chantry and J.S. Rowlinson, J. Chem. Phys. **81**, 530 (1984).
11) J.R. Henderson and J.S. Rowlinson, J. Phys. Chem. **88**, 6484 (1984).
12) A.F. Bakker and C. Bruin, in *Special Purpose Computers*, edited by B.J. Alder (Academic, London, 1988).
13) M.J.P. Nijmeijer, C. Bruin, A.F. Bakker and J.M.J. van Leeuwen, chapter IV of this thesis.
14) J.H. Irving and J.G. Kirkwood, J. Chem. Phys. **18**, 817 (1950).
15) A. Harasima, Adv. Chem. Phys. **1**, 203 (1958).
16) M.J.P. Nijmeijer, C. Bruin, A.F. Bakker and J.M.J. van Leeuwen, chapter VIII of this thesis and
M.J.P. Nijmeijer, C. Bruin, A.F. Bakker and J.M.J. van Leeuwen, to be published.

SAMENVATTING

SIMULATIES VAN VLOEISTOF OPPERVLAKKEN

In dit proefschrift worden grootschalige computersimulaties besproken van systemen waarin een vloeistoffase, een gasfase en eventueel een substraat aanwezig zijn. De oppervlakken tussen deze fasen zijn het onderwerp van studie. Deze systemen vereisen een groot aantal deeltjes en dientengevolge een grote rekencapaciteit. Het gebruik van een "special purpose" computer, de Delft Molecular-Dynamics Processor (DMDP), die een systeemgrootte tot en met 16.000 deeltjes toelaat en daarbij de rekentijden binnen acceptabele grenzen houdt, maakt deze simulaties mogelijk.

Simulaties geven een gedetailleerd inzicht in de microscopische structuur van een oppervlak. Hierdoor kunnen exacte, statistisch-mechanische uitdrukkingen die een verband leggen tussen macroscopische en microscopische grootheden, geëvalueerd worden. Een voorbeeld is de uitdrukking voor de oppervlaktespanning als een integraal over de paarkorrelatiefunctie, een uitdrukking die in de simulaties veelvuldig gebruikt wordt om de oppervlaktespanning te meten. Deze grootheid bepaald namelijk de thermodynamische toestand van het oppervlak en speelt daarom dezelfde centrale rol voor een oppervlak als de druk voor een bulkfase.

De verschillende fasen worden in de DMDP gerepresenteerd door Lennard-Jones deeltjes met een afgekapte wisselwerking. De simulaties zijn van het moleculaire-dynamica type zoals de afkorting DMDP al aangeeft. Belangrijke beperkingen aan de simulaties zijn de beperking aan systeemgrootte en de beperking aan de dracht van de interakties tussen de deeltjes. Beide beperkingen hebben in het algemeen een aanzienlijke invloed op de gesimuleerde oppervlakken maar desalniettemin vormen deze een niet onredelijke beschrijving van een oppervlak zoals dat bijvoorbeeld door een edelgas gevormd wordt. De simulaties vallen uiteen in twee klassen. De meerderheid, beschreven in de hoofdstukken III-VII, is gerelateerd aan de zogenaamde "wetting" en "drying" overgang, de laatste twee hoofdstukken zijn gewijd aan het vloeistof-gas oppervlak. Deze twee klassen zijn niet onafhankelijk daar vrije vloeistof-gas oppervlakken ook een rol spelen in wetting en drying verschijnselen maar ze zijn beide interessant genoeg om een aparte studie te rechtvaardigen.

In het geval van de hier beschreven simulaties refereren de termen "wetting" en "drying" aan de adsorptie van een systeem bestaande uit een coëxisterende vloeistof- en gasfase aan een substraat. De wetting overgang is gedefinieerd als de overgang waarbij een substraat-gas oppervlak spontaan vervangen wordt door een substraat-vloeistof en een vloeistof-gas oppervlak. De overgang vindt plaats op het moment dat de substraat-vloeistof plus de vloeistof-gas oppervlaktespanning lager wordt dan de substraat-gas oppervlaktespanning. De drying overgang is de complementaire overgang, waarbij een substraat-vloeistof oppervlak vervangen wordt een substraat-gas en een vloeistof-gas oppervlak. In een experiment wordt de wetting overgang vaak bestudeerd aan de hand van een druppel die op het substraat rust en omgeven is door een verzadigde damp. De wetting overgang vindt plaats op het moment dat de druppel over het substraat uitspreidt en deze geheel met een macroscopisch vloeistoflaagje bedekt. Ze wordt dus gekarakteriseerd door het nul worden van de kontakthoek tussen de meniscus van de drupppel en het substraat-vloeistof oppervlak.

Analoog hieraan vindt de drying overgang plaats op het moment dat de kontakthoek gelijk wordt aan π maar deze overgang is nog niet experimenteel waargenomen. De kontakthoek is op een eenvoudige wijze gerelateerd aan de substraat-vloeistof, substraat-gas en de vloeistof-gas oppervlaktespanning via de wet van Young. De manier waarop de kontakthoek zijn extreme waarden 0 en π bereikt geeft de orde van de wetting c.q. drying overgang aan.

De eerste simulaties van de wetting en drying overgang op de DMDP werden uitgevoerd door Sikkenk *et al.* De overgangen werden bewerkstelligd door de interaktiesterkte ε tussen de substraatdeeltjes en de deeltjes die de vloeistof- en gasfase vormen, te variëren. Bij toenemende ε vindt een drying overgang plaats, gevolgd door een wetting overgang. Uit metingen van de oppervlaktespanningen en de daaruitvolgende kontakthoek werd het optreden van deze overgangen aangetoond en gekonkludeerd dat beide van een eerste orde karakter zijn. De metingen van de substraat-gas en substraat-vloeistof oppervlaktespanning bleken echter controversieel te zijn ten gevolge van het optreden van spanningen in de wand. Daarmee werden in het bijzonder de konklusies aangaande de lokatie en orde van de drying overgang op losse schroeven gezet.

Alvorens de simulaties beschreven worden, wordt in hoofdstuk I een algemene inleiding gegeven en worden in hoofdstuk II relaties tussen grootheden zoals de oppervlaktespanning en de microscopische eigenschappen van het systeem afgeleid. Deze relaties worden in de simulaties veelvuldig gebruikt en hoofdstuk II legt daarmee de basis voor de metingen in de volgende hoofdstukken.

Hoofdstuk III beschrijft een aantal simulaties waarin de kontakthoek visueel gemeten wordt, daarmee een meting van de oppervlaktespanningen omzeilende. Wederom wordt, als in de simulatie van Sikkenk *et al*, de kontakthoek als funktie van ε gemeten en deze hoeken vertonen een grote verschuiving van de positie van de drying overgang vergeleken met Sikkenks simulatie. Bovendien zijn de nieuwe data consistent met zowel een eerste-orde als een continue drying overgang. De wetting overgang daarentegen blijft sterk eerste orde.

Dit gewijzigde beeld wordt bevestigd in de simulaties van hoofdstuk IV. De opzet van deze simulaties is gelijk aan die van Sikkenk *et al* uitgezonderd de representatie van het substraat. Terwijl in Sikkenk's simulatie de wanddeeltjes vrij waren te bewegen en het substraat daarom leek op een thermodynamische fase, worden in deze simulaties de wanddeeltjes ingevroren op hun roosterposities. Hiermee wordt het effekt van spanningen in de wand geëlimineerd en is een veel nauwkeuriger bepaling van de substraat-vloeistof en substraat-gas oppervlaktespanningen mogelijk. De kontakthoeken die hieruit worden berekend stemmen goed overeen met de visuele metingen uit het vorige hoofdstuk.

Een veel scherpere bepaling van de orde en de lokatie van de drying overgang wordt gegeven in hoofdstuk V. In plaats van de kontakthoek, wordt hierin de variatie van de kontakthoek met ε gemeten. De metingen duiden er sterk op dat de drying overgang een continu karakter heeft en de onzekerheid in de lokatie van de overgang wordt er een orde van grootte door verkleind.

In hoofdstuk VI wordt de invloed van een lange-drachtskracht op de wetting en drying overgang bestudeerd. De lange-drachtskracht die aan de simulaties wordt toegevoegd, is die tussen de deeltjes die de wand vormen en de deeltjes die het gas en de vloeistof vormen. De lange-drachtskrachten tussen de wanddeeltjes onderling en tussen de vloeistof- en gasdeeltjes onderling kunnen niet in de simulaties meegenomen worden omdat de rekentijd hierdoor dramatisch zou toenemen. Naar verwachting wordt de drying overgang onderdrukt door de toegevoegde lange-drachtskracht en de simulaties bevestigen dit.

Een eerste orde wetting overgang dient vergezeld te gaan van een zogenaamde prewetting overgang. Deze behelst een overgang tussen een dunne geadsorbeerde film en een dikkere geadsorbeerde film die plaatsvindt in het regime van de onderverzadigde damp. Deze overgang is nog niet experimenteel waargenomen maar alleen in simulaties van rooster gassen en in één simulatie van een Lennard-Jones systeem. In onze simulaties wordt de adsorptie aan het substraat gemeten als funktie van de gasdichtheid en de waarde van ε maar we kunnen de prewetting overgang niet overtuigend waarnemen, wel vinden we tekenen die op de overgang wijzen.

De hoofdstukken VIII en IX zijn niet gewijd aan wetting-achtige verschijnselen maar aan het vloeistof-gas oppervlak. In hoofdstuk VIII worden simulaties van planaire vloeistof-gas oppervlakken besproken. In de literatuur worden verschillende, vaak uiteenlopende waarden voor de oppervlaktespanning van dit oppervlak (voor een systeem met afgekapte Lennard-Jones wisselwerkingen) genoemd. We hebben de oppervlaktespanning alsmede de eigenschappen van de coëxisterende fasen nauwkeurig gemeten bij verschillende temperaturen. Daarnaast hebben we het effekt van de afkapstraal bestudeerd door deze drie maal te vergroten. De toename in het bereik van de wisselwerking blijkt grote gevolgen te hebben.

In het laatste hoofdstuk wordt de invloed van een kromming van het oppervlak besproken aan de hand van simulaties van druppeltjes. Aangenomen wordt dat de oppervlaktespanning van een gekromd oppervlak afwijkt van die van een vlak oppervlak met een bedrag van de orde van de inverse kromtestraal. De afwijking kan bepaald worden uit een meting van het drukverschil over het oppervlak maar blijkt uit de simulaties klein te zijn.

CURRICULUM VITAE

van

Marco Jan Pieter Nijmeijer

Geboren op 25 juni 1964 te Beverwijk

In juni 1982 behaalde ik het VWO diploma aan het Thomas More College te Oudenbosch. Aansluitend begon ik in september de studie natuurkunde aan de Rijksuniversiteit Leiden waar ik in september 1983 het propadeutisch examen verkreeg. De experimentele stage heb ik verricht in de groep Quantumvloeistoffen o.l.v. prof. dr. G. Frossati. Gedurende de studie ben ik lid geweest van de Onderwijscommissie. Naast de studie natuurkunde heb ik in februari 1986 een propadeutisch examen in de wiskunde afgelegd. Mijn doctoraal scriptie getiteld "Time dependence of the overlap in two random spin systems" lag op het gebied van de theoretische natuurkunde en is geschreven o.l.v. prof. dr. H.J. Hilhorst. Het doctoraal examen werd mij in september 1986 uitgereikt. Direkt hierna begon in oktober mijn promotiewerk als Assistent In Opleiding in dienst van de "Stichting voor Fundamenteel Onderzoek der Materie" (F.O.M.). Dit werk is grotendeels verricht aan de Technische Universiteit Delft hoewel ik ook mijn promotor in het Instituut Lorentz van de Rijksuniversiteit Leiden regelmatig heb bezocht.

LIST OF PUBLICATIONS

1) M.J.P. Nijmeijer, A.F. Bakker, C. Bruin and J.H. Sikkenk, *A molecular dynamics simulation of the Lennard-Jones liquid-vapor interface*, J. Chem. Phys. **89**, 3789 (1988).

2) M.J.P. Nijmeijer, C. Bruin, A.F. Bakker and J.M.J. van Leeuwen, *A visual measurement of contact angles in a molecular-dynamics simulation*, Physica A **160**, 166 (1989).

3) J.M.J. van Leeuwen, M.J.P. Nijmeijer and C. Bruin, *Molecular Dynamics of Wetting and Drying at Solid-Fluid Interfaces*, Physica Scripta **T25**, 256 (1989).

4) M.J.P. Nijmeijer, C. Bruin, A.F. Bakker and J.M.J. van Leeuwen, *Molecular Dynamics of Wetting and Drying at Solid-Fluid Interfaces*, in *Static and Dynamic Properties of Liquids*, edited by M. Davidović and A.K. Soper (Springer-Verlag, 1989).

5) M.J.P. Nijmeijer and J.M.J. van Leeuwen, *Microscopic expressions for the surface and line tension*, accepted for publication in J. Phys. A.

6) M.J.P. Nijmeijer, C. Bruin, A.F. Bakker and J.M.J. van Leeuwen, *Wetting and drying of an inert wall by a fluid in a molecular-dynamics simulation*, submitted.

7) M.J.P. Nijmeijer, C. Bruin, A.F. Bakker and J.M.J. van Leeuwen, *A search for prewetting in a molecular-dynamics simulation*, submitted.

8) M.J.P. Nijmeijer, C. Bruin, A.F. Bakker and J.M.J. van Leeuwen, *Accurate determination of the location and order of the drying transition in a molecular-dynamics simulation*, submitted.

A reduced version of chapter II is contained in publication 5. The chapters III, IV, V, VII and VIII are, apart from minor modifications, contained in the publications 2, 6, 8, 7 and 1 respectively. The chapters VI and IX are being prepared for publication.

Nawoord

Tenslotte rest mij de plezierige taak enkele mensen te bedanken die een bijdrage hebben geleverd aan de totstandkoming van dit proefschrift. Allereerst zijn dit mijn ouders. Ze hebben er nooit op aangedrongen om toch timmerman te worden maar, integendeel, mijn verwoede pogingen om iets te begrijpen van een zo'n moeilijk vak als natuurkunde, van harte ondersteund. Bijzondere dank ben ik ook verschuldigd aan sgt. J. Lamers voor zijn suggestie om iedere morgen met een natte vinger over de *s* van het woordje *drs* op mijn naamplaatje te wrijven, in de verwachting dat deze letter na vier jaar wel weggepoetst zal zijn. Een serieuzere bijdrage aan de verwijdering van deze letter was de voortdurende aandacht van mijn promotor voor de Delftse simulaties. Ook zijn vermogen om hele korte metten te maken van alle door mij aangedragen onzin, heeft het gehalte van dit proefschrift aanzienlijk verhoogd. Daarnaast heb ik met plezier zijn "skating academy" gevolgd waar ik echter al spoedig ontdekte dat het behalen van een titel in deze branche voor mij niet is weggelegd. Niet minder was de betrokkenheid van mijn co-promotor die ik heb leren kennen als iemand die een grote zorgvuldigheid aan de dag legt bij het uitvoeren van de simulaties. Ik hoop dat hij zijn grijze haren niet te danken heeft aan de begeleiding van aanstormende, immer eigenwijze promovendi.

De bijdrage van A. van Woerkom (each day is a PFILE day) verdient een eervolle vermelding. Zuchtend liet hij zich overhalen om de assembler programma's voor de meting van de druktensor te schrijven. De aldus gekweekte familie DTSOR programma's heeft niettemin in hem een goede vader; ze vormt een betrouwbare hoeksteen onder deze simulaties. Ook F. Lange kampte met een enigszins haperend startmechanisme. Eenmaal aangeduwd heeft hij me echter veel werk uit handen genomen door een deel van de dagelijkse routine van de simulaties op zich te nemen. Een bijzonder genoegen heb ik beleefd aan de inspanningen van E. Hirshowitz op wiens conto de numerieke aanpassingen aan de menisci van hoofdstuk III staan. De overeenkomst tussen zijn resultaten en het handwerk dat ik enkele maanden daarvoor m.b.v een passer en een bloedige ijver volbracht had, vervulde mij van een diepe tevredenheid. Dat de apparatuur gedurende de afgelopen vier jaar niet is ingestort is vnl. te danken aan D. van Delft en F. Berwald. Gewapend met föhn, spuitbus en het wonder van de magische handoplegging, hebben zij de onwillige hardware op enkele kritieke momenten tot de orde geroepen. De kennis van Y. Fonk omtrent de tekstverwerker vindt u terug in de lay-out van dit boekje. Iedereen die me tot steun is geweest ben ik erkentelijk voor zijn of haar vaak onzichtbare bijdragen aan het welslagen van deze promotie.

Stellingen behorend bij het proefschrift:

SIMULATION OF FLUID INTERFACES

1) Hoewel het opleggen van "Saint-Venant's strain compatibility conditions" aan de druktensor de ambiguiteit in de mechanische definitie van het "surface of tension" verwijdert, betekent dit niet dat het aldus gedefinieerde "surface of tension" Tolmans lengte bepaald.

M. Baus en R. Lovett, preprint.
Hoofdstuk IX van dit proefschrift.

2) De door J.R. Henderson en F. van Swol waargenomen fluctuaties in de bedekking bij de drying overgang duiden eerder op een continu dan op een eerste-orde karakter van deze overgang.

J.R. Henderson en F. van Swol, J. Phys. Cond. Matt. **2**, *4537 (1990).*

3) De enorme verscheidenheid aan wetting en drying verschijnselen en de gevoeligheid ervan voor de keuze van het oppervlakteveld zoals volgt uit mean-field berekeningen, stemt niet overeen met het veel uniformere beeld dat door experimentele waarnemingen vertoond wordt.

G. Langie en J.O. Indekeu, Phys. Rev. B **40**, *417 (1989).*
S. Dietrich, in Phase Transitions and Critical Phenomena, edited by C. Domb and J.L. Lebowitz (Academic, London, 1988), Vol. 12.

4) De vorm van een Ising druppel geadsorbeerd aan een substraat zoals berekend door L.-F. Ko en M.E. Fisher dient ook te volgen uit een berekening die gestoeld is op de minimalisatie van de oppervlakte-vrije-energie.

L.-F. Ko en M.E. Fisher, J. Stat. Phys. **58**, *249 (1990).*

5) De Van der Waals theorie geeft voor de in dit proefschrift beschreven simulaties een zeer onrealistisch beeld van de prewetting overgang.

6) Voor het quantumroostergas met uitsluiting van 3 buren concludeert F. Mallezie ten onrechte tot een eerste orde faseovergang.

F. Mallezie, Phys. Rev. B **41**, *4475 (1990).*

7) De aanwezigheid van een groot aantal schaalfactoren in de programmatuur voor de DMDP is een niet te onderschatten nadeel van de "fixed point" rekenwijze van deze machine.

8) In de figuur van de pleegmoeder van Tomek laat Kieslowski zien dat de verschillen tussen de gevestigde normen en waarden en het onaangepaste gedrag van haar pleegzoon, kleiner zijn dan op het eerste gezicht lijkt.

A short film about love, de speelfilmversie van het zesde deel van de Dekalog, geregisseerd door K. Kieslowski (1988).

9) De commotie rond het onderzoek van Swaab aan de hersenen van homosexuele mannen toont aan hoezeer men zich verzet tegen een mechanisch beeld van de menselijke aard, daar waar we aan het beeld van het lichaam als een geavanceerd bouwpakket al lang gewend zijn.

10) Het is onwaarschijnlijk dat de behandeling van de partitiefunktie in termen van clusters omgeven door een ideaal gas, een adequate beschrijving geeft van de nucleatie in een oververzadigde damp.

H. Reiss, A. Tabazadeh en J. Talbot, J. Chem. Phys. **92**, *1266 (1990).*

M.J.P. Nijmeijer, juli 1990

BIBLIOTHEEK
INSTITUUT-LORENTZ
voor theoretische natuurkunde
Postbus 9506 - 2300 RA Leiden
Nederland